Composites Science and Technology

It Meng Low
Nurul Zahirah Noor Azman

Polymer Composites and Nanocomposites for X-Rays Shielding

Springer

Composites Science and Technology

Series Editor

Mohammad Jawaid, Lab of Biocomposite Technology, Universiti Putra Malaysia, INTROP, Serdang, Malaysia

Composites Science and Technology (CST) book series publishes the latest developments in the field of composite science and technology. It aims to publish cutting edge research monographs (both edited and authored volumes) comprehensively covering topics shown below:

- Composites from agricultural biomass/natural fibres include conventional composites-Plywood/MDF/Fiberboard
- Fabrication of Composites/conventional composites from biomass and natural fibers
- Utilization of biomass in polymer composites
- Wood, and Wood based materials
- Chemistry and biology of Composites and Biocomposites
- Modelling of damage of Composites and Biocomposites
- Failure Analysis of Composites and Biocomposites
- Structural Health Monitoring of Composites and Biocomposites
- Durability of Composites and Biocomposites
- Biodegradability of Composites and Biocomposites
- Thermal properties of Composites and Biocomposites
- Flammability of Composites and Biocomposites
- Tribology of Composites and Biocomposites
- Bionanocomposites and Nanocomposites
- Applications of Composites, and Biocomposites

To submit a proposal for a research monograph or have further inquries, please contact springer editor, Ramesh Premnath (ramesh.premnath@springer.com).

More information about this series at http://www.springer.com/series/16333

It Meng Low · Nurul Zahirah Noor Azman

Polymer Composites and Nanocomposites for X-Rays Shielding

Springer

It Meng Low
Department of Applied Physics
Curtin University
Perth, WA, Australia

Nurul Zahirah Noor Azman
School of Physics
Universiti Sains Malaysia
Gelugor, Pulau Pinang, Malaysia

Composites Science and Technology
ISBN 978-981-13-9809-4 ISBN 978-981-13-9810-0 (eBook)
https://doi.org/10.1007/978-981-13-9810-0

© Springer Nature Singapore Pte Ltd. 2020
This work is subject to copyright. All rights are reserved by the Publisher, whether the whole or part of the material is concerned, specifically the rights of translation, reprinting, reuse of illustrations, recitation, broadcasting, reproduction on microfilms or in any other physical way, and transmission or information storage and retrieval, electronic adaptation, computer software, or by similar or dissimilar methodology now known or hereafter developed.
The use of general descriptive names, registered names, trademarks, service marks, etc. in this publication does not imply, even in the absence of a specific statement, that such names are exempt from the relevant protective laws and regulations and therefore free for general use.
The publisher, the authors and the editors are safe to assume that the advice and information in this book are believed to be true and accurate at the date of publication. Neither the publisher nor the authors or the editors give a warranty, expressed or implied, with respect to the material contained herein or for any errors or omissions that may have been made. The publisher remains neutral with regard to jurisdictional claims in published maps and institutional affiliations.

This Springer imprint is published by the registered company Springer Nature Singapore Pte Ltd.
The registered company address is: 152 Beach Road, #21-01/04 Gateway East, Singapore 189721, Singapore

Contents

Chapter 1
Introduction and Background

Abstract Radiation (X-ray/gamma-ray) shielding is an age-old problem and has been studied in greater details up till now, due to their interactions being most prominent in many applications such as in medical fields (i.e. diagnostic imaging and therapy). X-rays/gamma-rays are the most penetrating of ionizing radiation that is known to be harmful to human health and heredity. X-ray photons are produced by the interaction of energetic electrons with matter at the atomic level. As an X-ray beam passes through an object, (i) it can penetrate the section of the matter without any interaction (i.e. Thompson scattering); (ii) it can interact with the matter and totally be absorbed by the atoms of the matter (i.e. photoelectric effect) or (iii) it can interact partially with the matter and be scattered from its original direction in all directions (i.e. Compton scattering). Hence, there is no doubt that X-ray shielding requirements have become more stringent as standards for exposure of personnel (patient and radiographer worker) and the general public during the diagnosis examination is carried out.

1.1 Introduction

1.1.1 Background

Radiation (X-ray/gamma-ray) shielding is an age-old problem and has been studied in greater details up till now, due to their interactions being most prominent in many applications such as in medical fields (i.e. diagnostic imaging and therapy). X-rays/gamma-rays are the most penetrating of ionizing radiation that is known to be harmful to human health and heredity. X-ray photons are produced by the interaction of energetic electrons with matter at the atomic level. As an X-ray beam passes through an object, (i) it can penetrate the section of the matter without any interaction (i.e. Thompson scattering); (ii) it can interact with the matter and totally be absorbed by the atoms of the matter (i.e. photoelectric effect) or (iii) it can interact partially with the matter and be scattered from its original direction in all directions (i.e. Compton scattering). Hence, there is no doubt that X-ray shielding require-

© Springer Nature Singapore Pte Ltd. 2020

I. M. Low and N. Z. Noor Azman, *Polymer Composites and Nanocomposites for X-Rays Shielding*, Composites Science and Technology,
https://doi.org/10.1007/978-981-13-9810-0_1

ments have become more stringent as standards for exposure of personnel (patient and radiographer worker) and the general public during the diagnosis examination is carried out.

To overcome the danger of X-rays, the material chosen for X-ray shielding must have a criterion to totally absorb the transmitted and the scattered X-ray from exposure of personnel and the general public. Hitherto, lead glass is the well-known material for X-ray shielding either for diagnostic or therapeutic examinations, but it is heavy, expensive, and extremely brittle. Thus, it is not surprising that the application of polymers in X-ray shielding technology is increasing steadily since polymers also have an enormous potential in many crucial applications that glass could not meet because of their unique properties such as the ability to form intricate shapes, optical transparency, low manufacturing cost, and toughness.

This book focuses mainly on the nanotechnology advances in designing electromagnetic radiation (focused on X-ray) shielding materials. It covers viable processing methodologies with the new material's design concept to enhance radiation shielding purposes to meet the safety requirements for use in medical X-ray imaging facilities.

In this book, we describe a simple sample preparation procedure for dispersing different types of micro-sized and nano-sized particles into polymeric materials by different methods such as melt-mixing, ion-implantation and electrospinning method. Accurate and effective melt-mixing method was becoming increasingly important so that a uniform mixture will be produced. Whilst, the ion-implantation technology is capable of precisely controlling the number of implanted ions into the material. Meanwhile, electrospinning is a method which provides advantageous to use the nanofiber webs in a layered structure together with a suited substrate material and offers sufficient strength and durability. Such, the final products produced have high potential applications for shielding of ionizing radiations such as X-rays and gamma-rays.

The X-ray attenuation ability of the fabricated composites was studied by means of X-ray transmission or X-ray attenuation coefficient determinations for the X-ray energy ranges used in the diagnostic examination by three separate equipments, i.e. general radiography unit, mammography unit and X-ray Absorption Spectroscopy (XAS).

This work seeks to gain a better understanding of fabricating new polymer composites with good filler dispersion for the usage as an X-ray shielding material. This research program led to in-depth analysis of synthesis methods, X-ray attenuation ability and characterization of these polymer composites.

1.1.2 Organisation of Chapters

This book consists of eleven chapters where background, literature review and research aims are introduced in this chapter. Meanwhile, the methodology to fabricate the samples by dispersing different types of micro-sized and nano-sized particles into polymeric materials using different methods such as melt-mixing, ion-implantation

and electrospinning method, together with the test methods to measure the physical, mechanical and X-ray attenuation ability of the fabricated X-ray shielding samples are presented in Chap. 2.

Chapter 3 describes the preliminary investigation of the filler dispersion within an epoxy matrix since the comprehensive literature survey reveals that the gamma/X-ray shielding characteristics of the filler (PbO and Pb_3O_4)-reinforced epoxy resins have not been attempted. This analysis allowed for the discussion of the effects of filler loadings on the density, phase composition, and morphology of the epoxy composites. Moreover, the X-ray attenuation by the samples was performed using calibrated general diagnostic radiography unit.

In Chap. 4, further analyses of filler-reinforced epoxy resins are reported. This work comprises similar characterizations of the synthesized different species of filler ($PbCl_2$, WO_3 and Bi_2O_3)-epoxy composites as in Chap. 3 including the discussion of their mechanical properties. In addition, the feasibility of these composites for use in X-ray shielding purpose is compared with the commercial lead glass. Meanwhile, Chap. 5 reveals the effect of particle size, filler loadings and X-ray tube voltage on the X-ray transmission of the WO_3-epoxy composites. For this study, a mammography and a diagnostic radiography unit were used which comprised of variable X-ray tube voltages 25–120 kV. Then, Chap. 6 is the continuous analysis of Chap. 5 which provides the X-ray transmission results from XAS and also some mechanical and microstructural analyses on the samples included.

Chapters 7 and 8 report the fabrication of filler-polymers matrix (epoxy, acrylic and glass) using ion-implantation. Heavy elements such as Pb, W and Au ions were implanted on the polymer matrix since they are a well-known candidate for X-ray shielding material. A comparative study of the near surface composition depth profiling of the implanted samples was performed using ion beam analysis (Rutherford backscattering spectroscopy). Moreover, the comparative X-ray attenuation analysis of the samples was performed using calibrated general diagnostic radiography unit.

The third final episode (Chap. 9) of this book is the presentation of a novel electrospinning method to fabricate the filler-polymer nanofiber mats. Poly lactic acid (PLA) was used as the matrix for nanofiber mat synthesis due to its advantages for the electrospinning process. This work presents the performance of PLA nanofiber mat embedded with different particle sizes for X-ray transmission study. A better understanding was gained by the comparative study using solution casting method to synthesize same composition of similar composites but in a thin film form.

Meanwhile, the second final episode (Chap. 10) of this book is about the effect of particle sizes and addition of starch into filler–polymer composites for X-ray shielding purpose. The X-ray transmission analysis of the prepared samples was done using X-ray fluorescent spectroscopy (XRF) and mammography unit. A preliminary investigation of the effect of starch addition into the polymer composite on the X-ray transmissions by different particle sizes of polymer composites was also studied. Polyvinyl alcohol (PVA) was used as the matrix due to its exclusive chemical and physical features. Starch was added in the mixture of filler-polymer composite since it seems to be a very good substrate for preparation of nanoparticles and improving the dispersion of nanoparticles within the polymer matrix.

In the final chapter (Chap. 11), the results obtained in this work are summarised. The challenges and future research directions in this field are highlighted in the concluding remarks.

1.2 Literature Review

1.2.1 Historical Foundations of X-Ray Shielding

During the early part of the 20th century, once the X-ray was discovered by Wilhem Röntgen in 1895, the potential hazards of ionizing radiation (especially X-rays/gamma-rays) were recognized and thus, radiation protection has evolved into an elaborate infrastructure of controls and disciplines specifying how this shield should be deployed [1–3]. Recently, X-ray shielding requirements have become more stringent as standards for exposure of personnel and the general public have been reviewed. Lead is the first material used as a shielding for X-ray since it possesses high atomic number (Z) which is mandatory to absorb the unwanted radiation. Once the danger of lead has become a major concern, many researchers have attempted to fabricate polymer composite in order to replace lead as the main radiation shielding material. X-ray technologists practice a principle called as-low-as-reasonably-achievable (ALARA) dose when dealing with X-rays, so that radiation dose received by personnel and the general public can be as low as possible [4–7].

In addition, by the extensive use of nuclear energy and radioactive isotopes in various fields' such as reactors, nuclear power plants, nuclear engineering and space technology, the radiation shielding became an important subject due to required proper precautions to avoid from the radiation hazards [1]. However, this book covered only the preparation and fabrication of the radiation shielding material focused on the X-rays with the energy of the diagnostic ranges.

1.2.2 X-Ray Attenuation

The meaning of attenuation is reducing the X-ray beam intensity as it pass through specific material. This reduction occurs either by scattering or absorption. *Several researchers have focused their efforts on studying how to measure the X-ray attenuation on an absorbing material. Whereas most researchers who examine this issue tried to measure and calculate the photon (X-rays/gamma-rays) attenuation coefficient of the absorbing material and made a comparison with the theoretical value tabulated from NIST XCOM* [8–15]*, while the other take the direct X-ray transmission results as an approach* [16–18].

In particular, the former can be measured for specific X-ray energy for a narrow beam geometry setup as shown in Fig. 1.1. The reduction in the X-ray beam intensity

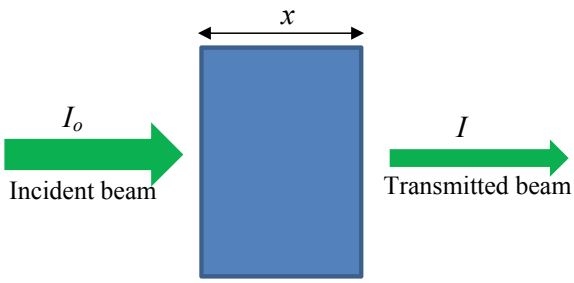

Fig. 1.1 Schematic illustration of a narrow beam geometry setup for measurement of X-ray attenuation process

(X-ray attenuation) for the absorbing material at that specific X-ray energy studied is measured by determining an X-ray attenuation coefficient which expressed the quantity of attenuated X-ray beam passing through specific thickness of shielding material [19].

There are two main X-ray attenuation coefficients used to determine the quantity of attenuated X-ray beam. These coefficients are linear attenuation coefficient (μ) and mass attenuation coefficient (μ_m). Each one of these coefficients depend on specific prosperity of absorbing material. Firstly, μ expresses the exponential change in the intensity of X-ray beam per thickness unit of absorbing material [19]. It has the dimensions of an inverse length (1/cm) and it represent the summation of three types of X-ray interactions which are photoelectric effect, Compton scattering and pair production. Monochromatic X-ray photons collimated into a narrow beam are attenuated through an absorbing material according to Beer Lambert's law as stated in Eq. (1.1) [20]:

$$\mu = \frac{(-\ln \frac{I}{I_o})}{x} \tag{1.1}$$

where I_o is the incident X-ray intensity, I is the attenuated X-ray photon intensity, μ is the linear attenuation coefficient and x is the thickness of the absorbing material as illustrated in Fig. 1.1. In order to measure the X-ray attenuation ability regarding to the physical state of the absorbing material, the mass attenuation coefficient (μ_m) is the preferred to be used and is obtained by dividing the μ by the density of the absorbing material (ρ) according to the following Eq. (1.2) [20]:

$$\mu_m = \frac{\left(-\ln \frac{I}{I_o}\right)}{x\rho} \tag{1.2}$$

There are another two types of X-ray attenuation coefficients used to determine the quantity of attenuated X-ray beam which are atomic attenuation coefficient (μ_a) and electronic attenuation coefficient (μ_e). The former coefficient, μ_a represents the fraction of attenuated beam by single atom of absorbing material which is obtained by dividing the μ_m by the number of material's atoms per gram. On the other hand,

the latter coefficient, μ_e represents the fraction of attenuated beam by the number of material's electrons per gram which is obtained by dividing the μ_m by the number of material electrons per gram [19].

For instance, Hussain et al. (1997) have studied the shielding properties of polyethylene glycol-lead oxide composite for Co-60 gamma-ray source [21]. They calculated the linear attenuation coefficient, μ from the plot of log of the count rate versus the composite thickness (X) using Eq. (1.3):

$$\text{Log}\, I(X) = \text{Log}\, I_o - \mu X \tag{1.3}$$

where $I(X)$ = count rate for the radiation that has not been involved in any collision during passage through the composite, I_o = count rate in the absence of shielding material and μ = linear attenuation coefficient, is the slope of the plot [22]. In their case, they did not compare the attenuation coefficient results with the theoretical tabulated from XCOM [16]. Meanwhile, using a similar method, Harish et al. [11] have investigated the radiation shielding properties of gamma-rays from Ba-133, Cs-137 and Co-60-point sources of lead oxide (PbO, PbO_2 and Pb_3O_4) with different concentrations filled isophthalic resin polymer composites. They found that the attenuation coefficient of the composite at the specific gamma-rays energy and found that experimental results are in a good agreement with the theoretical tabulations [16] under acceptable error.

Whereas, it would be much more useful to present the X-ray transmission (i.e. measured intensities through absorbing material divided by the measured intensity in the same configuration with absorbing material absent) over the full energy range (weighted by an appropriate model for X-ray tube spectrum) if the thickness of the absorbing materials is fixed. Absolute intensities obviously depend on the mAs setting, distance from source to detector, detector calibration etc. [23]. Usually, this direct transmission measurements were done for the polychromatic X-ray energies since by quoting these measurements would correct for all the effects [17, 18, 23, 24]. Some examples of X-ray transmission through the nanosized filler/polymer samples versus X-ray tube voltages containing polychromatic X-ray energies were studied by many researchers such as Kűnzel et al. (2012) in which they studied the X-ray transmission of nanosized CuO-epoxy resin samples at various X-ray tube voltages [18].

1.2.3 X-Ray Interactions with Matter

Generally, there are three possible X-ray interactions happen in an absorbing material as shown in Fig. 1.2 which are:

(1) Scattering—An X-ray photon will interact with an atom of absorbing material and it will be deflected. Depending on the case, it may or may not loss of energy.

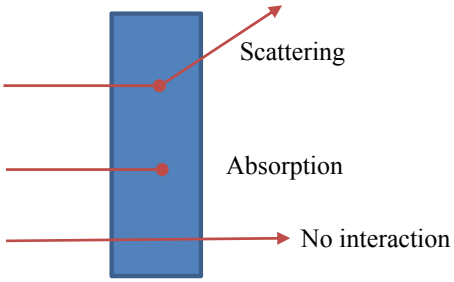

Fig. 1.2 Possible X-ray interactions happen in the material

(2) Absorption—An X-ray photon will interaction with an atom of absorbing material and will loses all of its energy to the atom.
(3) No interaction/penetration—An X-ray photon just passes through the absorbing material without interacting with any atoms of absorbing material.

These possible interactions are categorized into five different types of X-ray interaction with matter in which must be considered in radiological physics as listed below:

a. Photoelectric effect
b. Compton scattering effect
c. Pair production
d. Rayleigh scattering
e. Photonuclear interactions.

The first three types of X-ray interaction are the most important since their interactions result in the transfer of energy to electrons and then imparted to matter along their tracks. These interactions depend on both photon energy E and atomic number Z of the absorbing material.

The photoelectric effect is dominant at the lower photon energies while the Compton scattering effect takes over at medium energies (200 keV to about 10 MeV). Pair production is leading at the higher photon energies (above 10 MeV). Compton scattering effect domination is very broad for low Z of absorbing material and gradually narrow with increasing Z. At a given photon energy, the relative probability of two processes would be the ratio of their cross sections.

The Rayleigh scattering is an elastic interaction in which the photon is merely redirected through a small angle with no energy loss. The last interaction (photonuclear) is only significant for photon energies above a few MeV.

Further discussions only related to photoelectric effect and Compton scattering effect since both take part in the photon energy ranges studied for this book.

(a) *Photoelectric effect*

Photoelectric effect is the most important interaction to concern during the interaction of low energy photons with matter (Fig. 1.3). During photoelectric interaction, an inelastic collision occurred between the incident X-ray photon with an orbiting electron (inner shell electron). The photon gives up all of its energy and therefore

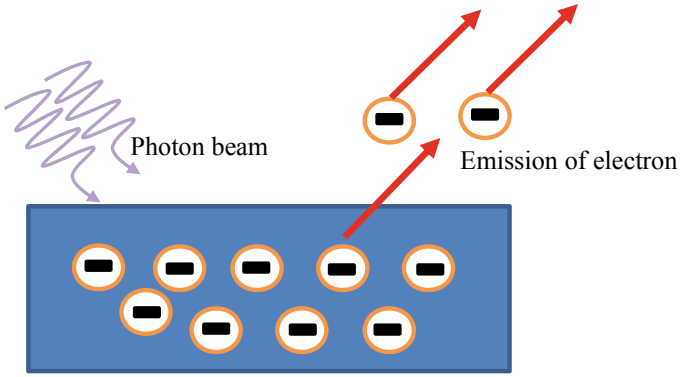

Fig. 1.3 Process of photoelectric effect in an absorbing material

disappears (absorbed by the electron). Then, the electron is ejected from the atom and flies off into space as photoelectron which may undergo another interaction with the atom. The vacancy left is immediately filled by an electron from the outer shell. The quantum 'jumps' of the electron producing a characteristic radiation which is equal to the energy difference between shells. The photoelectric effect always yields three end products: (1) characteristic radiation; (2) a negative ion (photoelectron); and (3) a positive ion (an atom deficient one electron) [25–27].

The probability of the photoelectric effect is inversely proportional to the cube of the X-ray energy $(1/E)^3$ and directly proportional to the cube of the atomic number of the absorbing material Z^3.

(b) *Compton scattering effect*

Almost all the scatter radiation that encounter in diagnostic radiology comes from Compton scattering. During this interaction, an incident photon of relatively high energy strikes a loosely bound outer shell electron, ejecting it from its orbit. The photon is then deflected by the electron and travel in a new direction as scatter radiation with part of its original energy. The reaction produces an ion pair of a positive atom and a negative ion (outgoing/recoil electron) [28]. Figure 1.4 shows the process of Compton scattering interaction.

The probability of Compton scattering depends directly on the number of electrons (i.e. density) within the absorbing material. Compton scattering represent the greatest percentage of occupational exposure for radiation workers in the diagnostic energy level [29].

1.2.4 X-Ray Energy

X-rays are the most penetrating of ionizing radiation following gamma-rays that are known to be harmful to human health and heredity. They are emitted by excited atoms

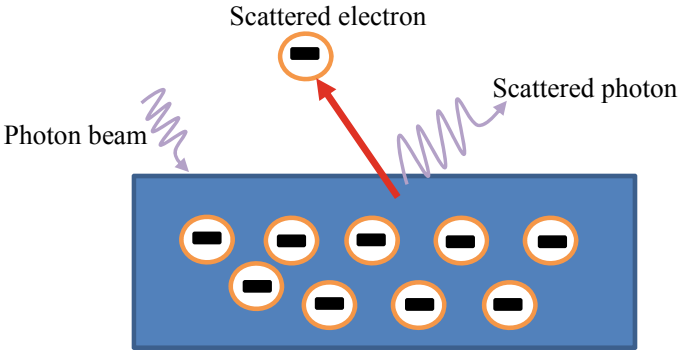

Fig. 1.4 Process of Compton scattering in an absorbing material

in the process of de-excitation to a ground state by means of electrons changing atomic energy levels (characteristic or fluorescence X-rays) or by an ion or a charged particle when a negative acceleration is applied to it (slowing down in a Coulomb force field or changing direction (continuous or bremsstrahlung X-rays). Most commonly, the energy ranges of X-rays are classified as follows (in terms of the generating tube voltage) [26]:

- 0.1–20 kV Low energy or "soft" X-rays
- 20–140 kV Diagnostic-range X-rays
- 140–300 kV Orthovoltage X-rays
- 300 kV–1 MV Intermediate-energy X-rays
- 1 MV upward Megavoltage X-rays.

Table 1.1 provides the accelerating voltage and the target material used to produce X-rays vary depending on the specific applications for the diagnostic-range X-ray energies (20–140 keV) since this energy range is related to this book.

Basically, these X-ray energy ranges are classified as polychromatic and monochromatic X-rays. Polychromatic X-rays are a broad spectrum of X-ray energies having various wavelengths, the expected form of X-ray generated in clinical

Table 1.1 The accelerating voltage and the target material used to produce X-rays vary depending on the specific applications [30]

Use		Accelerating voltage (kV)	Target	Source type	Average photon energy (keV)
Diagnostic X-rays	Mammography	20–30	Rhodium, Molybdenum	Tube	20
	Dental	60	Tungsten	Tube	30
	General	40–140	Tungsten	Tube	40
	CT	80–140	Tungsten	Tube	60

practice. Meanwhile, monochromatic X-ray is an X-ray with exclusively a single wavelength [31, 32]. As for the diagnostic X-rays, average photon energy was measured using half-value layer (HVL) experiment [33] for each of the accelerating voltage used for the specific applications. This average photon energy is an important parameter for further attenuation coefficient comparison between the measured value of the experiment and the tabulated data NIST XCOM [16].

1.2.5 Effect of Particle-Size on X-Ray Attenuation

Currently, it was demonstrated that materials at the nanoscale have unique physical and chemical properties compared to their bulk counterparts and these properties are highly promising for a variety of technological applications. Hence, there are no doubts that numerous analytical methods have been developed to investigate the effect of particle size of a material on the X-ray attenuation for various incoming X-ray energy ranges including the scattered photons [2, 5, 11, 34–41]. Some X-ray technologists believed that nano-sized particles will disperse more uniformly within the matrix with fewer agglomerations when compared to micro-sized particles and consequently affected the density and composition that modify the X-ray attenuation ability of the material [2, 17, 42]. In addition, nanomaterials have unique material properties that can be exploited to develop novel lead-free radiation-protection materials.

For instance, Hołyńska (1969) found that the intensity of scattered radiation increases with increasing grain size [34]. This size-effect has been observed in a sand matrix and for samples containing heavy elements such as iron or barium [34]. Moreover, the latest work done by Buyuk et al. (2012) proved that decreasing the titanium diboride particle size in the titanium diboride reinforced boron carbide-silicon carbide composites results in a higher linear attenuation coefficient for the energy of 0.662 MeV emitted by a Cs-137 gamma source [43]. In a complementary finding, a recent study by Botelho et al. (2011) showed that nanostructured copper oxide (CuO) is more effective in attenuating X-ray beams generated from lower tube voltages (i.e. 26 and 30 kV), whilst no significant variation in the attenuation of the X-ray beams generated from higher tube voltages (i.e. 60 and 102 kV) were observed [17].

Künzel and Okuno (2012) also provided similar results, showing that the X-ray beam attenuation is greater for a nanostructured CuO compound incorporated to a polymeric resin compared to the microstructured counterpart for low energies of tube voltages (25 and 30 kV) for a range of 5, 10 and 30% CuO concentrations incorporated into polymeric resins [44]. They found that the sample of 5, 10 and 30% nanostructured CuO incorporated to a polymeric resin absorbs more low energy photons (25 and 30 kV tube voltages) compared to the microstructured ones. Meanwhile, for the X-ray beams produced at 60 and 120 kV tube voltages, a minimal difference, less than 2%, in the X-ray transmission through the nanostructured and microstructured materials is observed [44].

1.2.6 Advantages and Disadvantages of Commercial Lead Glass

X-ray shielding lead glass is utilized in medical and industrial applications so that the operator can view the part or patient without being exposed to X-ray or Gamma-ray. To provide viewing of the patient in the X-ray room while providing protection to the operator, lead glass viewing windows can be furnished in the barrier. In most cases, the X-ray attenuation of the glass must be at least equal to the wall or barrier in which the window is installed. It can be installed in multiple layers so as to provide the same lead equivalency as the wall [45–47].

Lead glass ensures excellent protection against gamma and X-rays. Its effectiveness for X-ray shielding increases the attenuation of ionizing photons emitted by X-ray equipment, because this property increases dramatically as the atomic number of the attenuating material increases. Lead has a high atomic number which is further increases the density of lead glass, thus increasing the attenuation of X-ray photons. X-rays used in medical applications, specifically diagnostic X-rays, often have lower energies on the ionizing radiation spectrum, which are easily shielded by leaded glass [46].

Lead glass utilizes lead in the form of more than 65% lead oxide into a glass during the manufacturing process. It is transparent and easy to see through for observation purposes since it is made of high-quality optical grade material. It also offers a high refractive index and high light transmission with little to no distortion, even in the thickest available varieties, delivers superior visual clarity and does not discolor due to radiation. One important advantage during everyday use is that the glass resists scratches much better than plastic since it has hard and polished both surfaces (using Mohs' hardness scale tests at Level 6 which compatible to feldspar, a constituent of granite) [48]. It also is an incombustible material and has a high chemical resistance as well [45–48].

Even though lead glass provides good X-ray attenuation ability, but it also still has some disadvantages or limitations. Lead glass transmits more light, thereby it will create more annoying reflections causing eye strain to medical personnel. Moreover, it is very fragile and easily breakable or can shatter into sharp pieces if not handled with care. It is also a heavy and very expensive material. In addition, it cannot be tempered as it is physically impossible due to its low melting temperature and surface characteristics. During shipment, it is more prone to breakage, so it must be shipped on its edge and never laid flat. Crates must not be stacked upon or dropped [47]. Due to these drawbacks, many researchers are seeking a new safely, rigid and not heavy radiation shielding material. One of the advanced contributions is using polymer composites to fabricate new radiation shielding material [49].

Table 1.2 Lead equivalencies, thicknesses and densities of lead acrylic used as X-ray shielding [52]

Lead equivalency (mm)	Thickness (mm)	Weight (lb./ft)
0.3	7	2.3
0.5	12	3.9
0.8	18	5.9
1.0	22	7.2
1.5	35	11.5
2.0	46	13.7

1.2.7 Other Commercial Polymer Composites for X-Ray Shielding

Recently, several significant research efforts have been focused toward designing efficient, stronger, lightweight, cost-effective, and flexible shielding materials for protection against radiation encountered in medical X-ray either for diagnosis or treatment. In this regard, polymer composites have become attractive candidates for developing materials that can be designed to effectively attenuate photon or particle radiation. Here are some commercial polymer composites used nowadays for X-ray shielding purposes.

(a) *Lead acrylic*

Lead acrylic is made from an acrylic copolymer resin into which lead is chemically introduced as an organo-lead salt compound. It is a unique, versatile, transparent plastic that contains 30% lead weight and has a constant density of 1.6 gm/cm^3 with a refractive index of 1.54. It combines superb light transmission with effective radiation protection. Recently, it has been widely used as the substitution for lead glass as the observation viewing windows and intercommunication windows, door glazing, panoramic glazing, mobile shielding protection or protection panels for check-up systems [50, 51]. Lead equivalencies, thicknesses and densities of lead acrylic are summarized in Table 1.2 [52].

For the same lead equivalent, lead acrylic has to be approximately 5 times thicker than lead glass, significantly reducing observation capabilities. For example, 2.0 mm lead glass would be 5/16″ thick and lead acrylic would be approximately 1–1/2″ thick for the same protection.

(b) *X-ray lead vinyl*

X-ray lead vinyl is more suitable for use in low energy X-ray/gamma radiation reduction. It is flexible and pliable for a wide variety of applications such as a lead vinyl curtain since it has uniform density for a consistently dependable shielding value and is very durable and abrasion resistant for everyday use. Moreover, it has a high acid/alkali resistance and it is smooth and easy to clean its surfaces on both sides [53]. Table 1.3 shows the lead equivalence shielding value for a specified lead vinyl thickness.

Table 1.3 Lead equivalence shielding value for a specified lead vinyl thickness [53]

Lead vinyl thickness (mm)	Lead equivalence shielding value (mm)
0.8	0.25
1.6	0.50
3.2	1.00

(c) *Poly tungsten*

Poly tungsten or also known as the tungsten—filled polymer is a composition of various resins and tungsten powder which are mixed together through special metallurgical technology. The resins may include acrylonitrile butadiene styrene (ABS), polypropylene (PP), polybutylene terephthalate (PBT), polyamide (PA), polyurethane (PU), and thermoplastic elastomer (TPE). Poly tungsten has a high density of more than 11.34 g/cm^3 which provide a perfect radiation shielding performance since tungsten has comparable radiation shielding ability as a lead but is less hazardous than lead. The poly tungsten is made of non-toxic and recyclable materials and produces no pollution to the environment. To date, many manufacturers, especially those in the medical industry, are trying to replace lead radiation shielding products with poly tungsten products. Furthermore, it has good flexibility and excellent workability in which the poly tungsten sheets can be cut or holed with household scissors and formed into shapes with various curved surfaces [54, 55].

Tungsten-filled polymers can replace lead in radiation shielding applications such as X-ray equipment and CT scanning devices, tungsten poly syringe, tungsten poly collimator, radiation-protective clothing, etc. Testing, both on prototypes and actual products already in use, has proven that our tungsten-filled polymer products provide radiation shielding better than lead material radiation shielding without leakage or hot spots [54].

(d) *Hybrid polymer X-ray shielding material*

The hybrid polymer X-ray shielding material is a chemical compound of many organic and inorganic materials so that it is able to shield X-ray radiation. This X-ray radiation shielding material can be used in many areas like in research laboratories, in medicine, industry, agriculture or military. It has many advantages over lead shielding plates. Apart from being able to stop the X-ray, it is lighter and can shape easier than lead plates and also it is economic. Another important specification of this hybrid polymer X-ray shielding material is it is not toxic to human beings and for the environment [56].

(e) *Other polymer composites*

In the meantime, many researchers tried to prepare new polymer composites for X-ray shielding purposes too. For instance, Harish et al. (2009) have prepared lead monoxide-polyester [12] and also lead oxide-isophthalic resin (ISO) [11] for gamma radiation shielding applications. The lead monoxide-polyester composites were observed to exhibit excellent % of heaviness and half value layer in comparison

with other conventional materials [12]. Meanwhile, the lead monoxide-ISO composites when compared to conventional shielding materials perform as strong contenders to barite, steel and concrete at low gamma ray energies. Even at higher gamma ray energies considered, they perform satisfactorily and are very much comparable to steel and concrete [11].

Nambiar et al. (2011) have prepared polydimethylsiloxane (PDMS) composites with different weight percentages (wt%) together with the following high atomic-number (Z) materials: (i) bismuth tungsten oxide (BTO), (ii) bismuth oxide (BO) [57]. X-ray attenuation tests were performed using the diagnostic X-ray machine (Ysio, Siemens) for voltages from 40 to 150 kV. PDMS composite with 36.36 wt% of BTO shows an overall increase of 18.3 and 50% attenuation relative (absolute differential between the % attenuation) to that achieved by 18.18 wt% of BTO and pure PDMS (no BTO) respectively. A composite sample with 60.6 wt% of BO (thickness of 2.67 mm) has shown the best result, by far, with 92.5% attenuation of the beam at 60 kV [57].

Furthermore, polymer-based nanocomposites for shielding against diagnostic X-rays were developed. For instance, Nambiar et al. (2013) succeeded in fabricating polydimethylsiloxane/bismuth oxide (PDMS/BO) nanocomposites by using different weight percentages (wt%) of bismuth oxide (BO) nanopowder [49]. The X-ray attenuation properties of the nanocomposites were characterized using diagnostic X-ray energies from 40 to 150 kV tube potential and were compared to the attenuation characteristics of 0.25-mm-thick pure lead sheet. The PDMS/BO nanocomposite (44.44 wt% of BO and 3.73-mm thick) was capable of attenuating all the scattered X-rays generated at a tube potential of 60 kV, which is the beam energy commonly employed in interventional radiological IVR [49].

References

1. Archer B (1995) History of the shielding of diagnostic X-ray facilities. Health Phys 69(5):750–758
2. Archer B (2005) Recent history of the shielding of medical X-ray imaging facilities. Health Phys 88(6):579–586
3. Archer BR, Thornby JI, Bushong SC (1983) Diagnostic X-ray shielding design based on an empirical model of photon attenuation. Health Phys 44(5):507–517
4. Experiments with medium- Z materials for shielding against low-energy X rays 1966
5. Erdem M et al (2010) A novel shielding material prepared from solid waste containing lead for gamma ray. Radiat Phys Chem 79(9):917–922
6. Kurudirek M et al (2010) Comparison of some lead and non-lead-based glass systems, standard shielding concretes and commercial window glasses in terms of shielding parameters in the energy region of 1 keV–100 GeV: a comparative study. J Nucl Mater 407(2):110–115
7. Okunade AA (2002) Comparison of lead attenuation and lead hardening equivalence of materials used in respect of diagnostic X-ray shielding. Appl Radiat Isot 57(6):819–824
8. Baltaş H et al (2007) Measurement of mass attenuation coefficients and effective atomic numbers for superconductor using X-ray energies. Radiat Meas 42(1):55–60
9. Gerward L (1992) Theoretical upper and lower limits to experimental X-ray attenuation coefficients. Nucl Inst Methods Phys Res B 69(4):407–412

10. Gowda S et al (2004) Photon mass attenuation coefficients, effective atomic numbers and electron densities of some thermoluminescent dosimetric compounds. Pramana—J Phys 63(3):529–541
11. Harish V, Nagaiah N, Kumar H (2012) Lead oxide filled isophthalic resin polymer composites for gamma radiation shielding applications. Indian J Pure Appl Phys 50:847–850
12. Harish V et al (2009) Preparation and characterization of lead monoxide filled unsaturated polyester based polymer composites for gamma radiation shielding applications. J Appl Polym Sci 112(3):1503–1508
13. Içelli O, Erzeneoglu S, Boncukçuoglu R (2003) Measurement of mass attenuation coefficients of some boron compounds and the trommel sieve waste in the energy range 15.746–40.930 keV. J Quant Spectrosc Radiat Transf 78(2):203–210
14. Içelli O, Erzeneoglu S, Boncukçuoglu R (2004) Experimental studies on measurements of mass attenuation coefficients of boric acid at different concentration. Ann Nucl Energy 31(1):97–106
15. Tran C, Chantler C, Barnea Z (2003) X-ray mass attenuation coefficient of silicon: theory versus experiment. Phys Rev Lett 90(25) Pt 1:257401
16. Berger M et al (2010) XCOM: photon cross section database (version 1.5). National Institute of Standards and Technology, Gaithersburg, MD. http://physics.nist.gov/xcom
17. Botelho M et al (2011) X-ray transmission through nanostructured and microstructured CuO materials. Appl Radiat Isot 69(2):527–530
18. Künzel R, Okuno E (2012) Effects of the particle sizes and concentrations on the X-ray absorption by CuO compounds. Appl Radiat Isot 70(4):781–4
19. Mcketty H (1998) The AAPM/RSNA physics tutorial for residents. X-ray attenuation. Radiographics 18(1):151–163
20. Hosseini SH, Noushin Ezzati S, Askari M (2015) Synthesis, characterization and X-ray shielding properties of polypyrrole/lead nanocomposites. Polym Adv Technol 26(6):561–568
21. Hussain R, Haq ZU, Mohammad D (1997) A study of the shielding properties of poly ethylene glycol-lead oxide composite. J Islamic Acad Sci 10(3):81–84
22. Hussain R, Haq Z, Mohammad D (1997) A study of the shielding properties of poly ethylene glycol-lead oxide composite. J Islamic Acad Sci 10(3):81–84
23. Tickner J (2000) Modelling detector responses to neutrons using MCNP. Paper presented to advanced Monte Carlo for radiation physics, particle transport simulation and applications. Proceedings of the Monte Carlo 2000 conference, Lisbon, Spain, 23–26 Oct 2000
24. Al-Maamori MH, Al-Bodairy OH, Saleh NA (2012) Effect of PbO with rubber composite on transmission of (X-ray). Acad Res Int 3(3):113–119
25. *X-ray Interaction* (*Part I*), viewed 31 January 2013, http://newton.ex.ac.uk/teaching/resources/jjm/pam2011/Lectures/Xray%20Interaction%201.pdf
26. Attix F (1986) Introduction to radiological physics and radiation dosimetry. Wiley, New York
27. Abdel-Rahman W, Podgorsak EB (2010) Energy transfer and energy absorption in photon interactions with matter revisited: a step-by-step illustrated approach. Radiat Phys Chem 79(5):552–566
28. Chapter 6 Modern Technology, 2012, viewed 22 May 2013, http://www.physics.hku.hk/~phys0607/lectures/chap06.html
29. Palmer C (2013) Interaction of radiation with matter. Health Phys 104(2):234
30. X-rays 2012, Australian radiation protection and nuclear safety Agency, viewed 16 Apr 2013, http://www.arpansa.gov.au/radiationprotection/basics/xrays.cfm
31. Hoheisel M, Bernhardt P, Lawaczeck R, Pietsch H (2006) Comparison of polychromatic and monochromatic X-rays for imaging. Proc SPIE 6142:71–78
32. Martínez Ripoll M, Félix Hernández C (2013) X-rays, viewed 04 June 2013, http://www.xtal.iqfr.csic.es/Cristalografia/parte_02-en.html
33. Suk CC, Wei LJ, Harun AZ (2012) Evaluation of X-ray beam quality based on measurements and estimations using SpekCalc and Ipem78 models. Malays J Med Sci 19(3):22–28
34. Hołyńska B (1969) Grain size effect in low energy gamma and X-ray scattering. Spectrochim Acta Part B 24(1):85–93

35. Huang X, El-Sayed MA (2010) Gold nanoparticles: optical properties and implementations in cancer diagnosis and photothermal therapy. J Adv Res 1(1):13–28
36. Jackson P, Periasamy S, Bansal V, Geso M (2011) Evaluation of the effects of gold nanoparticle shape and size on contrast enhancement in radiological imaging. Australas Phys Eng Sci Med
37. Patra CR, Bhattacharya R, Mukhopadhyay D, Mukherjee P (2010) Fabrication of gold nanoparticles for targeted therapy in pancreatic cancer. Adv Drug Deliv Rev 62:346–361
38. Popov A (2009) Sun protection using nanoparticles. SPIE Newsroom 24:1–2
39. Sahare PD, Ranju R, Numan S, Lochab SP (2007) $K_3Na(SO_4)_2$: Eu nanoparticles for high dose of ionizing radiation. J Phys D Appl Phys 40(3):759
40. Van Den Heuvel F, Locquet JP, Nuyts S (2010) Beam energy considerations for gold nanoparticle enhanced radiation treatment. Phys Med Biol 55(16):4509–4520
41. Wang T, Liu Z, Lu M, Wen B, Ouyang Q, Chen Y, Zhu C, Gao P, Li C, Cao M, Qi L (2013) Graphene-Fe_3O_4 nanohybrids: synthesis and excellent electromagnetic absorption properties. J Appl Phys 113(2):024314–024318
42. Steinhart M (2004) Introduction to nanotechnology. By Charles P. Poole, Jr. and Frank J. Owens. Angew Chem Int Ed 43(17):2196–2197
43. Buyuk B, Tugrul AB, Akarsu AC, Addemir AO (2012) Investigation on the effects of titanium diboride particle size on radiation shielding properties of titanium diboride reinforced boron carbide-silicon carbide composites. J Nano Electron Phys 4(1):01010(1)-(4)
44. Künzel R, Okuno E (2012) Effects of the particle sizes and concentrations on the X-ray absorption by CuO compounds. Appl Radiat Isot 70(4):781–784
45. Data sheet lead glass (X-ray protection), UQG Optics, viewed 31 May 2013, http://www.uqgoptics.com/pdf/Lead%20Glass.pdf
46. Lead glass for X-ray/radiation shielding, 2009, viewed 31 May 2013, http://www.afabxray.com/lead_glass.htm
47. Lead X-ray glass vs. lead plastic acrylic, 2013, viewed 31 May 2013, http://www.marshield.com/nuclear-shielding/leaded-x-ray-shielding-glass-andacrylic
48. Leaded glass for X-ray shielding, viewed 31 May 2013, http://www.drct.com/dss/shielding/leadglass.html
49. Nambiar S, Osei EK, Yeow JTW (2013) Polymer nanocomposite-based shielding against diagnostic X-rays. J Appl Polym Sci 127(6):4939–4946
50. Lead Acrylic, 2013, viewed 31 May 2013, http://marshield.com/medical shielding/leadacrylic/
51. Wardray 2005–2011, Premac lead acrylic, part of the Wardray premise total radiation shielding package. Wardray Premise Ltd., viewed 4 May 2011, http://wardraypremise.com/structural/materials/premac.html
52. Control Windows, 2000–2010, viewed 31 May 2013, http://www.raybar.com/cntrl_wndws.htm#clr_acryl
53. Other ray-bar products, 2000–2010, viewed 14 April 2013, http://www.raybar.com/other_prd.htm
54. Poly tungsten radiation shielding, 1997–2013, viewed 31 May 2013, http://www.poly-tungsten.com/Tungsten-poly-radiation-shielding.html
55. Tungsten Products: Poly Tungsten, viewed 14 April 2013, http://www.stanfordmaterials.com/poly-tungsten.html
56. Hybrid polymer X-ray shielding material, 2010, viewed 24 June 2013, http://www.canlaser.com/en/XRay.aspx
57. Nambiar S, Osei E, Yeow J (2011) MO-F-BRA-01: polymer composite-based shielding of diagnostic X-rays. Med Phys 38(6):3720

Chapter 2
Materials and Methodology

Abstract Various composite samples were prepared by mixing lead oxide, bismuth oxide or tungsten oxide of either nano-sized or micro-sized with epoxy resin, acrylic, PLA and PVA polymers using three different methods i.e melt-mixing, ion-implantation and electrospinning. Meanwhile, there were various samples characterization tests were done such as X-ray attenuation measurement, density measurement and morphology studies in order to characterize the properties of the prepared samples so that they were applicable and suitable to be the X-ray shielding material candidate.

2.1 Lead Oxide–Epoxy Composites

2.1.1 Samples Preparation

Micron-sized of PbO and Pb_3O_4 powder (Chem Supply, Gillman, South Australia, product number LL021) were used as the filler to prepare lead oxide–epoxy composite samples. Initially, the filler powder was added into the FR251 epoxy resin (Bisphenol-Adiglycidyl ether polymer) before the FR251 hardener (isophoronediamine) was mixed into it. The ratio of epoxy resin to hardener used was 2:1. The mixing of filler powder in epoxy resin was done through gentle stirring with a wooden stick within a beaker with constant speed for 10 min to ensure uniform dispersion of the powder in epoxy matrix. The well-mixed mixture was then cast in a 4×6 cm^2 rectangular silicon rubber mold with a thickness of 5 mm and could set overnight at room temperature. The list of samples with different weight percentages of PbO and Pb_3O_4 fillers are shown in Table 2.1.

© Springer Nature Singapore Pte Ltd. 2020

I. M. Low and N. Z. Noor Azman, *Polymer Composites and Nanocomposites for X-Rays Shielding*, Composites Science and Technology,
https://doi.org/10.1007/978-981-13-9810-0_2

Table 2.1 List of composites prepared with different weight fractions of filler and epoxy system and corresponding designations used in this study

Composite by weight fraction (wt%)			Composite designation
Filler		Epoxy system	
PbO	10	90	A1
	30	70	A2
	50	50	A3
	70	30	A4
Pb_3O_4	10	90	B1
	30	70	B2
	50	50	B3
	70	30	B4

2.1.2 Density Measurements

The apparent density ρ of prepared samples was measured using the Archimedes method and calculated using Eq. (2.1) [1]. A calibrated single pan electrical balance, ethanol, and toluene were used for this purpose.

$$\rho = \frac{m_1}{m_2 - m_3}(\rho_l) \tag{2.1}$$

where m_1, m_2 and m_3 are the mass of the sample weighted on the balance, the mass of the sample hanging on balance arm in the air and the mass of the sample hanging on the balance arm immersed in ethanol respectively while ρ_l is the density of the immersion liquid (ethanol and toluene).

The measured densities were compared with the theoretical values, ρ_c (with an assumption that the samples were free from voids) which are determined according to Eq. (2.2) [2]:

$$\rho_c = \frac{100}{\left[\frac{F}{\rho_f} + \frac{E}{\rho_e}\right]} \tag{2.2}$$

where F is the wt% of the filler, E is the wt% of epoxy, ρ_f is the density of filler, ρ_e is the density of epoxy system.

2.1.3 Measurement of X-Ray Mass Attenuation Coefficients (μ_m)

To determine the initial dose (Do), the generated X-rays were directly exposed to the DIADOS diagnostic detector connected to DIADOS diagnostic dosemeter (PTW-Freiburg, Germany) without having passed though any sample. The distance between the X-ray tube and the detector was set to 100 cm, and the X-ray beam was well collimated according to the size of the sample. This experiment was done using a calibrated X-ray machine in Royal Perth Hospital, Western Australia. The final dose (D) was taken with the sample placed on the detector. The exposure was set at 10 mA s, where the X-ray tube voltage was started at 40 kVp with 10 kVp increment up to 100 kVp. Next, the linear attenuation coefficient (μ) for each sample was determined by Eq. (2.3), where x is the thickness of the sample. This μ is divided by the calculated ρ_{comp} according to Archimedes' method [1] to determine μ_m (Eq. 2.4).

$$\mu = \frac{\left(\ln \frac{D_o}{D}\right)}{x} \tag{2.3}$$

The observed results of lm were compared with the theoretical values evaluated from Hubbell's database, NIST XCOM.

$$\mu_m = \frac{\mu}{\rho_{comp}} \tag{2.4}$$

2.1.4 Powder Diffraction

Powder diffraction measurements were performed at the Australian Synchrotron in Melbourne to identify the crystalline phases present in the samples. This work was conducted on the Powder Diffraction beamline, and the diffraction patterns were recorded in the 2θ range of 10–60° at a fixed wavelength of 1.37 Å.

2.1.5 Optical Microscopy

Optical microscopy was done using Nikon ME600 optical microscope. The samples were polished using diamond pastes from 15 to 1.0 lm to obtain mirror-like surface finish.

Table 2.2 List of prepared samples with different weight fractions of filler (WO_3) and epoxy resin

Composite by volume fraction (vol%)	
Filler (WO_3)	Epoxy resin
5	95
10	90
20	80
30	70
35	65

2.1.6 Scanning Electron Microscopy (SEM)

The surface of the samples was also examined using a Zeiss Evo 40XVP scanning electron microscope. Samples were Pt-coated to prevent any charging on the samples during the imaging process. The backscattered electron technique was chosen to gain better contrast because of different atomic number between epoxy and lead. A pure epoxy sample was also examined as a control.

2.2 Tungsten Oxide—Epoxy Composites

2.2.1 Samples Preparation

Nano-sized (<100 nm) and micro-sized (~20 μm) tungsten oxide (WO_3) were used as filler for synthesizing WO_3-epoxy composites. The former was obtained from Sigma-Aldrich and the latter (FR251) from Fibreglass and Resin Sales.

To prepare WO_3-epoxy composite samples, WO_3 powder was added into the FR251 epoxy resin (Bisphenol-A diglycidyl ether polymer) before the FR251 hardener (Isophoronediamine) was mixed into it. The ratio of epoxy resin to hardener used was 2:1. The mixing of WO_3 powder in epoxy resin was done through gentle stirring using a stirring machine at constant speed for 15 min to ensure uniform dispersion of the powder in epoxy matrix. The well-mixed mixture was then cast in a 4 cm × 6 cm rectangular silicon rubber mould with a thickness of 7 mm and could set overnight at room temperature. The list of prepared samples with different weight percentages of WO_3 are shown in Table 2.2.

2.2.2 Measurement of X-Ray Mass Attenuation Coefficient (μ_m)

This work was done using two different sets of equipment. For the lower X-ray energy range, a mammography unit (brand: Siemens AG, model: 2403951-4 G.E

Health Care) was used while a general diagnostic X-ray machine (brand: Shimadzu, model: Circlex 0.6/1.2 P364DK-100SF) was used for the higher X-ray energy range. The initial X-ray intensity (I_o) was determined by directly measuring X-rays with the DIADOS diagnostic detector connected to DIADOS diagnostic dosimeter (PTW-Freiburg, Germany) in the absence of the sample. The dosimeter is a universal dosimeter for measuring simultaneous dose and dose rate for radiography, fluoroscopy, mammography, dental X-ray and CT with a sensitivity of 0.01 microRoentgen (μR). Meanwhile the transmitted X-ray intensity (I) was taken with the sample placed on the detector. The distance between the X-rays' tube and the detector was set to 86 cm since this is the maximum distance that can be adjusted for the mammography unit, and the X-ray beam was well collimated to the size of the sample.

The exposure was set at 10 mAs to obtain meaningful readings for this type of detector. The range 22–49 kV of X-ray tube voltage was selected from mammography unit since the machine can go only within this range for lower X-ray energy. On the other hand, the range of X-ray tube voltage (40–120 kV) was chosen from the general diagnostic X-ray machine because this range is the normal range of X-ray tube voltage used in general diagnostic imaging purposes. The transmitted X-ray beam intensity (I) for each sample at each X-ray tube voltage was determined directly from the dosimeter reading. For each composite, the measurements were performed three times to obtain an average value. The performance of micro-sized and nano-sized WO_3-epoxy composite was compared from the graph of I as a function of filler loading for each X-ray tube voltage.

2.3 Ion-Implanted Epoxy

2.3.1 Samples Preparation

Pure epoxy samples were prepared by mixing one part of FR251 hardener (Isophoronediamine) with two parts of FR251 epoxy resin (Bisphenol-A diglycidyl ether polymer). The mixing of epoxy resin and hardener was done through gentle stirring using a stirring machine (2 level of speed) within a beaker with constant level 1 speed for 10 min to ensure the uniformity of the mixture. Then, the mixture was cast in cylindrical Fixiform moulds (diameter of 25 mm) with a thickness of 2 mm and allowed to set overnight. The cured epoxy samples were polished using diamond pastes from 15 to 1.0 lm to obtain flat and mirror-like surface finishes.

2.3.2 Ion-Implantation

For this preliminary investigation of the X-ray attenuation characteristics of ion-implanted composites, we started with lower implanted dose in order to prevent

possible melting and/or decomposition of the epoxy samples during ion implantation. Polished epoxy samples were implanted with tungsten (W), gold (Au) and lead (Pb), produced by a metal evaporation and direct extraction ion source. For this type of ion source, the charge distribution of positive ions was measured previously by RBS and they are: $W^{+1} = 1\%$, $W^{+2} = 16\%$, $W^{+3} = 58\%$, $W^{+4} = 25\%$, $Au^{+1} = 12\%$, $Au^{+2} = 78\%$, $Au^{+3} = 9\%$, $Au^{+4} = 1\%$ and $Pb^{+1} = 35\%$, $Pb^{+2} = 64\%$, $Pb^{+3} = 1\%$. These values are close to the theoretical prediction using the Debye–Huckel approximation of non-ideal plasma [3]. The RBS measured values of charge distribution result in an average charge of W + 3.07, Au^{+1}.99 and Pb^{+1}.66. Thus, the ion acceleration of 40 kV used in this work afforded an average implantation energy of W = 122.8 keV, Au = 79.6 keV and Pb = 66.4 keV, and a projected range in epoxy of 80 nm, 59 nm and 54 nm, respectively. The beam size was close to 20 cm^2, and the beam current used in this experiment was around 30 lA. The ion fluence was monitored by converting the ion target current into pulses using a current-to-frequency convertor. In this work all three ions were implanted at nominal doses between 7×10^{14} ions/cm^2 and 1.4×10^{15} ions/cm^2, measured by RBS, after the implantation process, and converted in [at. %] for ease of comparison.

2.3.3 Ion Beam Analysis and Rutherford Backscattering Spectroscopy (RBS)

The near surface composition depth profiling of ion-implanted epoxy samples was characterized by ion beam analysis and RBS using a beam of 1.8 MeV He^{1+} ions beam at the Australian Nuclear Science and Technology Organisation. The information obtained was processed using SIMNRA code [4] which allowed calculation of depth distribution of implanted species and the implanted dose, which was converted in concentration. For these particular samples, a depth resolution of the order of 10 nm was achieved for the implanted heavy element.

2.3.4 Measurement of X-Ray Mass Attenuation Coefficients (μ_m)

This work was done using a general diagnostic X-ray machine (brand: Shimadzu, model: Circlex 0.6/1.2 P364DK-100SF). The initial X-ray dose (D_0) was determined by directly measuring X-rays with the DIADOS diagnostic detector connected to DIADOS diagnostic dosemeter (PTW-Freiburg, Germany) in the absence of the sample. The dosemeter is a universal dosemeter for measuring simultaneous dose and dose rate for radiography, fluoroscopy, mammography, dental X-ray and CT. Meanwhile the exit dose (D) was taken with the sample placed on the detector. The distance between the X-rays tube and the detector was set to 100 cm and the X-ray

beam was well collimated to the size of the sample. The exposure was set at 10 mAs to obtain meaningful reading for this type of detector while the tube voltage was increased from 40 to 100 kV in step of 10 kV for each dose measurement. The range of X-ray tube voltage (40–100 kV) was selected because this diagnostic imaging purposes. The mass attenuation coefficient, ($\mu_m = l/\rho_{comp}$) for each sample was determined from Eqs. (2.3) and (2.4).

2.4 Ion-Implanted Acrylic and Glass

2.4.1 Samples Preparation

Commercial samples of acrylic and glass were used for this work.

2.4.2 Ion-Implantation

As a starting study of X-ray shielding capability on different ion-implanted matrices, the sample matrixes were implanted with tungsten (W) of a nominal dose (7×10^{14} ions/cm^2) and lead (Pb) of the nominal dose (7×10^{14} ions/cm^2) and (1.4×10^{14} ions/cm^2) respectively. These lower nominal doses were chosen as the preface investigation in order to prevent possible melting and/or decomposition of the sample matrix during high energy implantation and then will be converted in [at.%] for ease of comparison. The ions were produced by a metal evaporation and the direct extraction ion source. The charge distribution of positive ions of W and Pb as measured previously by RBS are: $W^{+1} = 1\%$, $W^{+2} = 16\%$, $W^{+3} = 58\%$, $W^{+4} = 25\%$, and $Pb^{+1} = 35\%$, $Pb^{+2} = 64\%$, $Pb^{+3} = 1\%$ which are nearly the same as the theoretical prediction by the Debye–Huckel approximation of non-ideal plasma [3]. The RBS measured values of the charge distribution provided an average charge of $W^{+3.07}$ and $Pb^{+1.66}$. Meanwhile, an average implantation energy of W = 122.8 keV and Pb = 66.4 keV was afforded with the ion acceleration of 40 kV used in this study. The beam size was close to 20 cm^2, and the beam current used in this experiment was around 30 μA. The ion fluence was monitored by converting the ion target current into pulses using a current-to-frequency convertor.

2.4.3 Ion Beam Analysis and Rutherford Backscattering Spectroscopy (RBS)

Characterization of the near surface composition depth profiling of all ion-implanted samples was performed using an ion beam analysis and RBS with a beam of 1.8 MeV

He^{1+} ions beam at the Australian Nuclear Science and Technology Organization. Next, the information gathered was processed with SIMNRA code [4] to get the calculation of the depth distribution of implanted species and then was converted in concentration [at.%]. These results were compared with the previous results on ion-implanted epoxy samples [5].

2.4.4 Measurement of X-Ray Linear Attenuation Coefficients (μ_m)

A general diagnostic X-ray machine (Make: Shimadzu, Model: Circlex 0.6/1.2 P364DK-100SF), a DIADOS diagnostic detector and a DIADOS diagnostic dosimeter (PTW-Freiburg, Germany) were used to study the X-ray shielding capability of these implanted sample matrixes. The DIADOS dosimeter is a universal dosimeter for measuring simultaneous dose and dose rate for radiography, fluoroscopy, mammography, dental X-ray and CT. The incident X-ray dose was measured by placing the detector directly below the X-ray tube at a distance of 100 cm. The exit dose (D) was measured by placing the sample on the detector. The X-ray beam was well collimated to the size of the sample and the exposure was set at 10 mAs to receive significant readings for this type of detector. The range of X-ray tube voltage (40–100 kV) was selected for this investigation since this range is the normal range of X-ray tube voltage used in the general diagnostic imaging purposes. The linear attenuation coefficient, μ (unit: cm^{-1}) for each sample was determined from Eq. (2.3).

2.5 Electrospun Bismuth Oxide/Poly-lactic Acid Nanofibre-Mats

2.5.1 Materials

Bismuth (III) oxide (Bi_2O_3) particles of sizes 90–210 nm and 10 μm were used as filler for synthesizing electrospun Bi_2O_3/poly lactic acid (PLA) nanofibre mats and Bi_2O_3/PLA thin films. Bi_2O_3, chloroform and methanol were obtained from Sigma-Aldrich. Meanwhile, PLA (3051D) pellets with the molecular weight Mn = 93.500 g mol and glass transition temperature T_g = 65.50 °C were supplied by NatureWorks USA.

Table 2.3 Prepared electrospun Bi_2O_3/PLA nanofibre mats with different weight fractions (wt%) of filler (Bi_2O_3) and PLA

Filler (Bi_2O_3) (wt%)	PLA (wt%)
24	76
28	72
34	66
38	62

2.5.2 Samples Preparation

Electrospinning was carried out using 9% wt/v PLA solution by mixing with 8 mL of chloroform and 2 mL methanol as the solvents. The micro(m)-Bi_2O_3 and nano(n)-Bi_2O_3 suspension was added at 24–38 wt% to the polymer solution and was homogenized for 45 min under ultrasonication. For electrospinning process, the solutions were transferred to a 10-mL syringe pump with 25-G needles. The flow rate of polymer solution was 1 mL/h, and the applied positive voltage used was in the range of 18–20 kV. The distance between the needle tip and the target was set at 12 cm. The resulting nanofibre mats were collected on a flat aluminium foil for about 2 h to get an acceptable thickness for X-ray transmission experiment. The nanofibre mat was removed from the aluminium foil and was cut to a dimension of 2.0×1.5 cm^2 or was folded together before cutting so that the nanofibre mat has an acceptable thickness for a reliable X-ray transmission experiment. Three sets of the same nanofibre mats were prepared. The list of prepared electrospun Bi_2O_3/PLA nanofibre mats with different weight percentages of Bi_2O_3 are shown in Table 2.3.

The solution casting method was performed to prepare Bi_2O_3/PLA thin films for verifying the X-ray transmission results obtained for electrospun Bi_2O_3/PLA fibre mats. In this method, PLA was mixed with the chloroform without methanol (since methanol was only used in the electrospinning process to increase the conduction of the solution and will totally evaporate during the process) of the same amount as in the electrospinning process and was homogenized for 45 min under ultrasonication. Then, the solution was poured into a beaker of 5 cm diameter and left in the fume cupboard for 24 h to dry. Next, the thin film was removed from the beaker and three sets of the same thin film were cut to pieces of 2.0×1.5 cm^2 for X-ray transmission experiments. The list of prepared Bi_2O_3/PLA thin films with different weight percentages of Bi_2O_3 are the same as shown in Table 2.3.

2.5.3 Measurements of Sample Thickness and Porosity

Since it is difficult to produce all the electrospun Bi_2O_3/PLA fibre mats to have a constant thickness which is an important factor in X-ray transmission comparison, the average thickness of nanofibre mat was measured by weighing and carefully

determining the area of the nanofibre mat. The average thickness (t_{ave}) of the nanofibre mat was determined from Eq. (2.5) where m is the mass, A is the surface area; and ρ is the apparent density of the electrospun Bi_2O_3/PLA nanofibre mat.

$$t_{ave} = \frac{m}{A\rho} \tag{2.5}$$

The apparent density (ρ) of the electrospun Bi_2O_3/PLA fibre mat was accurately measured using the density bottle method (ASTM D854). An average of three measurements was taken for each electrospun Bi_2O_3/PLA fibre mat. The porosity of the electrospun nanofibre mat was calculated by using the following Eq. (2.6). A calibrated single pan electrical balance and distilled water were used for this purpose.

$$Porosity(\%) = \left(1 - \frac{\rho}{\rho_{theory}}\right) \tag{2.6}$$

where, ρ_{theory} is the bulk density of the Bi_2O_3/PLA composite.

The average thickness t_{ave} of individual (2.0×1.5 cm^2) thin films was measured using vernier caliper. Meanwhile, the apparent density (ρ) of thin films was measured using Eq. (2.7) where m is the weighted sample's mass and A is the surface area of Bi_2O_3/PLA thin film.

$$\rho = \frac{m}{t_{ave} \times A} \tag{2.7}$$

2.5.4 Measurement of X-Ray Transmission

Two separate instruments were used to characterize the X-ray transmission of prepared samples. The first involved the use of X-ray absorption Spectroscopy (XAS) beamline at the Australian Synchrotron. Experiments were carried out in the energy range of 7–20 keV using a Si (311) monochromator and a beam size on the sample of about 0.25 by 0.25 mm^2 and a photon flux of about 10^{11} ph/s. Transmission data were collected in an ionization chamber after the sample, and compared to the incident beam flux. For each sample 20 readings were recorded at each energy. To normalize the data collected readings were also recorded for an empty sample holder.

The second instrument used was a mammography unit (brand: Siemens AG, model: 2403951-4 G.E Health Care) at Royal Perth Hospital, Western Australia. For the work with this mammography unit, the exposure was set at 10 mAs to obtain meaningful readings for DIADOS diagnostic detector connected to the DIADOS diagnostic dosimeter (PTW-Freiburg, Germany) and the range 22–49 kV of X-ray tube voltage was selected. The dosimeter is a universal dosimeter for measuring

Table 2.4 Anode/filter combination operated by the mammography machine

X-ray tube voltage (kV)	Anode/filter combination
22	Mo/Mo[a]
25	
30	
35	Mo/Rh[b]
40	
45	Rh/Rh[c]
49	

[a]Molybdenum anode/molybdenum filter. [b]Molybdenum anode/rhodium filter. [c]Rhodium anode/rhodium filter

simultaneous dose and dose rate for radiography, fluoroscopy, mammography, dental X-ray and CT with a sensitivity of 0.01 microRoentgen (μR). Three different anode/filter combinations (Table 2.4) were used for filtering the X-ray beam produced by the chosen X-ray tube voltages used for the mammography machine, since the combination was controlled by the machine itself. The X-ray beams generated by these anode/filter combinations composed mainly of the characteristic X-ray energies of molybdenum (17.5 and 19.6 keV) or rhodium (20.2 and 22.7 keV). For each sample, the measurements were performed three times. The detector was placed 86 cm under the X-ray tube since this is the maximum distance that can be adjusted for the mammography unit, and the X-ray beam was well collimated to the size of the sample size to minimize the scattered X-ray produced by the sample.

An average value for the incident intensity I_o (determined by directly measuring X-rays passed through the detector in the absence of the sample) and transmitted intensity I (determined by a sample placed in front of the detector) were calculated and a graph of the X-ray transmission ($T = I/I_o$) as a function of wt% was plotted for each of the X-ray tube voltage chosen with (T) was related to Eq. (2.8).

$$T = \left(\frac{I}{I_o}\right) = \mathrm{e}^{-\mu t_{ave}} \tag{2.8}$$

2.5.5 Scanning Electron Microscopy (SEM)

The depth profile of the samples was examined using Zeiss Evo 40XVP scanning electron microscope at the voltage of 15 kV with the working distance between 8.0 and 9.0 mm. Both secondary electrons (SE) and backscattered electron (BSE) techniques coupled with an energy dispersive X-ray spectroscopy (EDS) were done after standard coating with platinum to minimize charging to show the different of the image due to the different atomic number of PLA and bismuth. A pure electrospun PLA nanofibre mat was also examined as a benchmark.

Table 2.5 Compositions of WO_3-epoxy composites with different volume fractions of filler WO_3 and epoxy resin

Composite by volume fraction (vol%)	
Filler (WO_3)	Epoxy resin
2	98
4	96
6	94
8	92
10	90

2.6 Micro-sized and Nano-sized Tungsten Oxide-Epoxy Composites

2.6.1 Samples Preparation

Nano-sized (<100 nm) tungsten oxide and micro-sized (~20 μm) tungsten oxide (WO_3) were used as the filler for synthesising WO_3-epoxy composites. The former was obtained from Sigma-Aldrich and the latter (FR251) from Fibreglass and Resin Sales. The particle sizes were provided by Sigma-Aldrich.

Details about the preparation of the WO_3-epoxy composite samples are available in [6]. For the current work, the thickness of the samples was set at 2.0 mm. The list of the prepared samples with the different volume percentages of WO_3 is shown in Table 2.5.

2.6.2 Measurements of X-Ray Transmission

This work was done using the X-ray Absorption Spectroscopy (XAS) beamline at the Australian Synchrotron located in Melbourne. Experiments were carried out in the energy range of 10–40 keV using an Si (311) monochromator and a beam size on the sample of about 0.25 × 0.25 mm^2 and a photon flux of about 10^{11} ph/s. Data on X-ray transmission (I/I_o) were collected in an ionisation chamber after the sample, and compared to the incident beam flux. For each sample, 20 readings were recorded at each energy level. To normalise the data collected, readings were also recorded for an empty sample holder. The average I/I_o was calculated and plotted as a function of filler loadings (WO_3 vol%) for each synchrotron radiation energy. The X-ray transmission (I/I_o) was related to the linear attenuation coefficient (μ) and the thickness of the samples (t) through Eq. (2.8).

Next, all the samples were examined again with a mammography unit and a radiology unit according to previous experiments [6].

2.6.3 Powder Diffraction

Powder diffraction (PD) measurements were conducted to identify the crystallite size of the WO_3. This was done at the Australian Synchrotron in Melbourne, on the Powder Diffraction beamline. Mythen detectors were used to record the diffraction patterns in the 2θ range of 0°–60° at a fixed wavelength of 1.13 Å. The crystallite size (L) of the nano sized WO_3 was determined using the Scherrer equation as follows (Eq. 2.9):

$$L = \frac{k\lambda}{(FWHM)\cos\theta} \tag{2.9}$$

where k is a constant depending upon the crystal shape and size ($k = 0.90$), λ is the wavelength, FWHM is the full-width half maximum of the peak and 2θ is the diffraction angle of the strongest peak.

2.6.4 Flexural Tests

Three-point bending tests were used to determine the flexural strength and modulus of the WO_3-epoxy composites containing different loadings of nano-sized and micro-sized WO_3. Specimens with dimensions 60 mm × 10 mm × 2 mm were prepared for the test according to the ASTM D790-03 standard [7] on a universal testing machine (LLOYD Instruments). A minimum of three samples was tested for each composite and the average results were taken. In these measurements, the samples were tested to the applied load with the results calculated by the NEXYGEN Plus software.

2.6.5 Indentation Hardness Test

The hardness values of polished WO_3-epoxy composites were determined using a Rockwell hardness tester with scale H. The hardness measurements were conducted using an indentation load of 588.4 N and ball diameter of 0.3 cm. Five measurements were conducted for each sample in order to obtain an average value.

2.7 Starch Filled Bi_2O_3–PVA Composites

2.7.1 Materials

Bismuth (III) oxide, Bi_2O_3, with a density of 8.9 g/cm^3, (10–100 nm, Sigma-Aldrich) and (20 lm, Alfa Aesar), polyvinyl alcohol, PVA [molecular weight: 89,000–98,000; hydrolysis rate: 99? %; density: 1.3 g/cm^3 (Sigma-Aldrich)], and starch (potato starch, Sigma-Aldrich) were used in the present study.

2.7.2 Samples Preparation

PVA powder was dissolved in double distilled water at 90 °C and stirred for 6 h in order to ensure that the powders dispersed uniformly. The micro-sized and the nanosized Bi_2O_3–PVA composites were added with different weight percentages (wt%), as depicted in Table 2.6.

The PVA solution was prepared by mixing the PVA powder with distilled water in a beaker. Then, Bi_2O_3 powder was added and heated at a constant temperature (90–100 °C). The solution was stirred at a constant speed for 6 h in order to ensure that the powders dispersed uniformly. The micro-sized and the nano-sized Bi_2O_3–PVA composites were prepared with different weight percentages (wt%), as depicted in Table 2.6. The steps were repeated with the addition of different amounts of starch, as listed in Table 2.7. For the initial investigation, the addition of starch into the composite was prepared only for the Bi_2O_3 filler with wt% of 8, 12, and 15. This procedure was performed to gain better dispersion of both micro-sized and nano-sized Bi_2O_3 particles within the PVA matrix, as well as to assist in enhancing the effect of Bi_2O_3 particle sizes on the X-ray transmission readings. This preliminary approach was done due to the supporting evidence provided by Hejri et al. [8], who claimed that uniform dispersion of TiO_2 nanoparticles was found within the

Table 2.6 Weight percentage of Bi_2O_3 and PVA

Element	Weight percentage (wt%)				
Bi_2O_3	8	12	15	18	21
PVA	92	88	85	82	79

Table 2.7 Weight percentage of Bi_2O_3, PVA and starch

Element	Weight percentage (wt%)					
Bi_2O_3	8	8	12	12	15	15
PVA	91	89	87	85	84	82
Starch	1	3	1	3	1	3

starch–PVA matrix. Finally, the mixture was cast in a rectangular glass plate with a dimension of 11.6 cm × 9 5.6 cm. The sample was left to dry for a week in a closed container within a fume cupboard. After drying, the polymer composite was peeled off from the casting plate, stored, and ready for transmission measurement. The average thickness of the polymer composite was found to be about 0.25 mm.

2.7.3 Density Measurements

The density, ρ, of the samples was determined by using the Archimedes principle with ethanol as the immersion medium, based on the relation provided in Eq. (2.1).

2.7.4 Measurement of X-Ray Transmission

The X-ray transmission was performed by using two modalities, i.e., X-ray fluorescence spectroscopy (XRF) and mammography units (brand: Philips, model: MammoDiagnost AR). In addition, several metal targets, such as niobium, molybdenum, palladium, silver, and tin, were used to measure the X-ray transmission by the samples via XRF unit. These metal targets produced the characteristic of X-ray with energy values of 16.59, 17.46, 21.21, 22.20, and 25.2 keV, respectively. Meanwhile, the mammography unit was used to measure the energy of the X-ray photons produced by tube voltages that ranged from 23 to 35 kV. As for the X-ray transmission measurement of the samples by using XRF unit, the composite sample was placed in front of the germanium detector and it was exposed with the selected energy. On the other hand, for the mammography unit, the source to surface (SSD) distance was arranged at 66 cm and the exposure was set at 10 mAs. The X-ray transmission was obtained by measuring the dose received via Raysafe Xi MAM detector system. The dosimeter is well known as a universal dosimeter for measuring simultaneous dose and dose rate for radiography, CT, mammography, and fluoroscopy. Moreover, the X-ray beam was collimated to a dimension of 3 cm × 9.3 cm in order to minimize any scattered radiation. The initial X-ray beam intensity (Io) was obtained by directly measuring the dose received by the detector in the absence of sample. Other than that, the final X-ray beams' intensity (I) was taken by measuring the dose received with the sample placed on the detector. Initial investigations of starch–composite mixture related to Bi_2O_3 particle size and its effect on the X-ray transmissions had been carried out by using the XRF unit.

References

1. Australian Standards 1774.5, Method 5 (1989) The determination of density, porosity and water absorption
2. Harish V, Nagaiah N, Prabhu TN, Varughese KT (2009) Preparation and characterization of lead monoxide filled unsaturated polyester based polymer composites for gamma radiation shielding applications. J Appl Polym Sci 112:1503–1508
3. Anders A (1997) Ion charge state distributions of vacuum arc plasmas: the origin of species. Phys Rev E 55:969–981
4. Mayer M (1999) Proceedings of the 15th international conference on the application of accelerators in research and industry. In: Duggan JL, Morgan IL (eds) American Institute of physics conference proceedings, vol 475, p 541
5. Noor Azman NZ, Siddiqui SA, Ionescu M, Low IM (2012) Synthesis and characterisation of ion-implanted epoxy composites for X-ray shielding. Nucl Instrum Methods Phys Res Sect B 287:120–123
6. Noor Azman NZ, Siddiqui SA, Hart R, Low IM (2013) Applied radiation and isotopes 71, 62–67
7. Annual Book of ASTM Standards vol 08.01, ASTM, 2005
8. Hejri Z, Ahmadpour A, Seifkordi AA, Zebarjad SM (2012) Role of nano-sized TiO_2 on mechanical and thermal behavior of starch/Poly (vinyl alcohol) blend films. Int J Nanosci Nanotechnol 8:215–226

Chapter 3
Microstructural Design of Lead Oxide–Epoxy Composites for Radiation Shielding Purposes

Abstract Composite epoxy samples filled with PbO and Pb_3O_4 were fabricated to investigate the mass attenuation characteristics of the composites to X-rays in the diagnostic imaging energy range. The effect of density on the attenuation ability of the composites for radiation shielding purposes was studied using a calibrated X-ray machine. Characterization of the microstructure properties of the synthesized composites was performed using synchrotron radiation diffraction, optical microscopy, and scanning electron micros-copy. The results indicate that the attenuation ability of the composites increased with an increase in density. The particle size of WO_3 fillers has a negligible effect on the value of mass attenuation coefficient. Microstructural analyses have confirmed the existence of uniform dispersion of fillers within the matrix of epoxy matrix with the average particle size of 1–5 μm for composites with filler loading of ≤30 wt% and 5–15 μm for composites with filler loading of ≥50 wt%.

3.1 Introduction

During the early part of the 20th century, the hazards from ionizing radiation were recognized, and the use of lead and other materials became commonplace for shielding against X-rays [1–3]. Once the dangers of X-rays are considered, lead has become an important material for radiation protection. Since then protection has evolved into an elaborate infrastructure of controls and disciplines specifying how this shield should be deployed [4–6]. Recently, shielding requirements have become more stringent as standards for exposure of personnel and the general public. X-ray technologists practice a principle called as-low-as-reason- ably-achievable dose when dealing with X-rays, so that radiation dose received by personnel and the general public can be as low as possible [3–7].

The shielding for radiation purposes are based on the type and energy of the radiation itself. Gamma and X-rays are the most penetrating radiations as compared to other ionizing radiations. Their interaction depends on the probability of their collision with the atoms of the materials during the interaction. To increase the probability, they will interact the density of the material they are passing through

© Springer Nature Singapore Pte Ltd. 2020

I. M. Low and N. Z. Noor Azman, *Polymer Composites and Nanocomposites for X-Rays Shielding*, Composites Science and Technology,
https://doi.org/10.1007/978-981-13-9810-0_3

needs to be increased which means the materials should have a lot of atoms with an assumption that the materials are free from voids. If dealing with a material having a lot of pores, porosity needs to be considered, because it will affect the interaction of the radiations with the atoms within the material [8].

Lead-glass is one example of the material used as shielding materials for ionizing radiations, but it is heavy, expensive, and very brittle. So, it is not surprising that polymers have made inroads into markets that were in the beginning dominated by glass. Polymers also have a great potential in many important applications that glass could not meet because of their unique properties, such as a low density, ability to form intricate shapes, optical transparency, low manufacturing cost, and toughness. However, the use of polymers is still limited, because of their inherent softness and low thermal stability [9, 10]. One modern example of the filler-reinforced polymer used for radiation shielding is lead-acrylic [11, 12]. Moreover, many researchers tried to create new lead-based composites for this radiation shielding purposes such as lead-polyester composites [13], lead-styrene butadiene rubber [14], lead-polystyrene [15], and similar materials.

Rudraswamy et al. [16] have shown that some lead compounds such as PbO, PbO_2, $PbNO_3$, and $PbCl_2$ have an adequate mass attenuation coefficient, lm for use in radiation shielding purposes. Unfortunately, the usage of either lead or lead compounds alone will cause certain health risks to human, animals, and to the surroundings [17]. Moreover, lead or lead compounds themselves are also not malleable and lack in mechanical strength [18].

Additionally, there are many methods available to achieve a good dispersion of fillers within a polymeric matrix. One of the traditional methods for dispersing fillers in polymer matrices is melt-mixing method of the fillers into the polymer. The fillers are weighted and added straightly into the polymer for mixing. In many works done, many researchers used a static mixer with constant speed during the mixing process to achieve homogenously dispersion of fillers within the polymers [13, 19]. It is expected that lead oxide–epoxy composites will be a good material to be used as radiation shielding in diagnostic radiology purposes. This is because lead oxide can be easily dispersed within a polymer matrix [13]. Besides, an epoxy system is a thermoset material that is generally stronger and better suited to higher temperatures than thermoplastics, so it can withstand the high energetic X-rays bombardment during the diagnostic imaging [20]. Hence, the purpose of this study is to prepare and characterize a composite that is made of an epoxy system filled with lead oxides. The feasibility of this material for use in X-ray shielding is discussed.

3.2 Results and Discussion

3.2.1 Density of Samples

As can be seen from Table 3.1, the values of apparent density for samples obtained

Table 3.1 Comparison of measured and theoretical density values for the composites

Composite designation	Density of composite, ρ_{comp} (g/cm^3)	
	Theoretical	Measured
A1	1.26	1.26 ± 0.01
A2	1.56	1.53 ± 0.01
A3	2.06	2.05 ± 0.02
A4	3.00	2.93 ± 0.03
B1	1.26	1.26 ± 0.01
B2	1.55	1.55 ± 0.01
B3	2.02	2.00 ± 0.03
B4	2.90	2.83 ± 0.03

from the Archimedes' technique did not totally agreed with the theoretical values because of experimental uncertainties. The porosity calculated for each sample was less than 1%. Besides, the higher the wt% of the filler within the composite, the higher the value of qc as also been observed by Harish et al. [13], Berger et al. [21].

3.2.2 X-Ray Mass Attenuation Coefficients

The μ_m values given in NIST are specifically measured for characteristic photon energy, whereas in this experiment; the X-ray tube voltages used are in continuous spectrum. So, the equivalent energies for the X-ray tube voltages used within the experiment must be taken into account for comparing the value of lm between NIST and experiment. The equivalent energies for the X-rays tube voltages used are shown in Table 3.2. These values were calculated using the equation fitted as an exponential function (Eq. 3.1) [22]:

$$y = a_{\exp}^{-\left(\frac{x}{c}\right)} + b \tag{3.1}$$

Table 3.2 Equivalent energy for the various X-ray tube voltages used

X-ray tube voltage (kV_p)	Equivalent energy (keV)
40	29.9
50	34.3
60	38.5
70	42.5
80	46.2
90	49.7
100	52.9

where a, b, and c in the Eq. (3.2) are constants with values of −97.535, 106.857, and 168.672, respectively, whereas y is the equivalent energy and x is the X-ray tube voltage. For composites, the value of μ_m was calculated using Eq. (3.2):

$$\mu_m = \sum w_i \mu_{m_i} \tag{3.2}$$

where μ_m is the mass attenuation coefficient of the composite, whereas w_i and μ_{mi} are the weight fraction and the mass attenuation coefficient of each compound used to make the composite, respectively.

The plots in Fig. 3.1a–c show that almost all the lines for the lm experimental values were a few percent lower than the lm values interpolated from NIST for the given X-ray tube voltages. These results are like the work done by Gerward et al., which they have found that tabulated X-ray mass attenuation coefficients are commonly a few percent higher than the measured values [23, 24]. Icelli et al. [25] obtained very similar results where the higher the density of the material, the higher the value of μ_m. However, the relationship between mass attenuation coefficient (lm) and particle size of lead oxide remains unknown. The use of nanosized lead oxide increase or decrease the value of μ_m? As nanosized lead oxide was not available, the effect of particle size of WO_3 filler (purchased from Sigma–Aldrich, Castle Hill, NSW, Australia) on μ_m was studied. The procedure to prepare this composite was similar to that for preparing PbO–epoxy samples. Figure 3.1d shows the effect of particle size on the mass attenuation coefficient in epoxy composite filled with either microsized (~20 μm) or nanosized (<100 nm) WO_3. It is clearly shown that particle size has a negligible effect on the value of μ_m of a material for this range of X-ray energy 40–100 kVp. However, it should be noted that nanosized particles (e.g., CuO) have been reported to show better X-ray attenuation at the lower X-ray beam energy (i.e., 26–30 kV) [26, 27]. As photoelectric absorption dominates at low photon energies, the probability of an X-ray with low energy to interact and to be absorbed is higher for nanosized particles, in addition to maximization of the surface/volume ratio. However, as photon energy increases, the probability of Compton scattering increases, and hence the attenuation by the material decreases, as this interaction is weakly dependent on atomic number of the element and the photon energy. Hence, the probability of an X-ray with higher energy to interact and to be absorbed becomes similar for both nanosized and microsized particles. It appears that the use of nanosized particles only helps in providing a uniform dispersion within the epoxy matrix but has no direct effect on the value of μ_m as clearly indicated in Eq. (3.2). Only the abundance of WO_3 dispersed in the composite will influence the value of μ_m. The mass attenuation coefficient, μ_m is the rate of photon interactions within 1-unit of mass per 1-unit of area (g/cm^2). It depends on the energy of the photon and the concentration of electrons in the material. Its value will decrease rapidly with the increment of photon energy. Further the chance of a photon coming close enough to an electron is higher when the concentration of electrons within the material is higher, because it is absorbed by the material. Electron concentration was determined by the physical density of the material. Thus, composites with a fine

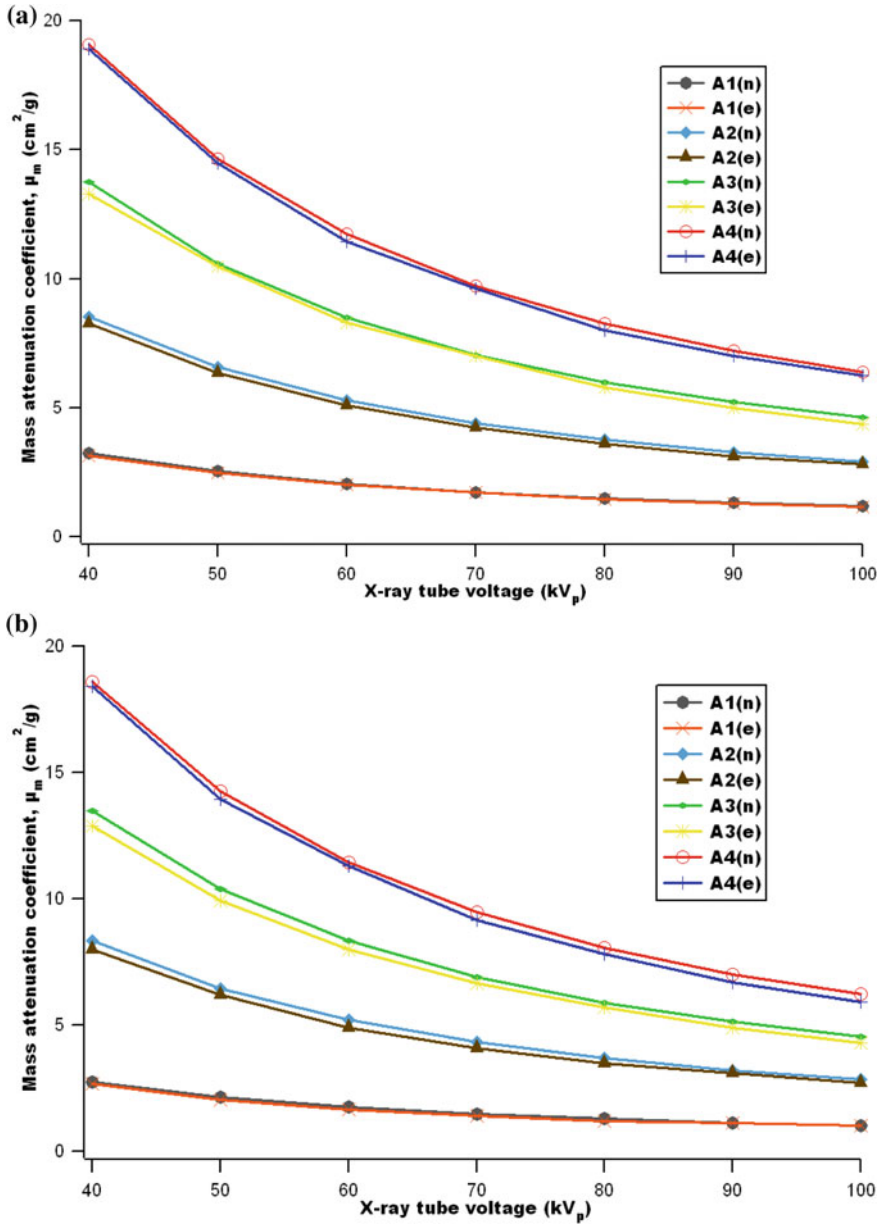

Fig. 3.1 Mass attenuation coefficients as a function of kVp as obtained from NIST (n) and experiment (e) for samples of **a** PbO–epoxy composite, **b** Pb_3O_4–epoxy composite, **c** close-up view of (**a**), and **d** micro-and nano-WO_3 epoxy composites [29]

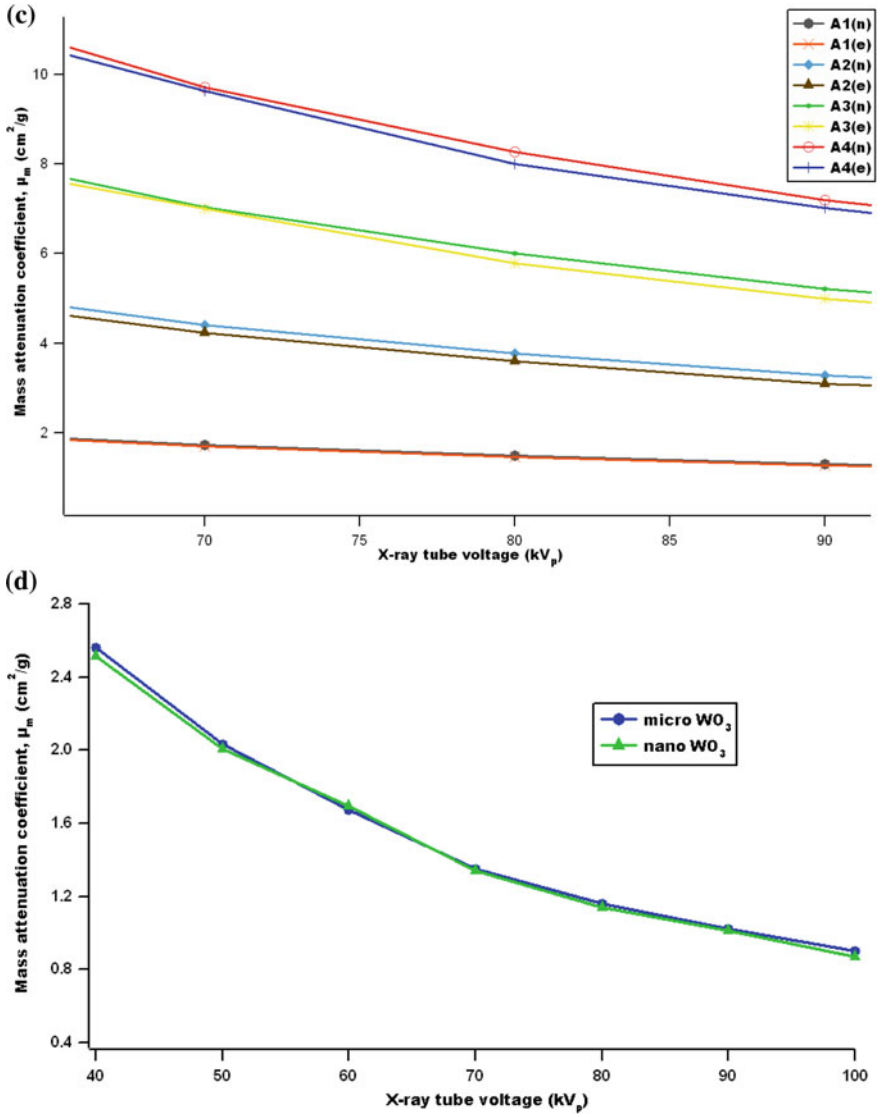

Fig. 3.1 (continued)

dispersion of high-density material provide more interaction probability for photons and also better radiations shielding properties [13, 28]. To ascertain the shielding ability of the composites, calculations of μ_m were done to compare the 50 wt% of PbO reinforced isophthalate resin composite performed by Harish et al. [13] The value of μ_m for their composite was calculated to be 0.0948 cm^2/g, whereas the values of μ_m for samples A3 and B3 in this study, which also have 50 wt% of the

Table 3.3 Mass attenuation coefficients interpolated from NIST databases for gamma rays of energy 0.662 MeV from Cs-137 point source

Composite designation	Mass attenuation coefficient, μ_m (cm^2/g)
A1	0.0871
A2	0.0924
A3	0.0978
A4	0.1055

fillers, were 0.0978 and 0.0974 cm^2/g, respectively. The calculation of μ_m was done by interpolating NIST databases for gamma rays of energy 0.662 MeV from a Cs-137-point source. These results show that samples A3 and B3 in this study provided better radiation shielding than the composite fabricated by Harish and coworkers. Moreover, the usage of lead oxides for radiation shielding can be minimal in the fabrication of composites and thus reduce the health risks associated with lead oxides. The results for other samples at the same energy range are shown in Table 3.3.

3.2.3 Phase Compositions

The reference for phase-fitting the peaks were taken from International Centre for Diffraction Data PDF-4 + 2009 database. The wavelength for all these databases was chosen to be the same as the wavelength of the synchrotron radiation used. From Fig. 3.2a, all the peaks belong to orthorhombic PbO crystal structures (PDF_4 þ files 01-076-1796). While for composite filled with Pb_3O_4 powder, all the peaks were identified as tetragonal Pb_3O_4 crystal structures (PDF-4 + file 04-007-2162) as shown in Fig. 3.2b. These indicate that the powders of PbO and Pb_3O_4 used were single-phase pure.

3.2.4 Microstructures

The typical fracture surfaces for the samples are shown in Fig. 3.3. The scratches seen in the images were due to the polishing process. These images have shown that the fractured surfaces were quite rough, and the fillers (white patches) were well dispersed and firmly embedded in the epoxy matrix due to their relatively small particle size and good compatibility with the epoxy matrix. Although the fillers have a greater weight fraction than epoxy, they were dispersed quite uniformly with only some agglomerations to be found. As can be seen in Fig. 3.3a, the blurry white patches are clear indications of some minor filler agglomerations. The scanning electron microscopy (SEM) images in Fig. 3.4 have provided results that agreed with the optical images shown in Fig. 3.3. The bright regions represent the filler particles (lead-oxide) dispersed in the dark epoxy matrix. The fillers were seen to be

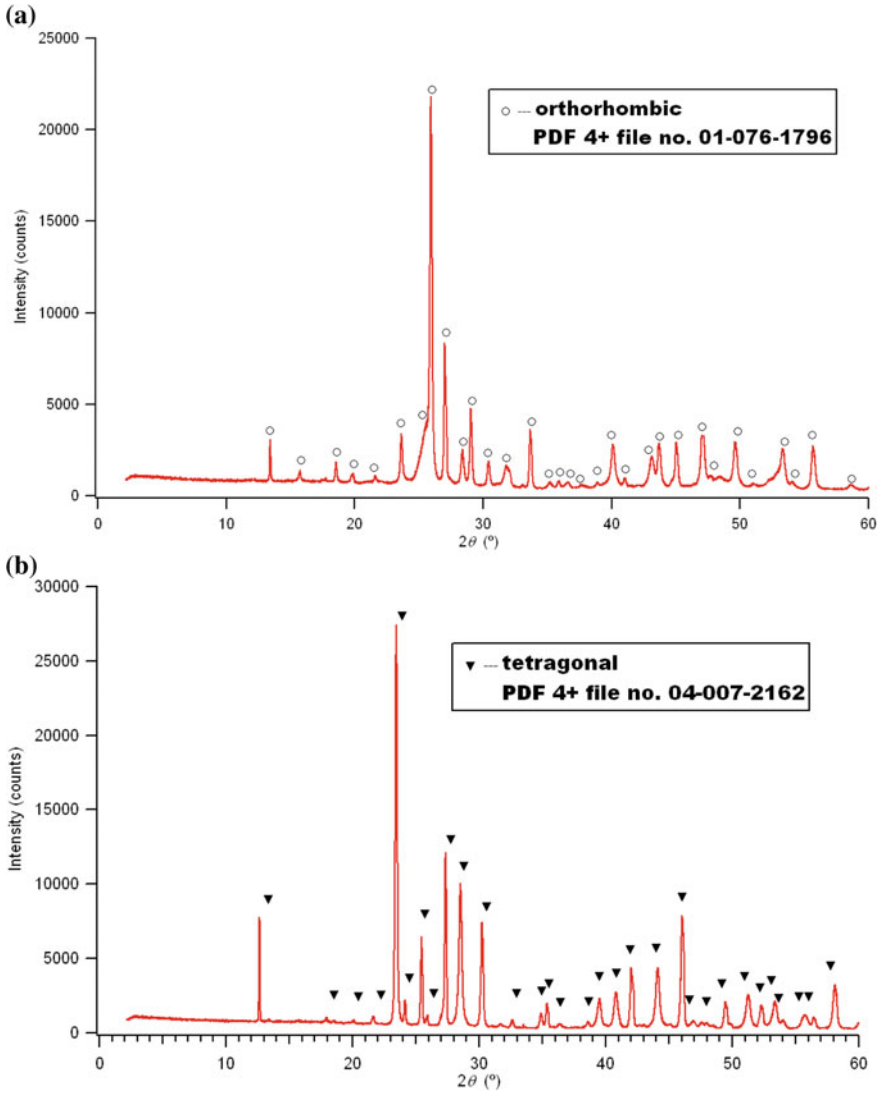

Fig. 3.2 Typical powder diffraction patterns for **a** PbO–epoxy composite and **b** Pb_3O_4–epoxy composite [29]

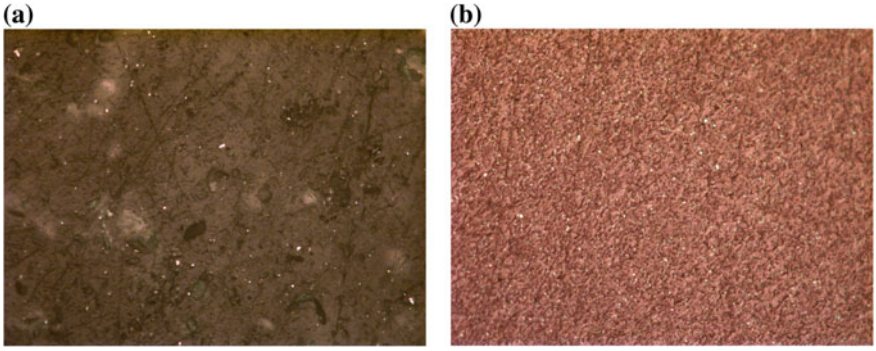

Fig. 3.3 Optical micrographs showing the typical uniform dispersion of fillers in the matrix of epoxy for two composite samples: **a** A3 and **b** B2. 50 × magnification [29]

quite uniformly dispersed in the composites, although minor agglomerations can be observed. The average particle size obtained from the SEM images was ~1–5 μm for composites with filler loading of ≤30 wt% and ~5–15 μm for composites with filler loading of ≥50 wt%.

3.3 Conclusions

Epoxy composites filled with dispersed lead oxide particles of 1–5 μm for composites with filler loading of ≤30 wt% and 5–15 μm for composites with filler loading of ≥50 wt% have been successfully fabricated. These composites showed good X-ray attenuation properties and could be considered as a potential candidate for radiation shielding in diagnostic radiology purposes. The particle size of WO_3 fillers has a negligible effect on the value mass attenuation coefficient (μ_m) for the X-ray energy of 40–100 kVp. In addition, the lead oxide–epoxy composites in this study are superior to the lead oxide-isophthalate resin composite previously investigated.

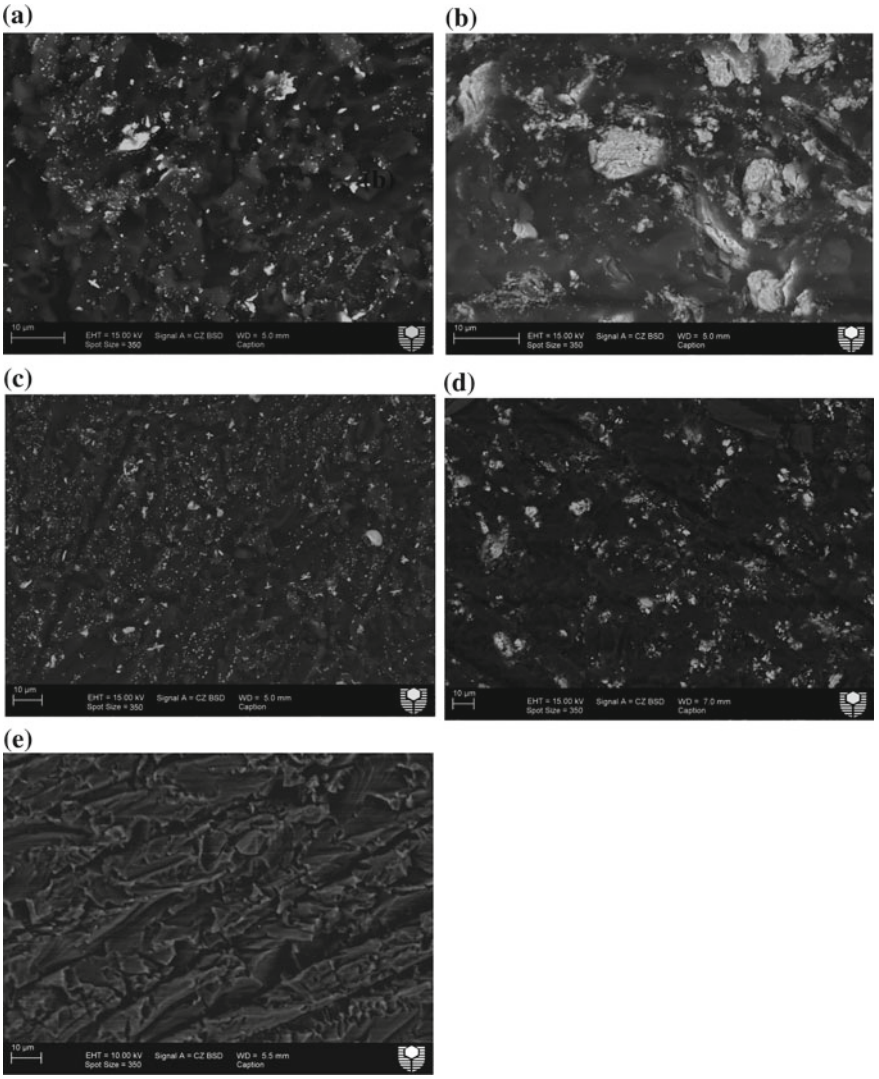

Fig. 3.4 SEM micrographs showing the uniform dispersion of PbO or Pb_3O_4 particles within the epoxy matrix in various composite samples: **a** A3, **b** A4, **c** B2, **d** B3, and **e** pure epoxy [29]

Acknowledgements The funding for the collection of synchrotron powder diffraction data at the Australian Synchrotron in this work was provided by Grant Number AS111/PD3509 and AS111_PDFI3181.

References

1. Archer BR, Thornby JI, Bushong SC (1983) Diagnostic X-ray shielding design based on an empirical model of photon attenuation. Health Phys 44:507
2. Archer BR (1995) History of the shielding of diagnostic X-ray facilities. Health Phys 69:750
3. Archer BR (2005) Recent history of the shielding of medical X-ray imaging facilities. Health Phys 88:579
4. Hessenbruch A (2002) A brief history of x-rays. Endeavour 26:137
5. Okunade AA (2002) Comparison of lead attenuation and lead hardening equivalence of materials used in respect of diagnostic X-ray shielding. Appl Radiat Isot 57:819
6. Okunade AA (2004) Numerical models for the determination of primary structural barriers for diagnostic X-ray facilities. Med Phys 31:513
7. Dixon RL, Simpkin DJ (1998) Primary shielding barriers for diagnostic X-ray facilities: a new model. Health Phys 74:181
8. Lorenzen W (2000) Is Gold better than lead as a radiation shield. MadSci network: engineering
9. Polymer versus Glass, POLYMICRO Newsletter, 2004. Available at: http://www.polymicro-cc.com. Accessed on 24 June 2011
10. Lee EH, Rao GR, Lewis MB, Mansur LK (1993) Ion beam application for improved polymer surface properties. Nucl Instrum Methods Phys Res Sect B: Beam Interact Mater Atoms 74:326
11. Premac Lead Acrylic, Part of the Wardray Premise Total Radiation Shielding Package, Wardray Premise Ltd. Available at: http://wardray-premise.com/structural/materials/premac.html. Accessed on 4 May 2011
12. Radiation Safety & Consumable Products. Available at: http://www.lablogic.com/moreinfo/PDF/consumables/lablogic_consumables_brochure.pdf. Accessed on 4 May 2011
13. Harish V, Nagaiah N, Prabhu TN, Varughese KT (2009) Preparation and characterization of lead monoxide filled unsaturated polyester based polymer composites for gamma radiation shielding applications. J Appl Polym Sci 112:1503
14. Abdel-Aziz MM, Badran AS, Abdel-Hakem AA, Helaly FM, Moustafa AB (1991) Styrene-butadiene rubber/lead oxide composites as gamma radiation shields. J Appl Polym Sci 42:1073
15. Pavlenko VI, Lipkanskii VM, Yastrebinskii PN (2004) Calculations of the passage of gamma-quanta through a polymer radiation-protective composite. J Eng Phys Thermophys 77:11
16. Rudraswamy B, Dhananjaya N, Manjunatha H (2010) Measurement of absorbed dose rate of gamma radiation for lead compounds. Nucl Instrum Methods Phys Res Sect A: Accelerators Spectrometers Detectors Assoc Equip 619:171
17. Robert RD (2005) High density composites replace lead. Ecomass Technologies, Austin
18. Spinks JWT, Wood RJ (1976) An introduction to radiation chemistry. Wiley-Interscience, New York
19. Tanahashi M (2010) Development of fabrication methods of filler/polymer nanocomposites: with focus on simple melt-compounding-based approach without surface modification of nanofillers. Materials 3:1593
20. Material Guide, Archos LLC. Available at: http://www.archosllc.com/Material_Guide_2.html. Accessed on 20 June 2011
21. Berger MJ, Hubbell JH, Seltzer SM, Chang J, Coursey JS, Sukumar R, Zucker DS, Olsen K (2010) XCOM: photon cross section database (version 1.5). National Institute of Standards and Technology, Gaithersburg, MD, 2010. Available at: http://physics.nist.gov/xcom. Accessed on 20 June 2011
22. Mincong C, Hongmei L, Ziyu C, Ji S (2008) An examination of mass thickness measurements with X-ray sources. Appl Radiat Isot 66:1387
23. Gerward L (1992) Theoretical upper and lower limits to experimental X-ray attenuation coefficients. Nucl Inst Methods Phys Res B 69:407
24. Midgley SM (2005) Measurements of X-ray linear attenuation coefficient for low atomic number, materials at energies 32–66 and 140 keV. Radiat Phys Chem 72:525
25. Icelli O, Erzeneoglu S, Boncukc-uoglu R (2004) Experimental studies on measurements of mass attenuation coefficients of boric acid at different concentration. Ann Nucl Energy 31:97

26. Botelho MZ, Ku¨nzel R, Okuno E, Levenhagen RS, Basegio T, Bergmann CP (2011) X-ray transmission through nanostructured and microstructured CuO materials. Appl Radiat Isot 69:527
27. Ku¨nzel R, Okuno E (2012) Effects of the particle sizes and concentrations on the X-ray absorption by CuO compounds. Appl Radiat Isot 70:781
28. Sprawls P (1993) The physical principles of medical imaging. Aspen Publishers, Gaithersburg
29. Noor Azman NZ, Siddiqui SA, Hart R, Low I (2012) Microstructural design of lead oxide-epoxy composites for radiation shielding performances. M J Appl Polym Sci 128:3213

Chapter 4
Synthesis and Characterization of Pb, Bi or W Compound Filled Epoxy Composites for Shielding of Diagnostic X-Rays

Abstract Lead chloride, bismuth oxide and tungsten oxide filled epoxy composites with different weight fractions were fabricated to investigate their X-ray transmission characteristics in the X-ray diagnostic imaging energy range (40–127 kV) by using a conventional laboratory X-ray machine. Characterizations of the microstructure-properties of the synthesized composites were performed using synchrotron radiation diffraction, backscattered electron imaging microscopy, three-point bend test and Rockwell hardness test. As expected, the X-ray transmission was decreased by the increment of the filler loading. Meanwhile, the flexural modulus and hardness of the composites were increased through an increase in filler loading. However, the flexural strength showed a marked decrease with the increment of filler loading ($\geq$30 wt%). Some agglomerations were observed for the composites having $\geq$50 wt% of filler.

4.1 Introduction

X-rays/gamma-rays are the most penetrating of ionizing radiation than is known to be harmful to human health and heredity. Hence there is no doubt that the attenuation of them through composite materials has attracted much attraction amongst the researchers especially for medical studies [1–3]. The most important quantity to characterize the attenuation of photons (X-rays/gamma-rays) within the extended material they pass through is the linear attenuation coefficient (μ) or mass attenuation coefficient (μ/ρ). This quantity is needed in solving various problems such as in radiation dosimetry and radiation shielding application [1, 4, 5].

Lead-glass is one of the materials used for shielding of ionizing radiations, but it is heavy, expensive and very brittle. So, it is not surprising that the application of polymers in X-ray shielding technology is increasing steadily. This is due to several advantages that glass could not meet because of their unique properties, such as low manufacturing cost and rugged shatter-resistant material. In addition, the improved dispersion of fillers within polymer will enable the formation of mechanically stable materials and the possibility to modify both chemical composition and the related physical properties of polymers by easy-to-control fabrication parameters [6–10].

© Springer Nature Singapore Pte Ltd. 2020

I. M. Low and N. Z. Noor Azman, *Polymer Composites and Nanocomposites for X-Rays Shielding*, Composites Science and Technology,
https://doi.org/10.1007/978-981-13-9810-0_4

However, the use of polymers is still limited, because of their inherent softness and low thermal stability [11–13].

Recently, many researchers have tried to synthesize new filler-reinforced polymer composites for radiation shielding and as the replacement for lead glass which is heavy and very fragile [14–17]. The X-ray shielding properties of the filler-reinforced polymer composites generally increase with a good dispersion degree of the filler within the polymer [18]. One modern example of the filler-reinforced polymer used for radiation shielding is lead-acrylic [19, 20]. The lead acrylic of the same size of lead glass with equal lead equivalence, the lead acrylic has nearly twice the weight of lead glass and it is even thicker than lead glass if just looking for the same lead equivalent factor, hence reducing the observation capabilities.

The comprehensive literature survey reveals that the gamma/X-ray shielding characteristics of filler-reinforced epoxy resins have not been attempted. In a recent work on WO_3-filled epoxy composites [21], we investigated only the effect of nano-sized and micro-sized fillers on X-ray attenuation in the energy range of 22–127 kV but the mechanical properties of these composites were not investigated. The results showed that nano sized WO_3 was more effective than micro-sized WO_3 in X-ray attenuation only at the low energy range of 22–35 kV but this size effect was not apparent at the higher energy range of 40–120 kV.

Thus, the aim of this study was to prepare, characterize and compare the physical, mechanical and X-ray transmission properties of epoxy composites filled with Pb, Bi or W compound. The feasibility of these composites for use in X-ray shielding is compared with the commercial lead glass.

4.2 Results and Discussion

4.2.1 Density

From Table 4.1, the apparent density of each sample of the same filler type increased with the increment of filler content, a phenomenon which was also observed by

Table 4.1 Density of filler-epoxy composite samples

% Weight	Density (cm^3/g)					
	$PbCl_2$-epoxy		Bi_2O_3-epoxy		WO_3-epoxy	
	(e)	(t)	(e)	(t)	(e)	(t)
10	1.24 ± 0.02	1.25	1.26 ± 0.01	1.26	1.24 ± 0.03	1.26
30	1.47 ± 0.05	1.52	1.55 ± 0.03	1.56	1.50 ± 0.02	1.54
50	1.85 ± 0.03	1.92	2.00 ± 0.03	2.04	1.87 ± 0.06	1.98
70	2.54 ± 0.06	2.63	2.68 ± 0.07	2.95	2.71 ± 0.03	2.79

(e)—experiment, (t)—theory

Harish et al. [14]. However, the results did not agree very well with the theoretical values, especially when the filler loading was more than 30 wt% due to lack of epoxy to fully cover the surfaces of filler powder, resulting in the concomitant increase in the number of pores and thus reducing the density of the composite. Equation (4.1) was used to compute the relative errors for density measurements relative to the theoretical density values:

$$\delta\rho_s = \left(\frac{\delta m_1}{m_1} + \frac{\delta m_2 + \delta m_3}{m_2 - m_3} + \frac{\delta\rho_e}{\rho_e}\right) \times \rho_s \tag{4.1}$$

where $\delta\rho_s$ is the apparent density uncertainty of the sample, δm_1, δm_2 and δm_3 are the mass uncertainty of the sample weighted in the balance, the sample hanging on the balance arm in the air and the sample hanging on the balance arm immersed in ethanol respectively. $\delta\rho_e$ is the density uncertainty of ethanol calculated from the error of its measured density and its accepted density.

The theoretical density values (ρ_{comp}) were calculated from Eq. (2.2) with an assumption of the samples being void-free.

The computed errors for density values relative to the theoretical density values are in the acceptable limit (i.e. <10.0%).

4.2.2 *Effect of Filler Loading on the X-Ray Transmission (I/I_o) by Epoxy-Based Composites*

The plots in Fig. 4.1a show that for the same filler type and at the same X-ray tube voltage, X-ray transmission value was decreased by the increment of the filler loading. For example (Fig. 4.1b), at 60 kV X-ray tube voltage, X-ray transmission for the 10 wt% of Bi_2O_3-epoxy composite is about 57 times greater than the X-ray transmission value for the 70 wt% of Bi_2O_3-epoxy composite. This was due to the amplification of elemental composition of the composite with the increment of filler loading in the epoxy base which play an important role in absorbing the X-ray passing through them. A similar result in X-ray transmission as a function of filler loading was obtained for epoxy composites filled with $PbCl_2$ and WO_3.

In order to ascertain the shielding ability of the composites, these results were compared with commercial lead glass (thickness: 10 mm) which contained 56 wt% of Pb (information provided by Gammasonics Institute for Medical Research Pty Ltd.) (see Fig. 4.1a). Bi_2O_3-epoxy composite having 70 wt% of Bi_2O_3 gave nearly the same (I/I_o) value as compared to lead glass and other composite samples even though it is thinner than lead glass. Hence the usage of lead in X-ray shielding can be substituted by Bi_2O_3 whereby Bi is classified as least toxic compared to Pb. In addition, even though the 70 wt% WO_3-epoxy composite with 8 mm thickness shows higher (I/I_o) values when compared to lead glass (Fig. 4.1c), WO_3-epoxy composite also can be a substitute material for Pb in X-ray shielding by increasing its thickness

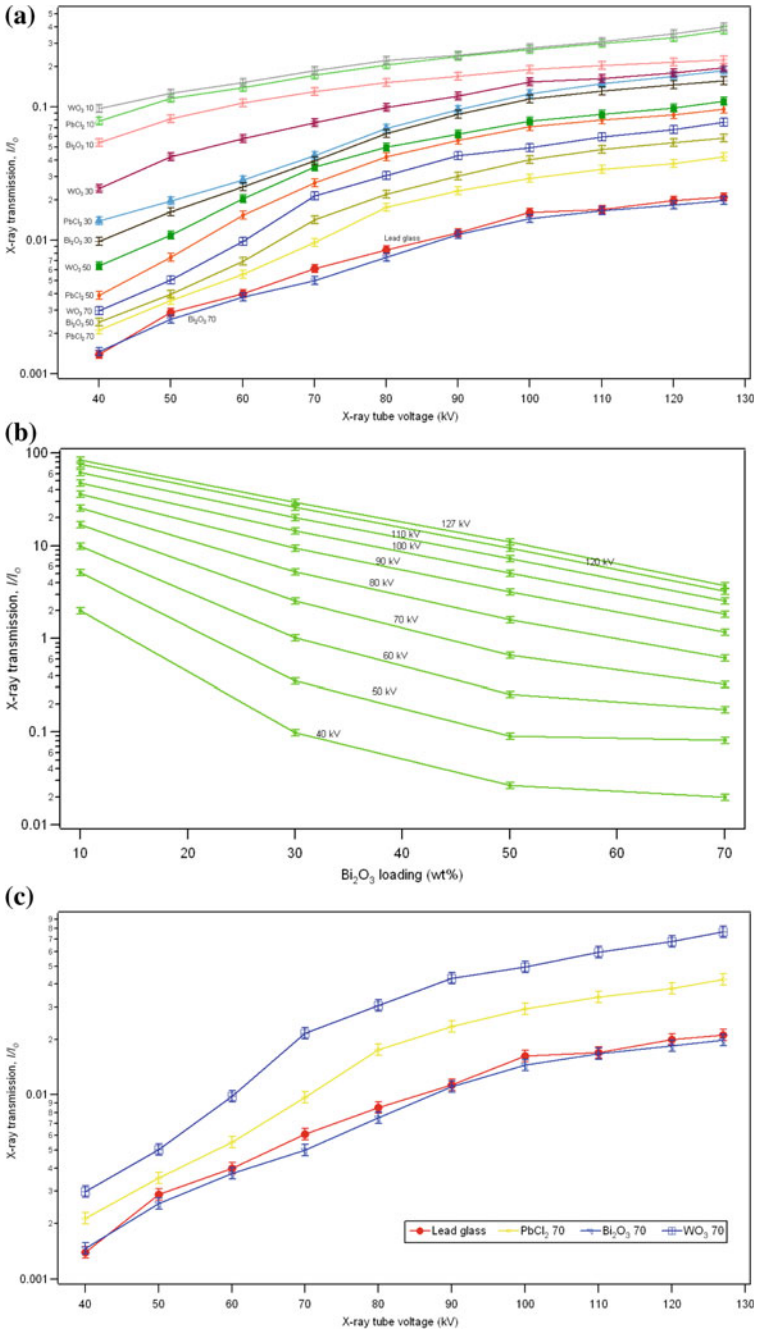

Fig. 4.1 **a** X-ray transmission (I/I_o) as a function of X-ray tube voltage for all composites and commercial lead glass; **b** X-ray transmission (I/I_o) as a function of Bi_2O_3 loading (wt%) showing that (I/I_o) was decreased by the increment of the filler loading; and **c** X-ray transmission (I/I_o) as a function of X-ray tube voltage for epoxy composites filled with 70 wt% of $PbCl_2$, Bi_2O_3 and WO_3 [23]

so that it can provide similar X-ray transmission characteristic as lead glass. The usage of $PbCl_2$-epoxy composite with larger thickness can also be considered as a lighter alternative for lead glass in X-ray shielding.

4.2.3 Phase Compositions

The reference for fitting the peaks was taken from International Centre for Diffraction Data (ICDD) PDF-4 + 2009 database. The wavelength for all of these databases was chosen to be the same as the wavelength of the synchrotron radiation used.

The Powder Diffraction (PD) pattern in Fig. 4.2a shows that all the peaks belong to orthorhombic $PbCl_2$ (PDF files 04-005-4709). For composite filled with Bi_2O_3, all the peaks were identified as monoclinic Bi_2O_3 (PDF file 00-050-1088) as shown in Fig. 4.2b and the diffraction peaks shown in Fig. 4.2c belong to monoclinic WO_3 (PDF file 00-043-1035). These results indicate that $PbCl_2$, Bi_2O_3 and WO_3 were single-phase pure without impurities.

4.2.4 Microstructure Analyses

The surface features of samples in Fig. 4.3, which uses atomic number contrast to differentiate between low and high atomic number elements, show that the fillers appear brighter (higher atomic number) than the surrounding epoxy (low atomic number). The fillers (white patches) are seen to be dispersed uniformly in the epoxy matrix with low filler loading (Fig. 4.3a–c). However, the dispersion of the fillers within the matrix becomes less uniform with the increment of filler loading, resulting in some agglomerations. These filler agglomerations can be seen in composites with $\geq$50 wt% of filler (Fig. 4.3d–g). To minimize the occurence of these agglomerations, higher shear forces through faster stirring are required to achieve a fine dispersion in the polymer matrix. Alternatively, the use of ultrasonication can be used to prevent or minimize filler agglomerations. These methods promote the "peeling off" of individual particles located at the outer part of the particle bundle, or agglomerates, and thus results in the separation of individualized particles from the bundles.

4.2.5 Mechanical Properties

Figure 4.4 shows the effect of filler loading on flexural strength, flexural modulus and Rockwell hardness of epoxy composites. The flexural strength has improved for composite with 10 wt% filler loading. For instance, the flexural strength of epoxy has improved by 48% in the composite with 10 wt% WO_3 loading. However, the addition of more filler ($\geq$30 wt%) caused a marked decrease in flexural strength due

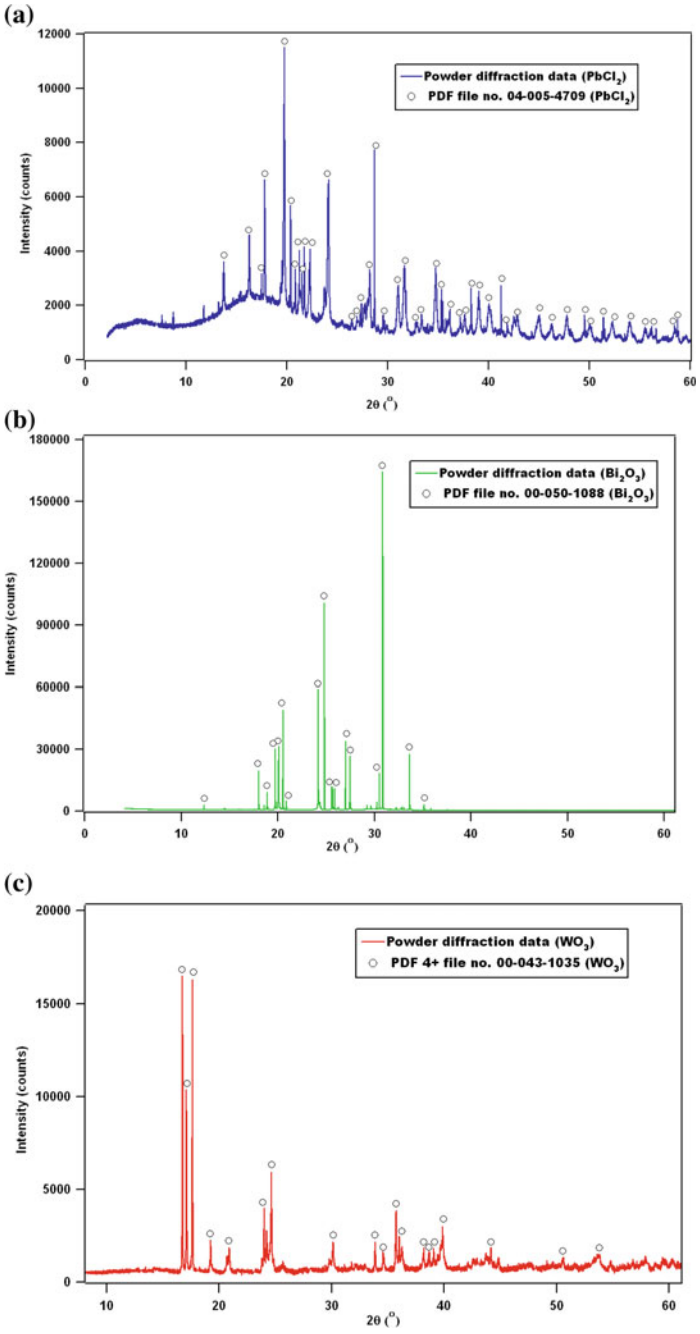

Fig. 4.2 Typical powder diffraction pattern of **a** $PbCl_2$-epoxy composite; **b** Bi_2O_3-epoxy composite and **c** WO_3-epoxy composite [23]

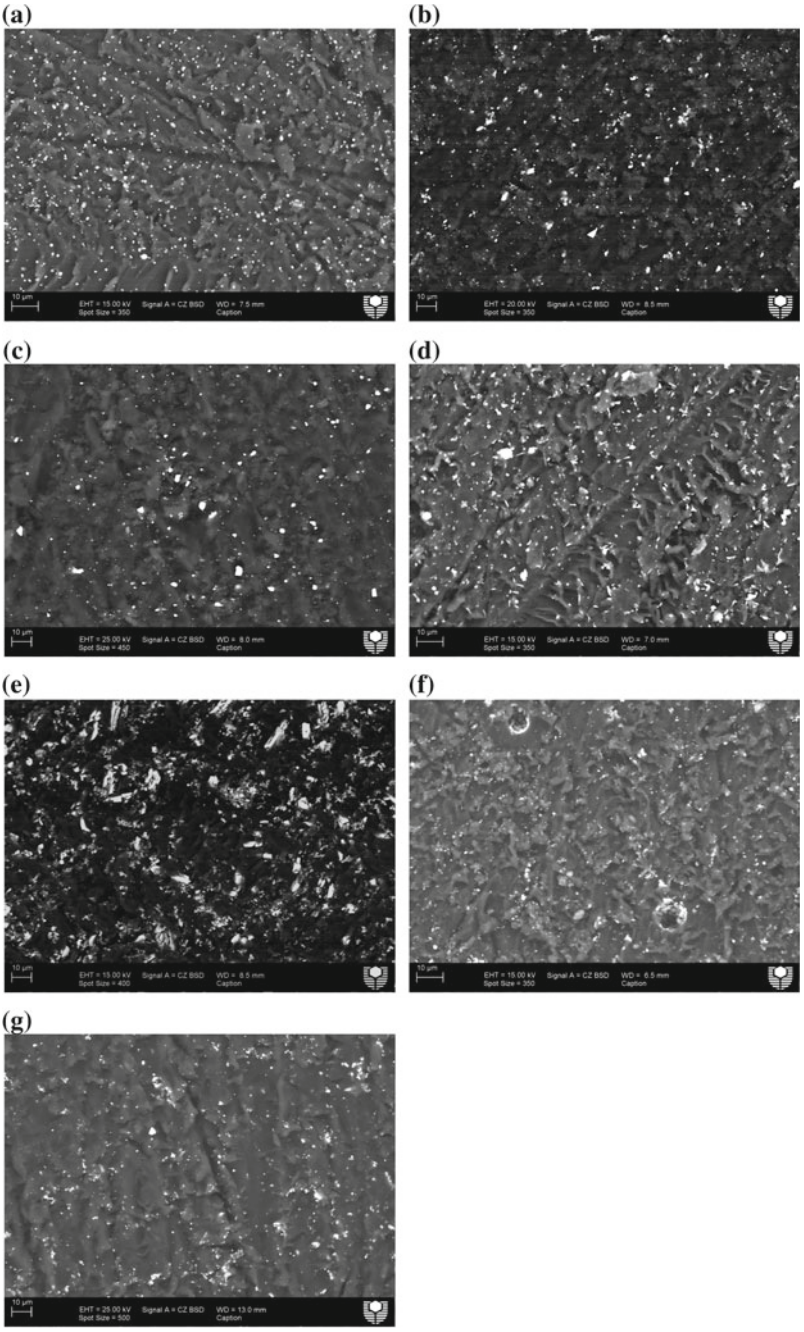

Fig. 4.3 Backscattered electron micrographs showing the dispersion of fillers in epoxy composites containing. **a** 10 wt% $PbCl_2$; **b** 30 wt% Bi_2O_3; **c** 30 wt% WO_3; **d** 50 wt% $PbCl_2$; **e** 50 wt% Bi_2O_3; **f** 70 wt% $PbCl_2$; and **g** 70 wt% WO_3 [23]

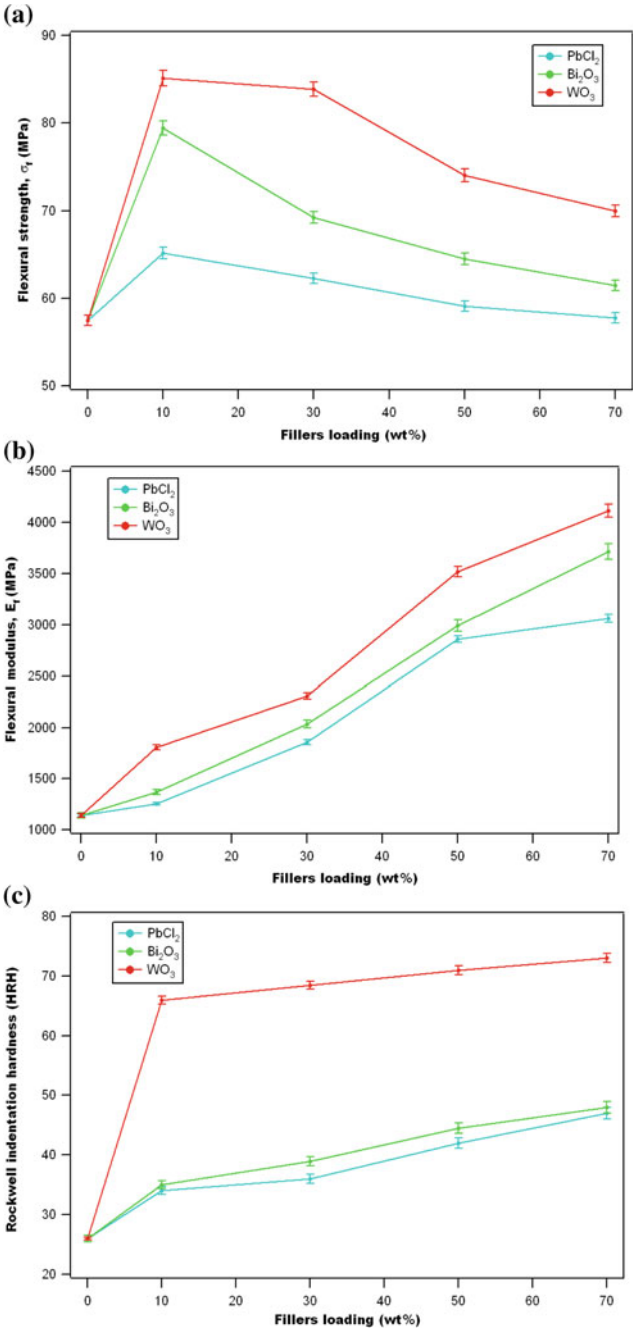

Fig. 4.4 The effect of filler loading on **a** flexural strength; **b** flexural modulus and **c** hardness of epoxy-composites [23]

to the filler not well dispersed within the epoxy matrix. In addition, the porosity for the samples was between 1 and 10% with more pores for filler ≥30 wt% because of air-bubbles trapped in the samples which act as stress-concentrators and thus the resultant weakening. On the other hand, the flexural modulus increased with an increase in filler loading which suggests that the stiffness of the composites obey the rule-of-mixtures. In comparison, the flexural strength and flexural modulus of lead glass are ~90 MPa and ~6500 MPa respectively, thus indicating that glass is still superior to epoxy. For the hardness results, they show that an increase in the filler loading resulted in a modest increase in hardness of the composite. In comparison, the Rockwell hardness of lead glass is ~HRC 043 [22].

The mechanical properties obtained in this work are adequate for the optimum sample (i.e. 70 wt% Bi_2O_3-epoxy composite) in X-ray shielding of radiological rooms since it is comparable with lead glass in terms of X-ray transmission although it shows lower flexural properties than lead glass. In particular, the mechanical properties of the composite did not change even after being repeatedly exposed to the X-ray beam of highest X-ray tube voltage. Although these flexural properties are inferior when compared to lead glass, this limitation can be overcome by increasing the thickness of the 70 wt% Bi_2O_3-epoxy composite.

4.3 Conclusions

It may be concluded that:

- $PbCl_2$, Bi_2O_3 or WO_3-epoxy composites have good X-ray shielding ability and hence they can be considered as candidate materials for X-ray shielding of radiological rooms.
- The 8 mm thick Bi_2O_3-epoxy composite with 70 wt% Bi_2O_3 is comparable with a 10 mm thick commercial lead glass which contains 56 wt% Pb.
- The 8 mm thick $PbCl_2$- and WO_3-epoxy composites were not comparable with the 10 mm thick lead glass unless they were prepared with a thickness greater than 10 mm.
- Both flexural modulus and hardness of composites increased with increasing filler loading but the flexural strength decreased markedly when the filler loading was equal or greater than 30 wt%.

Acknowledgements The collection of synchrotron powder diffraction data was funded by the Australian Synchrotron (PD3509).

References

1. Holmes-Siedle L (2002) Adams, hand book of radiation effects, 2nd edn. Oxford University Press, England
2. El Haber F, Froyer G (2008) Transparent polymers embedding nanoparticles for x-rays attenuation (Review). J Univ Chem Technol Metall 43:283
3. Schmid E, Panzer W, Schlattl H, Eder H (2012) Emission of fluorescent x-radiation from non-lead based shielding materials of protective clothing: a radiobiological problem? J Radiol Prot 32:129
4. Sutton DG, Martin CJ, Peet D, Williams JR (2012) Radiation shielding for diagnostic radiology. Report of a BIR working party. 2nd edn. London, UK: British Institute of Radiology. J Radiol Prot 32:117
5. Sprawls P (1993) The physical principles of medical imaging. Aspen Publishers, Gaithersburg, Md.
6. Arjula S, Harsha A, Ghosh M (2008) Solid-particle erosion behavior of high-performance thermoplastic polymers. J Mater Sci 43:1757
7. Dworecki K, Drabik M, Hasegawa T, Wąsik S (2004) Modification of polymer membranes by ion implantation. Nucl Instrum Methods Phys Res Sect B: Beam Interact Mater Atoms 225:483
8. Hubler GK (1981) Use of ion beam analysis in metal modification by means of ion implantation. Nucl Instrum Methods Phys Res 191:101
9. Soares MRF, Alegaonkar P, Behar M, Fink D, Müller M (2004) 6Li+ ion implantation into polystyrene. Nucl Instrum Methods Phys Res Sect B 218:300
10. Kim JK, Robertson RE (1992) Toughening of thermoset polymers by rigid crystalline particles. J Mater Sci 27:161
11. Daren S, Polymer versus Glass, POLYMICRO Newsletter, http://www.polymicro-cc.com. Accessed 16 July 2010
12. Lee EH, Rao GR, Lewis MB, Mansur LK (1993) Ion beam application for improved polymer surface properties. Nucl Instrum Methods Phys Res Sect B: Beam Interact Mater Atoms 74:326
13. Andreopoulos AG, Papanicolaou GC (1987) Rubber-modified polymer composites. J Mater Sci 22:3417
14. Harish V, Nagaiah N, Prabhu TN, Varughese KT (2009) Preparation and characterization of lead monoxide filled unsaturated polyester based polymer composites for gamma radiation shielding applications. J Appl Polym Sci 112:1503
15. Abdel-Aziz MM, Badran AS, Abdel-Hakem AA, Helaly FM, Moustafa AB (1991) Styrene-butadiene rubber/lead oxide composites as gamma radiation shields. J Appl Polym Sci 42:1073
16. Pavlenko VI, Lipkanskii VM, Yastrebinskii PN (2004) Calculations of the passage of gamma-quanta through a polymer radiation-protective composite. J Eng Phys Thermophys 77:11
17. Osei-Mensah W, Fletcher JJ, Danso KA (2012) Assessment of radiation shielding properties of polyester steel composite using MCNP5. Int J Sci Technol 2:455
18. Liu L, He L, Yang C, Zhang W, Jin R-G, Zhang L-Q (2004) Influence of reaction-induced phase decomposition to dispersion of samarium acrylic acid (Sm(AA) 3) in rubber and shielding property of Sm(AA) 3/NR composites. Macromol Rapid Commun 25:1197
19. Premac Lead Acrylic, Part of the Wardray premise total radiation shielding package, Wardray Premise Ltd., http://wardray-premise.com/structural/materials/premac.html. Accessed 4 May 2011
20. Radiation Safety & Consumable Products. In: Limited LS (ed) Lablogic, Sheffield, United Kingdom (2009). http://www.lablogic.com/moreinfo/PDF/consumables/lablogic_consumables_brochure.pdf. Accessed 9 June 2010
21. Noor Azman NZ, Siddiqui SA, Hart R, Low IM (2013) Effect of particle size, filler loadings and x-ray tube voltage on the transmitted x-ray transmission in tungsten oxide-epoxy composites. Appl Radiat Isot 71:62

22. Data sheet lead glass (X-ray protection), UQG Optics, http://www.uqgoptics.com/pdf/Lead%20Glass.pdf. Accessed 9 Nov 2012
23. Noor Azman NZ, Siddiqui SA, Low IM (2013) Synthesis and characterization of epoxy composites filled with Pb, Bi or W compound for shielding of diagnostic x-rays. Appl Phys A 110:137

Chapter 5
Effect of Particle Size, Filler Loadings and X-Ray Energy on the X-Ray Attenuation Ability of Tungsten Oxide–Epoxy Composites

Abstract The effect of particle size, filler loadings and X-ray energy on the transmitted X-ray beam intensity by WO_3-epoxy composites has been investigated using the mammography unit and a general radiography unit. Results indicate that nano-sized WO_3 has a better ability to attenuate X-ray produced by lower X-ray tube voltages (22–35 kV) when compared to micro-sized WO_3 of the same filler loading. However, the role of particle size on transmitted X-ray beam intensity was negligible at the higher X-ray tube voltage range (40–120 kV).

5.1 Introduction

The use of nanoparticles in designing advanced materials has attracted much attraction amongst the researchers because of superior physical and mechanical properties that can be achieved. For instance, recent studies have shown that nano-sized filler reinforced polymer composites provided much improvement in chemical, physical and mechanical properties by virtue of better dispersion of the nanoparticles within the polymer matrix [1–4]. The main improvement of nanoparticles as a filler assembly over conventional materials is the maximization of the surface/volume ratio of the fillers [5]. For example, nano-particles improved the electrochemical capacitance of α-$Ni(OH)_2$ in alkali solutions as compared to micro-sized particles of the same hydroxide due to the greater surface/volume ratio of the nano-particles [6].

Additionally, this size-effect also becomes one of the virtues in designing materials for shielding of ionizing radiations. Some X-ray technologists believe that this effect will improve the X-ray attenuation ability of the composite since nano-sized fillers are able to disperse more uniformly within the polymer matrix with less agglomeration as compared to micro-sized fillers [7–9]. A recent study by Botelho et al. [7] found that nanostructured copper oxide (CuO) is more effective in attenuation of lower X-ray beam energy (26 and 30 kV) and no significant variation in X-ray attenuation at higher X-ray beam energy 60 and 102 kV). Kunzel et al. [10] also provided similar results, which show that the X-ray absorption is higher for a nanostructured CuO compound compared to the microstructured counterpart for low energy X-ray beams (25 and 30 kV) for all CuO concentrations incorporated into polymeric resin.

© Springer Nature Singapore Pte Ltd. 2020

I. M. Low and N. Z. Noor Azman, *Polymer Composites and Nanocomposites for X-Rays Shielding*, Composites Science and Technology,
https://doi.org/10.1007/978-981-13-9810-0_5

In general, the attenuation of photons (X-rays/gamma-rays) is dependent upon three factors: density, elemental composition, and thickness of the absorbing material [11]. Even though lead (Pb) or lead compounds provide good X-ray shielding properties, their usage as the shielding materials has increasingly become a sensitive issue due to its hazardous nature. As a result, much research has been focusing on developing new X-ray shielding materials which are safer and easier to handle [12, 13].

The aim of this work was to develop new X-ray shielding materials based on tungsten oxide-epoxy composites with either nano-sized or micro-sized fillers. The effect of filler size on the X-ray attenuation in the diagnostic imaging energy range (22–120 kV) has been investigated. The filler size effect in X-ray shielding ability is discussed.

5.2 Results and Discussion

Three different anode/filter combinations (Table 2.4) were used for low energy range X-rays transmitted from the mammography machine, since the combination was operated by the machine itself. The X-ray beams generated by these anode/filter combinations composed mainly of the characteristic X-ray energies of molybdenum (17.5 and 19.6 keV) or rhodium (20.2 and 22.7 keV). For WO_3 of 5 and 10 wt%, the exit dose reading was observed at 22 kV X-ray energy while for 20–35 wt%, the dose reading was initiated at 30 kV X-ray energy due to the zero reading of the dosimeter at 22 and 25 kV X-ray tube voltages.

Results in Fig. 5.1a, b clearly show a big difference in the transmitted X-ray beam intensity between the micro-sized WO_3-epoxy composite and the nano-sized WO_3-epoxy composite at 22–49 kV generated by the mammography unit at the same filler loading. The ratio of transmitted X-ray beam intensity for the micro-sized WO_3-epoxy composite (T_m) to transmitted X-ray beam intensity for the nano-sized WO_3-epoxy composite (T_n); (T_m/T_n) was in the range 1.3–3.0. The ratio (T_m/T_n) was larger at the X-ray tube voltages ranges 22–35 kV and was decreasing as the X-ray energy increased ($\geq$40 kV up to 49 kV) as shown in Fig. 5.1a, b. In contrast, the ratio (T_m/T_n) is $\approx$1.0, for the diagnostic X-ray tube voltages range (40–120 kV) generated by the general radiography unit, which suggests $T_m \approx T_n$. Thus, the size effect of WO_3 particles was negligible at the X-ray beam produced by higher X-ray tube voltage range (Fig. 5.2).

Besides that, Fig. 5.3 showed that the value of T_n by the nano-sized WO_3 epoxy composite is higher for the X-ray photon generated by 40 kV of the mammography unit compared to the same X-ray tube voltage (40 kV) selected from general radiography unit. A similar result was also obtained for micro-sized WO_3 epoxy composite (T_m). This outcome proved that the general radiography unit comprised of a continuous spectrum of X-rays energy, which is having lower equivalent energies as compared to the characteristic X-ray energies produced from the mammography unit (17.5–22.7 keV).

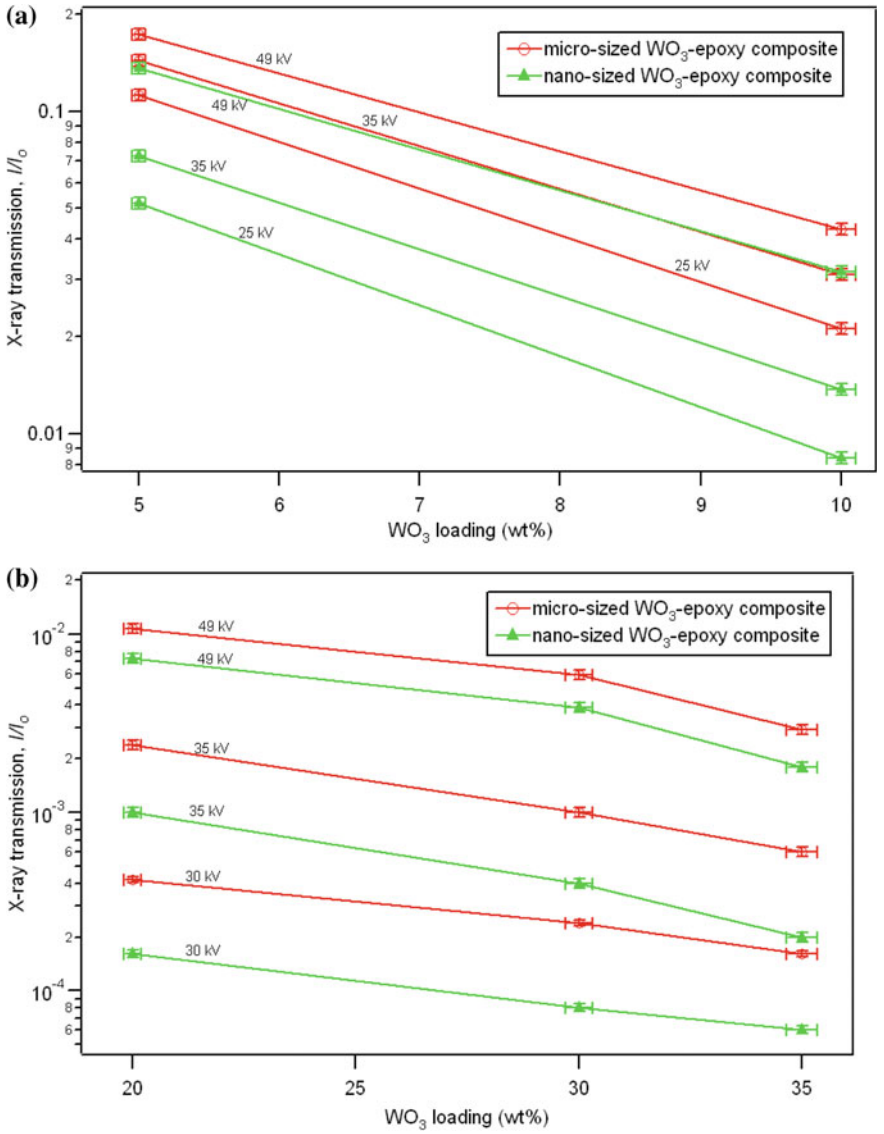

Fig. 5.1 X-ray transmission as a function of filler loading of **a** 5 and 10 wt% of the nano-sized WO_3-epoxy composite for X-ray tube voltage of 25, 35 and 49 kV generated by mammography unit and **b** 20–35 wt% of the nano-sized WO_3-epoxy composite as compared to the micro-sized WO_3-epoxy composite for X-ray tube voltage of 30, 35 and 49 kV generated by mammography unit [14]

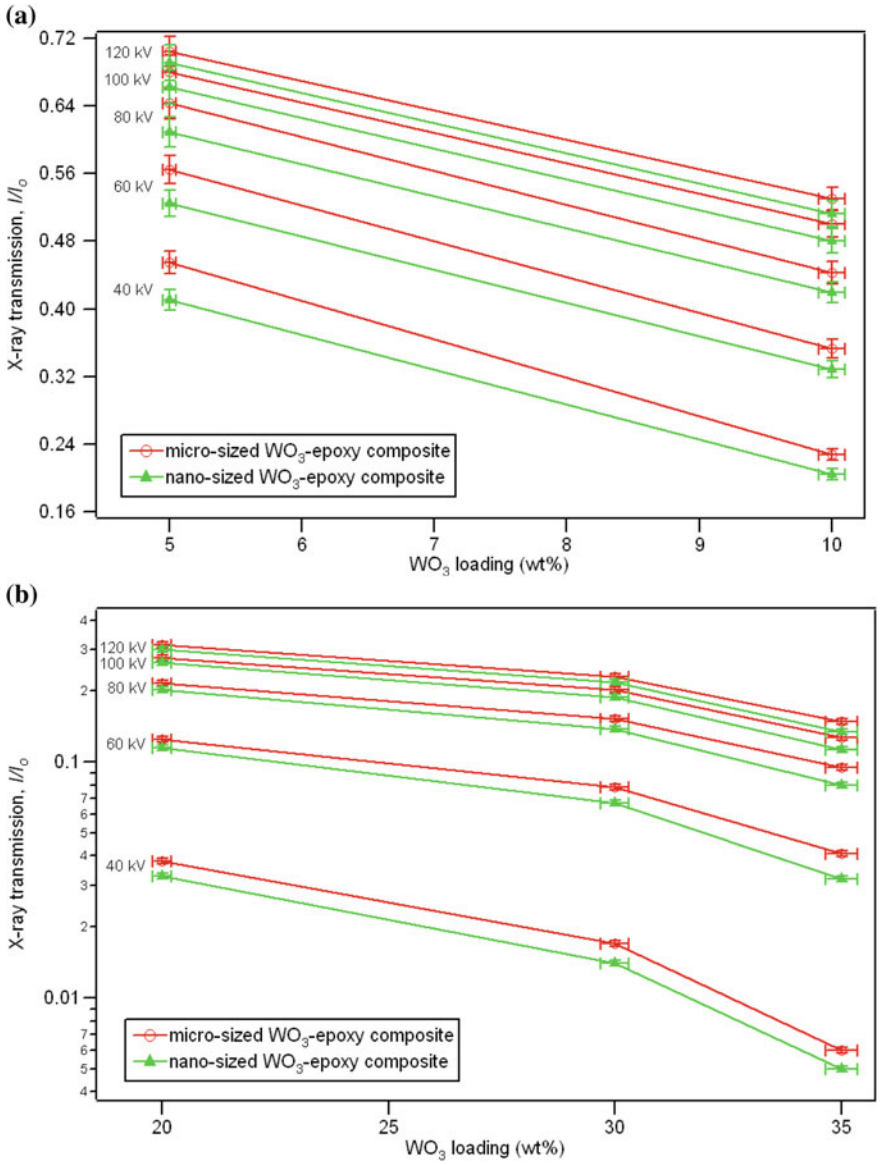

Fig. 5.2 X-ray transmission as a function of filler loading of **a** 5 and 10 wt% and **b** 20–35 wt% of the nano-sized WO_3-epoxy composite as compared to the micro-sized WO_3-epoxy composite for X-ray tube voltage of 40–120 kV generated by general radiography unit [14]

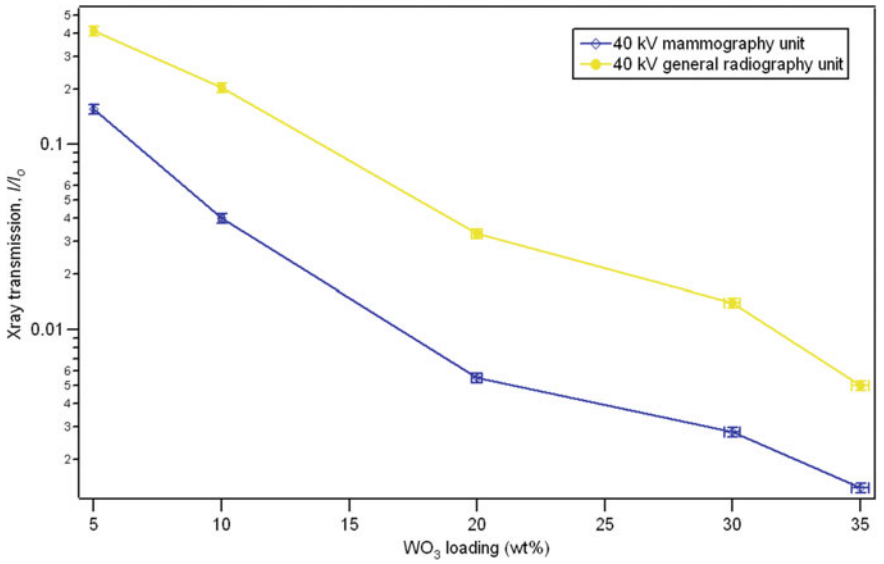

Fig. 5.3 Comparison of transmitted X-rays beam intensity values for all nano-sized WO_3 wt% loading in epoxy sample for 40 kV X-ray energy used by the mammography unit and the general radiography unit [14]

Generally, photoelectric absorption dominates at lower photon (X-ray) energies range. A photon is completely absorbed by the atom of the material, and a photoelectron is ejected in the process. The ejected photoelectrons may undergo single- or multiple-scattering events with neighboring atoms, which can alter the mass attenuation coefficient of an element relative to the bulk material when considered over a small range of X-ray energies together with slight fluctuations in the probability of emission of Auger electron and fluorescent photons. The probability of the photoelectric interaction is approximately dependent on Z^3/E^3 where Z is atomic number of the absorbing material and E is the photon energy. Furthermore, the number of W particles/gram in the nano-sized WO_3-epoxy composite is higher than that for the micro-sized WO_3-epoxy composite. Thus, the probability of an X-ray with lower energy to interact and to be absorbed may be higher for nano-sized WO_3-epoxy composite rather than micro-sized WO_3-epoxy composite.

As photon energy increases, the probability of Compton scattering increases and hence the attenuation by the material decreases since this interaction was weakly dependent on Z and E. Hence, the probability of an X-ray photon with higher energy to interact and to be absorbed may be similar for nano-sized and micro-sized WO_3-epoxy composite.

To support our attenuation results for low X-ray photon energies, we have repeated the procedure to measure transmitted X-ray beam intensity of a WO_3 compact disc of the same mass for 20 wt% (31% porosity) and 35 wt% (34% porosity) of WO_3 loading in the epoxy composite sample. The results in Fig. 5.4a, b clearly show that

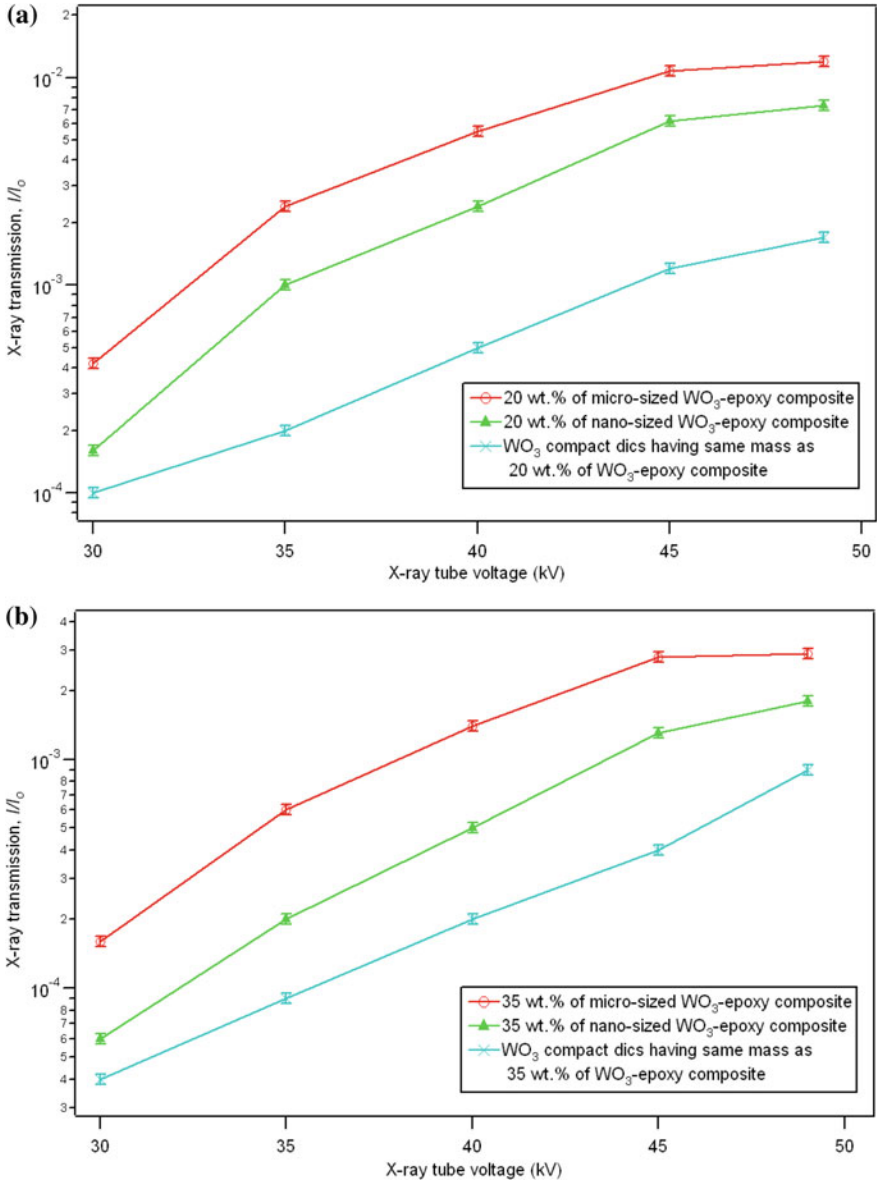

Fig. 5.4 X-ray transmission for WO_3 compact disc as compared to both micro-sized and nano-sized WO_3-epoxy composite of the same mass of **a** 20 wt% and **b** 35 wt% of WO_3 loading in epoxy sample for X-ray tube voltage range (30–49 kV) generated by mammography unit [14]

the WO_3 compact disc has the lowest T when compared to both micro-sized and nano-sized WO_3-epoxy composite of the same mass since WO_3 particles have been compressed closer together instead of being dispersed in the epoxy matrix.

Hence, the results obtained in this work are in good agreement with the work of Kunzel et al. [10] which showed that nano-sized fillers are superior to micro-sized fillers for attenuating lower X-ray energy but for the higher energy range, the effect is the same [10].

5.3 Conclusions

The results of this work showed that for the same WO_3 loading, nano-sized WO_3-epoxy composite has better X-ray attenuating ability in the lower X-ray tube voltage range (22–35 kV) when compared to the micro-sized WO_3-epoxy composite. However, the role of particle size in X-ray shielding was insignificant at the higher X-ray tube voltage range (40–120 kV).

References

1. Chapman R, Mulvaney P (2001) Electro-optical shifts in silver nanoparticle films. Chem Phys Lett 349:358–362
2. Karim A, Amis E, Yurekli K, Krishnamoorti R, Meredith C (2002) Combinatorial methods for polymer materials science: phase behavior of nanocomposite blend films. Polym Eng Sci 42:1836–1840
3. Ohno K, Koh KM, Tsujii Y, Fukuda T (2002) Synthesis of gold nanoparticles coated with well-defined, high-density polymer brushes by surface-initiated living radical polymerization. Macromolecules 35:8989–8993
4. Schmidt G, Malwitz MM (2003) Properties of polymer-nanoparticle composites. Curr Opin Colloid Interface Sci 8:103–108
5. Fabiani D, Montanari GC, Krivda A, Schmidt LE, Hollertz R (2010) Epoxy based materials containing micro and nano sized fillers for improved electrical characteristics. In: 2010 international conference on solid dielectrics. IEEE, Potsdam, Germany, pp 1–4
6. Jayalakshmi M, Mohan Rao M, Kim KB (2006) Effect of particle size on the electrochemical capacitance of a-$Ni(OH)_2$ in alkali solutions. Int J Electrochem Sci, 324–333
7. Botelho MZ, Künzel R, Okuno E, Levenhagen RS, Basegio T, Bergmann CP (2011) X-ray transmission through nanostructured and microstructured CuO materials. Appl Radiat Isot 69:527–530
8. El Haber F, Froyer G (2008) Transparent polymers embedding nanoparticles for X-rays attenuation (Review). J Univ Chem Technol Metall 43:283–290
9. Steinhart M (2004) Introduction to Nanotechnology. By Charles P. Poole, Jr. and Frank. J Owens Angew Chem Int Ed 43:2196–2197
10. Künzel R, Okuno E (2012) Effects of the particle sizes and concentrations on the X-ray absorption by CuO compounds. Appl Radiat Isot 70:781–784
11. Sprawls P (1993) The physical principles of medical imaging, 2nd edn. Aspen Publishers, Gaithersburg
12. Robert RD (2005) High density composites replace lead. Ecomass Technologies

13. Spinks JWT, Wood RJ (1976) An introduction to radiation chemistry, 2nd edn. Wiley-Interscience, New York
14. Noor Azman NZ, Siddiqui SA, Hart R, Low IM (2013) Effect of particle size, filler loadings and X-ray tube voltage on the transmitted X-ray transmission in tungsten oxide—epoxy composites. Appl Radiat Isot 71:62–67

Chapter 6
Characterisation of Micro-Sized and Nano-Sized Tungsten Oxide-Epoxy Composites for Radiation Shielding of Diagnostic X-Rays

Abstract Characteristics of X-ray transmissions were investigated for epoxy composites filled with 2–10 vol.% WO_3 loadings using synchrotron X-ray Absorption Spectroscopy (XAS) at 10–40 keV. The results obtained were used to determine the equivalent X-ray energies for the operating X-ray tube voltages of mammography and radiology machines. The results confirmed the superior attenuation ability of nano-sized WO_3-epoxy composites in the energy range of 10–25 keV when compared to their micro-sized counterparts. However, at higher synchrotron radiation energies (i.e., 30–40 keV), the X-ray transmission characteristics were similar with no apparent size effect for both nano-sized and micro-sized WO_3-epoxy composites. The equivalent X-ray energies for the operating X-ray tube voltages of the mammography unit (25–49 kV) were in the range of 15–25 keV. Similarly, for a radiology unit operating at 40–60 kV, the equivalent energy range was 25–40 keV, and for operating voltages greater than 60 kV (i.e., 70–100 kV), the equivalent energy was in excess of 40 keV. The mechanical properties of epoxy composites increased initially with an increase in the filler loading but a further increase in the WO_3 loading resulted in deterioration of flexural strength, modulus and hardness.

6.1 Introduction

Hitherto, numerous analytical methods have been developed to investigate the effect of the particle size of a material on the X-ray attenuation for various incoming X-ray energies including scattered gamma-rays and X-rays [1–11]. It is widely believed that nano-sized particles are able to disperse more uniformly within the matrix with fewer agglomerations when compared to micro-sized particles, thus improving the X-ray attenuation ability of the material [6, 12, 13]. For instance, Hołyńska [4] found that the intensity of scattered radiations increased with increases in the grain size of a material. This size effect has been observed in a sand matrix and for samples containing heavy elements such as iron or barium [4].

Filler-reinforced polymers have gained increasing attention from X-ray technologists in radiation shielding since polymers have great potential in many important applications by virtue of their unique properties, such as low density, the ability to

© Springer Nature Singapore Pte Ltd. 2020

I. M. Low and N. Z. Noor Azman, *Polymer Composites and Nanocomposites for X-Rays Shielding*, Composites Science and Technology,
https://doi.org/10.1007/978-981-13-9810-0_6

form intricate shapes, optical transparency, low manufacturing cost and toughness. One of the filler-reinforced polymers commonly used for radiation shielding is lead acrylic [14–16]. Moreover, some researchers have also tried to synthesise nano-sized filler-reinforced polymers for radiation shielding by virtue of the size effect in X-ray attenuation [2, 6, 17]. For instance, a recent study by Botelho et al. [13] revealed that the attenuation for X-ray beams generated from low tube voltages (i.e., 26–30 kV) in nanostructured copper oxide (CuO) was better than microstructured CuO. However, no significant difference in attenuation was observed for X-rays generated from higher tube voltages (i.e., 60–102 kV). A similar conclusion on this size effect in X-ray attenuation was made by Künzel and Okuno [18] for a nanostructured CuO-polymer system.

In a recent work on WO_3-filled epoxy composites [19], we investigated the effect of nano-sized and micro-sized WO_3 filler-epoxy composites on X-ray attenuation in the X-ray tube voltage range of 22–127 kV generated by a mammography unit and a general radiography unit. The equivalent X-ray energies for the various X-ray tube voltages used were in the range of 17.5–60 keV, which conformed to our expectation since the equivalent X-ray energies for a mammography unit were 17.5, 19.6, 20.2 and 22.7 keV which are the characteristic energies of molybdenum and rhodium; while the equivalent X-ray energy for a radiology unit is about one-third of the X-ray tube voltage used. The results showed that nano sized WO_3 was more effective than micro-sized WO_3 in X-ray attenuation only in the low X-ray tube voltage range of 22–35 kV but this size effect was not apparent at the higher X-ray operating tube voltage range of 40–120 kV [19]. Hence, the aim of this work was to verify our previous work on X-ray transmission in WO_3-filled epoxy composites by using synchrotron radiations as the X-ray source for the characteristic (monochromatic) X-ray energy range of 10–40 keV. The results obtained were compared with those of previous work [19] to determine the equivalent energy range of the previous machines used (a mammography unit and a radiology unit).

6.2 Results and Discussion

6.2.1 Characteristics of X-Ray Transmissions

Since the synchrotron radiations of the XAS beamline contain a large range of energies (i.e., 10–40 keV), the thickness of the samples was set at 2 mm to ensure that the detector was able to obtain a meaningful X-ray transmission reading for the lower energy range without being totally absorbed by the samples. As shown in Fig. 6.1, there was an obvious difference in X-ray transmissions between the micro-sized WO_3-epoxy and nano-sized WO_3-epoxy composites of the same WO_3 vol.% at the energy range of 10–20 keV. With a further increase of synchrotron energy to greater than 20 keV, there was no difference in X-ray transmissions between these two composites, thus indicating the absence of size effect at play. The results show that for

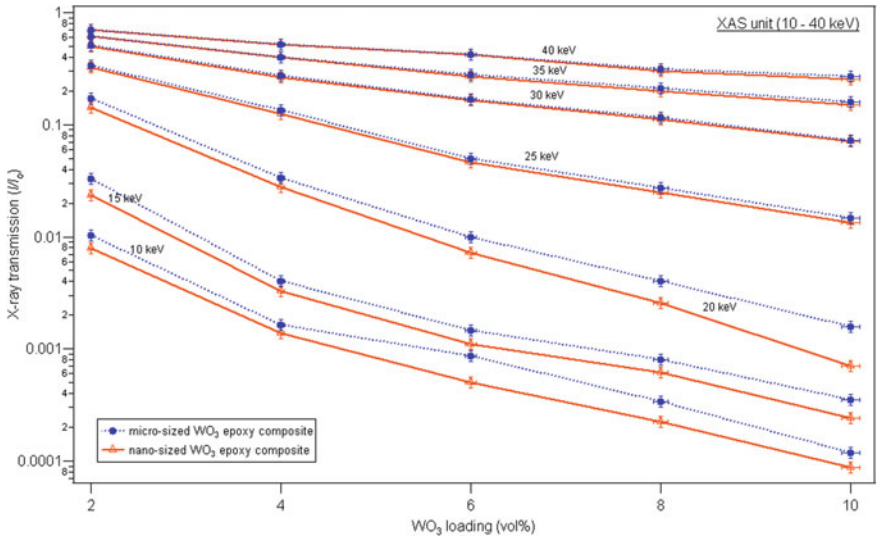

Fig. 6.1 Comparisons of X-ray transmission comparison in nano-sized and micro-sized WO_3-epoxy composites for synchrotron radiation generated by the XAS unit for energy of 10–40 keV [20]

all the WO_3 loadings in an epoxy matrix, the ratio of the X-ray transmission of the micro-sized WO_3-epoxy composite $(I/I_o)_m$ relative to the nano-sized WO_3-epoxy composite $(I/I_o)_n$, $(I/I_o)_m/(I/I_o)_n$ remained at ~1.0 for the synchrotron energy range of 25–40 keV. On the other hand, the ratio $(I/I_o)_m/(I/I_o)_n$ was 1.15–2.3 for all WO_3 loadings (see Fig. 6.2). The values determined for $(I/I_o)_m/(I/I_o)_n$ at these energy ranges indicate that the nano-sized WO_3-epoxy samples absorbed more low energy X-rays than their micro-sized WO_3-epoxy counterparts.

Further investigations were conducted to verify our previous results [19] obtained from a mammography unit and a radiography unit. In this investigation, all the same measurements from the previous work were repeated with samples of 2 mm in thickness. Since a mammography unit generates characteristic X-ray energies of molybdenum (17.5 and 19.6 keV) or rhodium (20.2 and 22.7 keV), it is much easier to compare with the XAS results (see Fig. 6.3). In the results presented in Fig. 6.3, it is clearly shown that the X-ray transmission results for the mammography unit sat between the results of 15–25 keV for the XAS beam energies. In contrast, for the radiography unit, the operated X-ray tube voltages generated a broad spectrum (polychromatic X-ray beam). Thus, the equivalent energies for the X-ray tube voltages of the radiography unit were estimated from the XAS results by superimposing their data together (see Fig. 6.4). As can be seen in Fig. 6.4, the X-ray transmissions of samples for X-ray tube voltages of 40–60 kV were sitting between 25 and 40 keV while the others were sitting above 40 keV. Hence, the X-ray tube voltages of 40–60 kV operated by the radiography unit produced the equivalent X-ray energies in

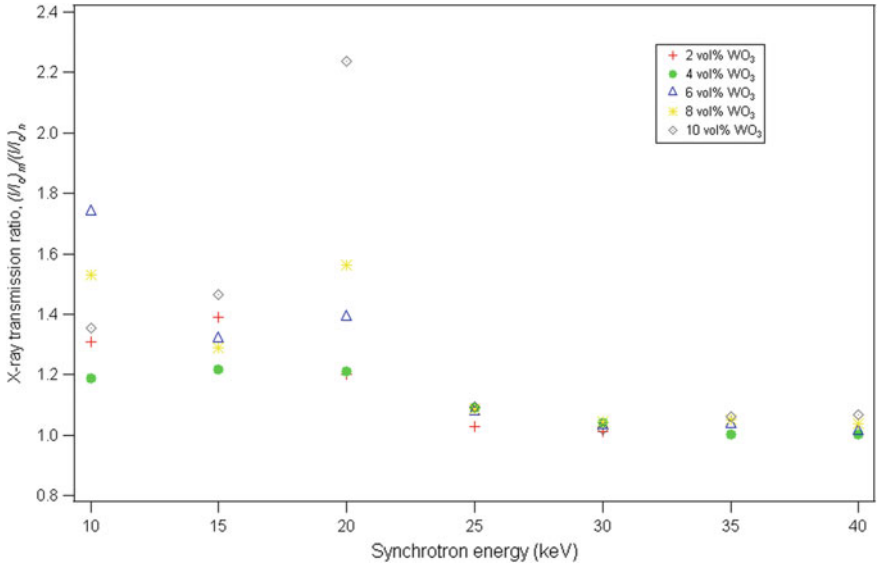

Fig. 6.2 The X-ray transmission ratio of micro-sized WO_3-epoxy composite $(I/I_o)_m$ to the X-ray transmission for nano-sized WO_3-epoxy composite $(I/I_o)_n$, $(I/I_o)_m/(I/I_o)_n$ for synchrotron energies (10–40 keV) [20]

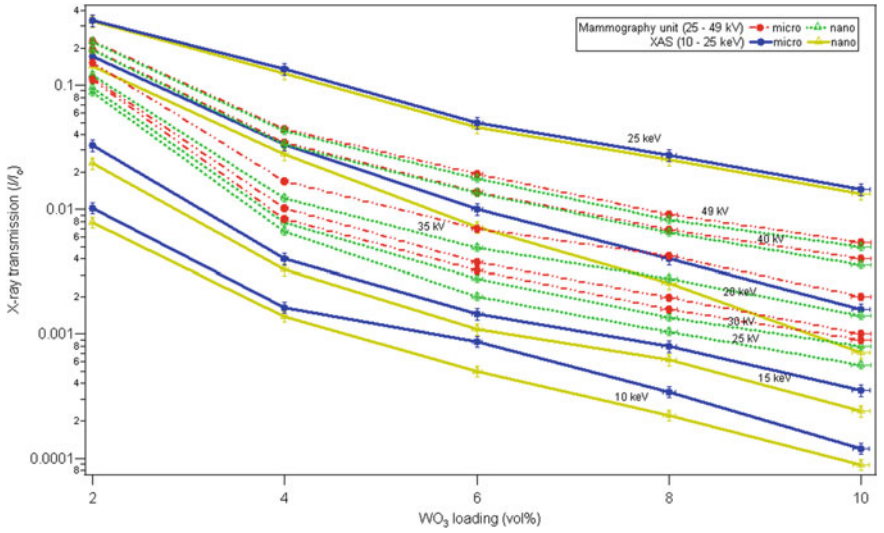

Fig. 6.3 Comparisons of X-ray transmission in nano-sized and micro-sized WO_3-epoxy composites for synchrotron radiation generated by the XAS unit for energies of 10–25 keV and mammography unit tube voltages of 25–49 kV [20]

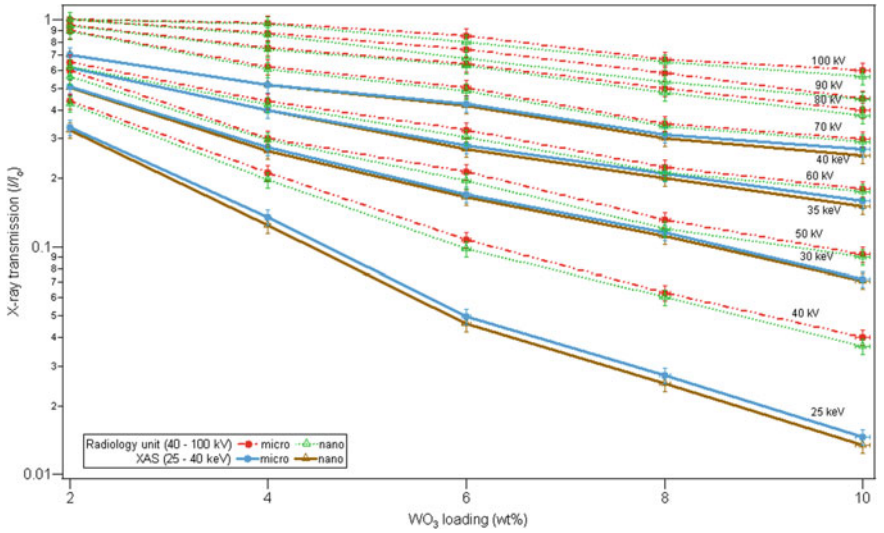

Fig. 6.4 Comparisons of X-ray transmission in nano-sized and micro-sized WO_3-epoxy composites for synchrotron radiation generated by the XAS unit for energies of 25–40 keV and radiography unit tube voltages of 40–100 kV [20]

the range of 25–40 keV while the X-ray tube voltages of ≥60 kV had an equivalent energy of ≥40 keV.

Figure 6.5 shows the comparison of X-ray transmissions for samples with different thicknesses. Samples of 7 mm thickness were used in our previous study [19], whereas 2 mm thick samples were used in this study. Figure 6.5a, b provide the results for the mammography unit only on samples with 4 and 6 vol.% loading of WO_3 respectively. As shown in these figures, the differences in the X-ray transmission between the micro-sized and nano-sized WO_3-epoxy became larger for thicker samples (7 mm). In contrast, Fig. 6.5c shows insignificant differences in X-ray transmission between nano-sized and micro-sized WO_3-epoxy composites for radiography tube voltages only for samples with a loading of 4 vol.% WO_3. This trend was also observed for all the other loadings (i.e., 2, 6, 8 and 10 vol.% WO_3). These findings are in good agreement with the work by Künzel and Okuno [18], which also showed that the grain size effect increased with the increase of the sample thickness at low energy X-ray beams (25 and 30 kV) but remained unchanged over the material thickness for higher energy X-ray beams (60 kV) [18].

In general, the photoelectric effect is the most likely interaction to occur within a matter at a lower photon (X-ray) energy range. In this interaction, a photon will transfer its entire energy to an electron in the material on which it impinges. The electron thereby acquires enough energies to free itself from the material to which it is bound and then may undergo single or multiple-scattering events with neighbouring atoms. In addition, there is also a slight fluctuation in the probability of emission of Auger electrons and fluorescent photons may form during this interaction. This

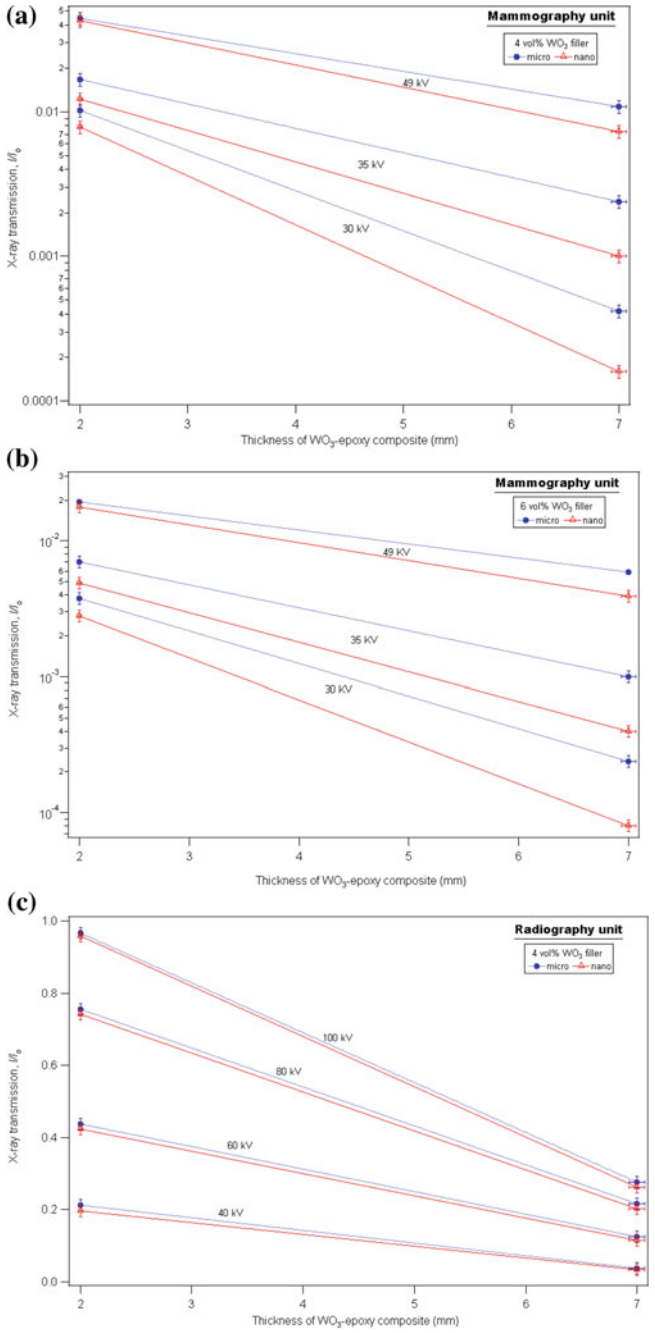

Fig. 6.5 X-ray transmission comparison for different thickness of the sample for **a** 4 vol.% of WO_3 filler epoxy composites for mammography unit tube voltages of 30, 35 and 49 kV; **b** 6 vol.% of WO_3 filler epoxy composites for mammography unit tube voltages of 30, 35 and 49 kV; and **c** 4 vol.% of WO_3 filler epoxy composites for radiography unit tube voltages of 40, 60, 80 and 100 kV [20]

phenomenon can contribute to the alteration of the mass attenuation coefficient of an element relative to the bulk material when considered over a small range of X-ray energies. The probability of photoelectric interaction is directly proportional to the cube of the atomic number of the absorbing material Z^3 and inversely proportional to the cube of the X-ray energy $(1/E)^3$.

Moreover, nano-sized WO_3-epoxy composites consist of a higher number of WO_3 particles/gram when compared to micro-sized WO_3-epoxy composites. Therefore, the distribution of the nano sized WO_3 in the resin should also be different from that presented by micro-sized WO_3, thus resulting in a more uniform dispersion in the resin. Therefore, the chances of an X-ray photon with lower energy to interact and be absorbed by WO_3 particles may be higher in nano-sized WO_3-epoxy composites than in micro-sized WO_3-epoxy composites. Figure 6.6 shows the back-scattered images of the same loading of WO_3 (4 vol.%) within nano-sized WO_3-epoxy and micro-sized WO_3-epoxy composites using the Zeiss Evo 40XVP scanning electron microscope. The WO_3 particles were seen to be more closely dispersed in the nano-sized WO_3-epoxy composite (Fig. 6.6a) as compared to its micro-sized counterpart (Fig. 6.6b). Thus, the probability for the lower energy photons to interact with the WO_3 particles and be absorbed is higher for the nano-sized WO_3-epoxy composite.

As the photon energy increases, the photon (X-ray) penetration through the absorbing material without interaction increases and hence, less photoelectric effect relative to the Compton affect occurs. Thus, the X-ray attenuation by the absorbing material decreased since the Compton interaction was weakly dependent on Z and E and this interaction only took place between the incident photon and one of the outer shell electrons of an atom in the absorbing material.

In order to discover the X-ray shielding ability of the composites, the results were compared to commercial lead (Pb) sheets (model RAS20 Calibrated Absorber Set) of four different thicknesses (i.e., 0.81, 1.63, 3.18 and 6.35 mm) (see Fig. 6.7) using a radiography unit of tube voltages 40–100 kV. The results show that although the lead sheets gave the lowest X-ray transmissions at each tube voltage when compared to

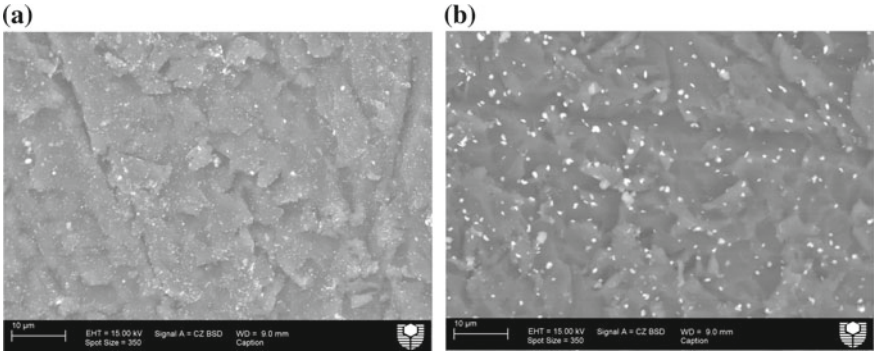

Fig. 6.6 SEM images for epoxy composites filled with **a** 4 vol.% nano-sized WO_3, and **b** 4 vol.% of micro-sized WO_3 [20]

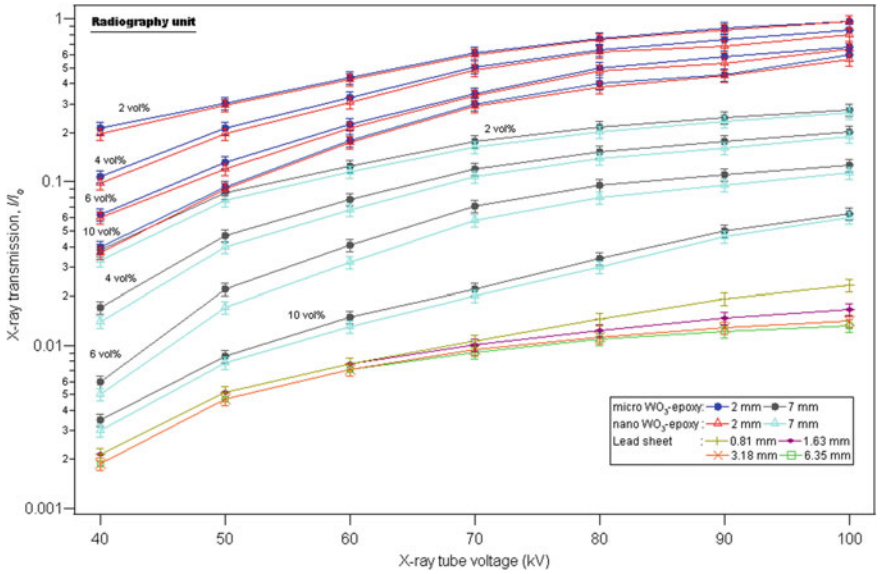

Fig. 6.7 X-ray transmission as a function of radiography unit X-ray tube voltage (40–100 kV) for all micro-sized and nano-sized WO_3-epoxy composites and commercial lead sheets [20]

all compositions of WO_3-epoxy composites, the latter with 10 vol.% of either micro-sized or nano-sized WO_3 can be a substitute for Pb in X-ray shielding by increasing the sample thickness to $\geq$7 mm. Hence, the usage of lead in X-ray shielding can be substituted by WO_3 whereby W is lighter and less toxic compared to Pb.

6.2.2 Crystallite Size

The reference for fitting the peaks was taken from the International Centre for Diffraction Data PDF-4+ 2009 database. The wavelength for all of these databases was chosen to be the same as the wavelength of the synchrotron radiation used. The diffraction peaks shown in Fig. 6.8 belong to monoclinic WO_3 (PDF file 00-043-1035). These results indicate that both the micro-sized WO_3 and the nano sized WO_3 were single-phase pure without impurities.

The diffraction patterns were plotted only in the 2θ range of 9–15° to clearly show the size difference of the peaks for each micro-sized and nano-sized WO_3. As shown in Fig. 6.8, the broad peaks belonged to nanometer-sized WO_3 crystallite whereas the well-defined crystalline peaks belonged to micrometer-sized WO_3. The crystallite size determined from the Scherrer equation for nano sized WO_3 was 51.5 nm. These nano-crystallites were significantly smaller than the particle sizes provided by Sigma-Aldrich, thus indicating that at least 2 crystallites were present in each WO_3 particle of 100 nm in size.

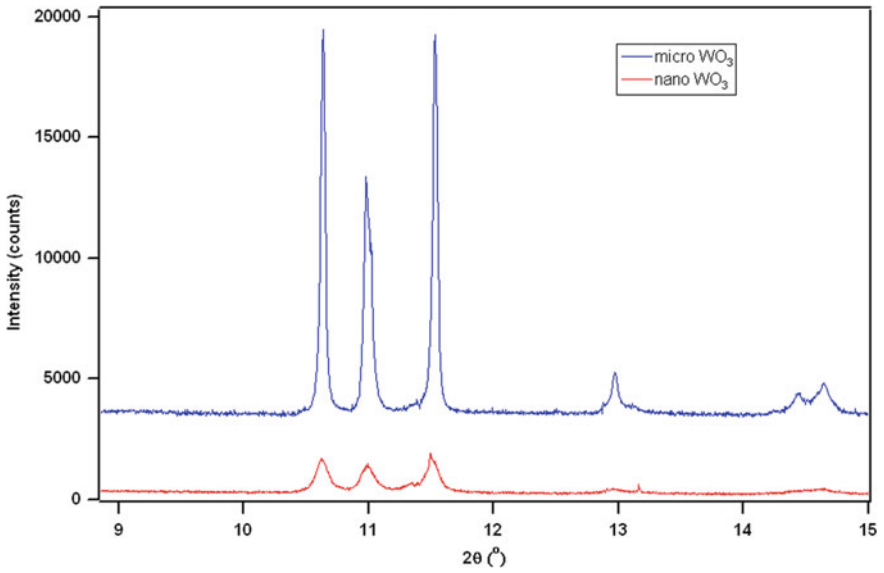

Fig. 6.8 Typical powder diffraction patterns for micro-sized and nano-sized WO_3 loading in epoxy composites [20]

6.2.3 Mechanical Properties

Figure 6.9 shows the effect of filler loading on the flexural strength, flexural modulus and Rockwell hardness of the epoxy composites. The flexural strength was found to decrease with increased WO_3 filler size while it had little or no effect on flexural modulus. Similar results were reported by Park [21] who observed an increase in flexural strength with decreased particle size in silica-reinforced epoxy composites. However, Moloney et al. [22] reported a negligible effect of particle size on flexural modulus in their epoxy composites filled with silica.

From Fig. 6.9a, the flexural strength of pure epoxy was 49.9 MPa but increased to a maximum value of 64 MPa for the composite containing 4 vol.% nano sized WO_3. However, a further increase in the filler loading beyond 4 vol.% resulted in a decrease in flexural strength whereby the composite containing 10 vol.% nano sized WO_3 exhibited the lowest flexural strength of 52.6 MPa. Similarly, for micro-sized WO_3-epoxy composites, the maximum flexural strength was obtained for a filler loading of 2 vol.%. A reduction in flexural strength was again observed when the filler loading was increased beyond 2 vol.% due to non-uniform dispersion of the filler within the matrix. The resultant agglomeration of the fillers acted as stress-concentrators which served to reduce the strength of the composites.

The flexural modulus of the composites increased with an increase in the filler loading for both the nano-sized and micro-sized WO_3 which may indicate that the stiffness of these composites obeyed the well-known rule-of-mixtures (Fig. 6.9b).

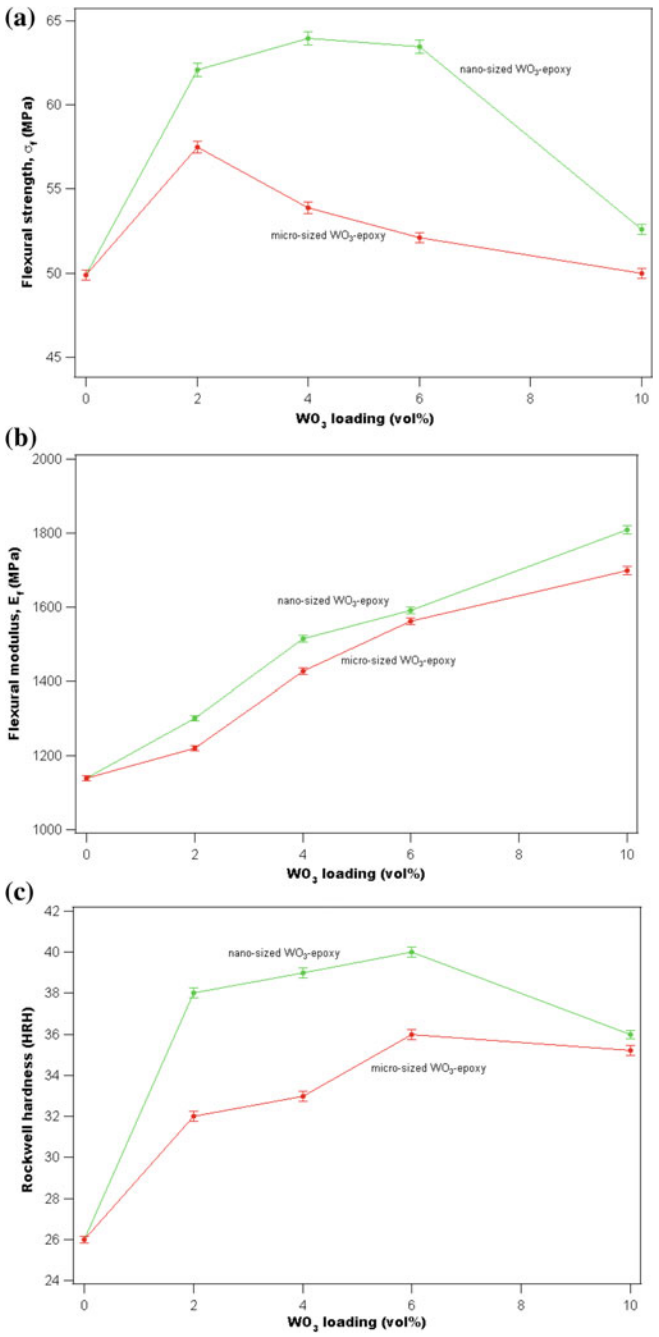

Fig. 6.9 Mechanical properties of epoxy composites showing: **a** flexural strength as a function of WO_3 filler loading; **b** flexural modulus as a function of WO_3 filler loading; and **c** Rockwell hardness as a function of WO_3 filler loading [20]

Finally, the hardness results presented in Fig. 6.9c indicate that an increase in the WO_3 filler loading resulted in an initial increase in the hardness of the composite, but a further increase in filler loading at 10 vol.% caused a reduction in hardness probably due to the undesirable agglomeration of the fillers. The initial increase in the hardness of the composites observed for both the nano-fillers and the micro-fillers may be attributed to their uniform dispersion within the epoxy matrix, together with their strong interaction with the epoxy chains to form good interfacial bonding.

6.3 Conclusions

The size effect of WO_3 particles on the X-ray transmission in nano-sized and micro-sized WO_3-epoxy composites has been investigated at various synchrotron radiation energies (i.e., 10–40 keV). The results presented in this work demonstrated that the size effect on X-ray attenuation was profoundly dependent on the energy of the synchrotron radiations. The particle size effect was more pronounced at lower synchrotron radiation energies (10–20 keV) since the X-ray transmission in nano-sized WO_3-epoxy composites was less than in their micro-sized counterparts. However, this size effect became insignificant at higher energies of 20–40 keV because the X-ray transmissions in both nano-sized and micro-sized WO_3-epoxy composites were very similar. The X-ray transmission results for the mammography unit sat between the results of 15–25 keV for XAS beam energies. Meanwhile, the X-ray transmissions in samples for X-ray tube voltages of 40–60 kV of the radiography unit sat between 25 and 40 keV. In addition, for composites with the same filler loading, but with increasing sample thickness, the size effect in X-ray transmission was most prominent for X-ray tube voltages of 25–35 kV but was negligible at 35–100 kV. As the filler loading of the WO_3 increased, the mechanical properties showed an initial optimum improvement, but a further increase in the filler loading caused these properties to deteriorate.

Acknowledgements The collection of X-ray absorption spectroscopy (XAS) data was funded by the Australian Synchrotron (AS123/XAS5341). We thank Dr. Bernt Johannessen of the Australian Synchrotron and our colleagues Dr. C. Ng and A/Prof. Z. Sun for assistance with XAS data collection. Also, we would like to thank Carolyn Madeley of Breast Assessment Centre, Royal Perth Hospital, Western Australia for giving us the opportunity to use the mammography unit.

References

1. Patra CR, Bhattacharya R, Mukhopadhyay D, Mukherjee P (2010) Fabrication of gold nanoparticles for targeted therapy in pancreatic cancer. Adv Drug Deliv Rev 62:346–361
2. Van Den Heuvel F, Locquet JP, Nuyts S (2010) Beam energy considerations for gold nanoparticle enhanced radiation treatment. Phys Med Biol 55:4509–4520

3. Wang T, Liu Z, Lu M, Wen B, Ouyang Q, Chen Y, Zhu C, Gao P, Li C, Cao M, Qi L (2013) Graphene-Fe3O4 nanohybrids: synthesis and excellent electromagnetic absorption properties. J Appl Phys 113:024314–024318
4. Hołyńska B (1969) Grain size effect in low energy gamma and X-ray scattering. Spectrochim Acta, Part B 24:85–93
5. Rad AG, Abbasi H, Afzali MH (2011) Gold nanoparticles: synthesising, characterizing and reviewing novel application in recent years. Phys Procedia 22:203–208
6. El Haber F, Froyer G (2008) Transparent polymers embedding nanoparticles for x-rays attenuation (Review). J Univ Chem Technol Metall 43:283–290
7. Jackson P, Periasamy S, Bansal V, Geso M (2011) Evaluation of the effects of gold nanoparticle shape and size on contrast enhancement in radiological imaging. Australas Phys Eng Sci Med 34:243–249
8. Huang X, El-Sayed MA (2010) Gold nanoparticles: Optical properties and implementations in cancer diagnosis and photothermal therapy. J Adv Res 1:13–28
9. Sahare PD, Ranju R, Numan S, Lochab SP (2007) K3Na(SO4)2: Eu nanoparticles for high dose of ionizing radiation. J Phys D Appl Phys 40:759
10. Popov A (2009) Sun protection using nanoparticles. SPIE Newsroom 24:1–2
11. Chen S-S, Chen H-C, Wang W-C, Lee C-Y, Lin IN, Guo J, Chang C-L (2013) Effects of high energy Au-ion irradiation on the microstructure of diamond films. J Appl Phys 113:113704–113710
12. Steinhart M (2004) Introduction to Nanotechnology. Angew Chem Int Ed 43:2196–2197
13. Botelho MZ, Künzel R, Okuno E, Levenhagen RS, Basegio T, Bergmann CP (2011) X-ray transmission through nanostructured and microstructured CuO materials. Appl Radiat Isot 69:527–530
14. Lablogic (2009) In: Lablogic Systems Limited (ed) Lablogic, Sheffield, United Kingdom
15. Daren S (2004) POLYMICRO Newsletter
16. Wardray. Wardray Premise Ltd, Surrey, United Kingdom, 2005–2011
17. Faccini M, Vaquero C, Amantia D (2012) Development of protective clothing against nanoparticle based on electrospun nanofibers. J Nanomater 2012:1–9
18. Künzel R, Okuno E (2012) Effects of the particle sizes and concentrations on the X-ray absorption by CuO compounds. Appl Radiat Isot 70:781–784
19. Noor Azman NZ, Siddiqui SA, Hart R, Low IM (2013) Effect of particle size, filler loadings and x-ray tube voltage on the transmitted x-ray transmission in tungsten oxide-epoxy composites. Appl Radiat Isot 71:62–67
20. Noor Azman NZ, Siddiqui SA, Low IM (2013) Characterisation of micro-sized and nano-sized tungsten oxide-epoxy composites for radiation shielding of diagnostic X-rays. Mater Sci Eng C 33:4952–4957
21. Park JJ (2013) Common spatial patterns based on generalized norms. Trans Electr Electron Mater 14:39–42
22. Moloney AC, Kausch HH, Kaiser T, Beer HR (1987) Review determining the strength and toughness of particulate filled epoxide resins. J Mater Sci 22:381–393

Chapter 7
Synthesis and Characterization of Ion-Implanted Epoxy Composites for X-Ray Shielding

Abstract The epoxy samples were implanted with heavy ions such as tungsten (W), gold (Au) and lead (Pb) to investigate the attenuation characteristics of these composites. Near-surface composition depth profiling of ion-implanted epoxy systems was studied using Rutherford Backscattering Spectroscopy (RBS). The effect of implanted ions on the X-ray attenuation was studied with a general diagnostic X-ray machine with X-ray tube voltages from 40 to 100 kV at constant exposure 10 mAs. Results show that the threshold of implanted ions above which X-ray mass attenuation coefficient, μ_m of the ion-implanted epoxy composite is distinguishably higher than the μ_m of the pure epoxy sample is different for W, Au and Pb.

7.1 Introduction

X-ray shielding requirements have become more stringent as standards for exposure of personnel and general public have been re-assessed. X-rays technologists practice the ALARA principle (as low-as-reasonably-achievable) dose when dealing with harmful ionizing radiation in order to continuously minimize the dose received by personnel and general public [1–5]. Moreover, the application of polymers in X-ray shielding technology is increasing steadily. This is due to a number of advantages such as the choice of fillers into the polymer matrix, the improved dispersion of fillers which enable the formation of mechanically stable hard coating materials and the possibility to modify both chemical composition and the related physical properties of polymers by easy-to-control fabrication parameters [6–11]. In addition, other surface modification tools such as ion implantation has also become increasingly used due to the ease and readability to process some parameters during the irradiation such as the choice of ions, the ion fluence, the depth of ion implantation, etc., which can further improve the X-ray absorption capacity of shielding materials, including polymers [7, 9, 12–14]. The main advantage of ion-implantation technology is the capability of accurately controlling the number of implanted dopant atoms and the dopant's depth distribution profile [15]. In addition, the ion-implantation is well established, and well understood technology as shown in applications for modifying the surface properties of metals, semiconductors and ceramics. More recently, the ion

© Springer Nature Singapore Pte Ltd. 2020

I. M. Low and N. Z. Noor Azman, *Polymer Composites and Nanocomposites for X-Rays Shielding*, Composites Science and Technology,
https://doi.org/10.1007/978-981-13-9810-0_7

implantation technology has been applied to the surface modification of polymers to enhance their mechanical and electrical properties without changing the bulk properties [10, 11, 16–19]. Promising results on ion-implanted ultra high molecular weight polyethylene (UHMWPE) have been shown by Chen et al. where improved hardness and Young's modulus could be obtained through nitrogen ion-implantation [14]. In addition, an epoxy system is a thermoset polymer which is generally stronger and better suited to higher temperatures than thermoplastics so it can withstand the high energetic ion during the implantation process [20]. Hence, the purpose of the present study is to synthesize and characterize the X-ray attenuation property, microstructure and near-surface composition of epoxy composites which have been implanted with heavy ions such as tungsten (W), gold (Au) and lead (Pb).

7.2 Results and Discussion

7.2.1 Rutherford Backscattering Spectroscopy (RBS)

The RBS results in Fig. 7.1 shows the yield versus channel number for samples B1, B3 and B5 implanted with W, Au and Pb, respectively. The list of samples with the different amount of implanted ions is shown in Table 7.1. These results confirm that a higher nominal dose resulted in a higher implanted concentration in the samples. For example, for Au-implanted sample B3, a maximum Au concentration of 0.13 at.% has been implanted in epoxy down to a depth of about 600 mono layers (ML) and it

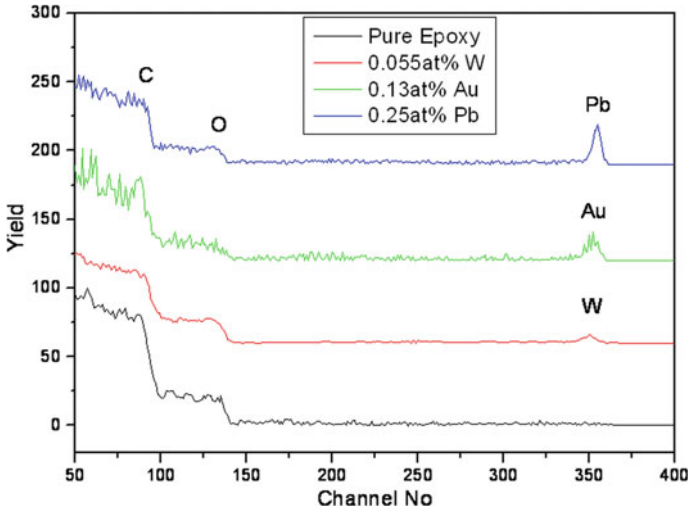

Fig. 7.1 RBS result for pure epoxy sample and implanted samples B1 (0.055 at.% W), B3 (0.13 at.% Au) and B5 (0.25 at.% Pb) [21]

Table 7.1 List of samples prepared with different implanted ions, average charge and RBS concentration of implanted ion

Sample ID	Implanted ion	Average charge	RBS concentration (at.%)
B1	W	+3.07	0.055
B2	W		0.115
B3	Au	+1.99	0.130
B4	Au		0.230
B5	Pb	+1.66	0.250
B6	Pb		0.402

drops to 0.06 at.% for the next 800 ML. For sample B4 a maximum Au concentration of 0.23 at.% has been implanted in epoxy down to a depth of about 700 ML and then it drops to about 0.08 at.% for the next 900 ML. This small difference in the implantation depth of Au in epoxy is attributed to the small differences in the local density of the hand-made epoxy polymer. A similar depth-profile RBS results was obtained for samples implanted with W and Pb.

7.2.2 X-Ray Mass Attenuation Coefficients

Figure 7.2 shows the mass attenuation coefficient, μ_m as a function of X-ray tube voltage for pure epoxy sample and for samples implanted with all three ions at various

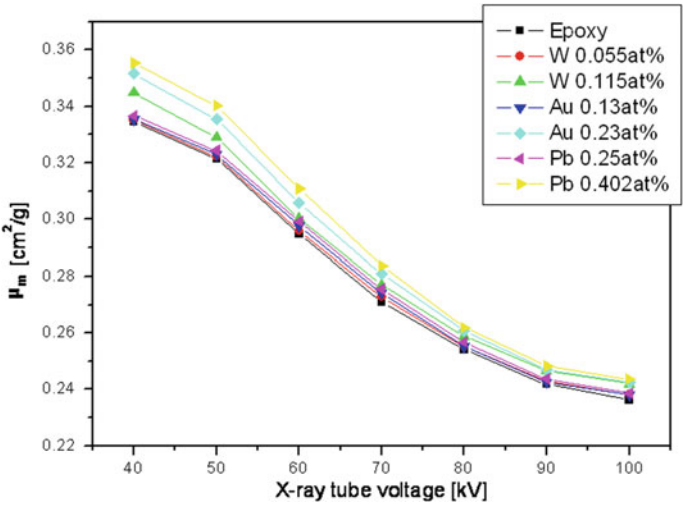

Fig. 7.2 Comparison of μ_m versus X-ray tube voltage for pure epoxy sample and all implanted samples [21]

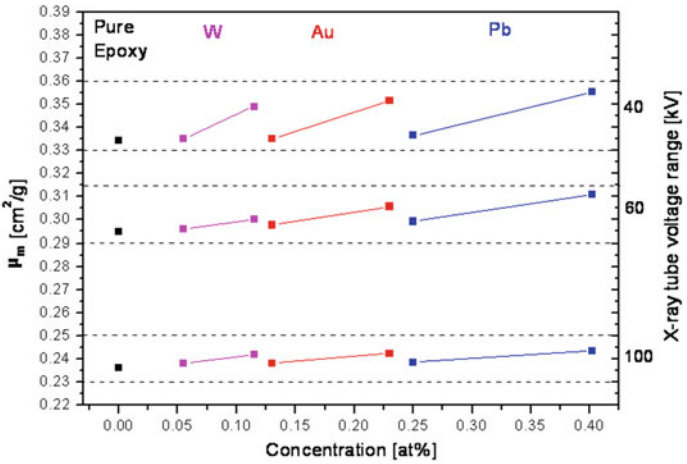

Fig. 7.3 Variation of μ_m with concentration of implanted ion, the type of implanted ion and the excitation energy of the X-ray tube [21]

concentrations, as determined by RBS. The results illustrate the typical decrease of μ_m with the increase of X-ray tube excitation voltage, due to a higher energy bremsstrahlung. In addition, a small increase of μ_m is noticed with the change of the implanted elements (W, Au and Pb). For small concentrations of implanted elements, the variation of μ_m with the X-ray tube voltage is similar with the result of μ_m for pure epoxy. However, for higher concentration of implanted elements, there is a noticeable increase of μ_m above the μ_m of pure epoxy, at each X-ray tube voltage, but this increase is higher at lower excitation voltages (energies). This is better illustrated in Fig. 7.3, where we capture the variation of μ_m with concentration of implanted ion, the type of implanted ion and the excitation energy of the X-ray tube. In addition, with the decreasing of μ_m with the increased of X-ray energy, we note the increase of μ_m with the concentration of implanted element and with type of implanted element. For the same energy of X-rays, the heavier the implanted ion or in other word the higher the atomic number of implanted ion, the higher is the value of μ_m. These were due to the photoelectric interaction that dominates in the low X-ray energy range and high atomic number of absorbing material. The probability of the photoelectric interaction is approximately dependent on Z^3/E^3 where Z is atomic number of the absorbing material (implanted ions) and E is the photon energy [22].

Figure 7.3 also shows that for the same excitation voltage, the increase of μ_m is more effective and that small additions of W afford a reasonable increase. For example (see Table 7.1) for comparable concentrations of 0.115 at.% W (sample B2) and 0.13 at.% Au (sample B3), the W appears to be more effective in increasing the μ_m which is contrary to what we expect since the atomic number of W is lower than the atomic number of Au. A possible explanation could be that at these concentrations, Au and Pb is agglomerating to a higher degree than W, but this is yet to be verified by cross section TEM. However, in terms of the relative increase in the concentration of

Table 7.2 Relative increase of μ_m with the excitation of the X-ray tube for a relative increase in the concentration of implanted ions of: W = 109.1%; Au = 76.9% and Pb = 60.8%

X-ray tube excitation voltage (kV)	W (%)	Au (%)	Pb (%)
40	4.18	4.95	5.55
60	1.45	2.69	3.01
100	1.64	1.59	2.09

implanted ions, the increase of μ_m is higher for Pb, as shown in Table 7.2. Table 7.2 also shows that within the range used for the excitation voltage of the X-ray tube, the doping threshold where μ_m of the composite starts to be larger than the μ_m of the pure epoxy is around 0.1 at.% for W, 0.2 at.% for Au and 0.25 at.% for Pb.

7.3 Conclusions

The ion-implantation technique has been successfully used to implant epoxy resin with W, Au and Pb at various concentrations, and the X-ray mass attenuation coefficient of the composite has been measured in a range of 40–100 kV of the excitation voltage for the X-ray tube. It has been shown that the threshold of implanted ions above which μ_m of the ion-implanted epoxy composite is distinguishably higher than the m of the pure epoxy is different for W, Au and Pb. The practical concentrations of W, Au and Pb in epoxy composite which could provide good X-ray attenuation properties and could be considered as candidates for effective X-ray shielding in diagnostic radiology is higher than the concentrations used in this report, and further work is considered.

Acknowledgements The work on ion-implantation and ion-beam analysis was conducted at the Australian Nuclear Science and Technology Organisation with financial support from AINSE under grant AINGRA 11-135.

References

1. Okunade AA (2002) Comparison of lead attenuation and lead hardening equivalence of materials used in respect of diagnostic X-ray shielding. Appl Radiat Isot 57:819–824
2. Okunade AA (2004) Numerical models for the determination of primary structural barriers for diagnostic X-ray facilities. Med Phys 31:513–520
3. Archer BR (2005) Recent history of the shielding of medical X-ray imaging facilities. Health Phys 88:579–586
4. Dixon RL, Simpkin DJ (1998) Primary shielding barriers for diagnostic X-ray facilities: a new model. Health Phys 74:181–189
5. Hessenbruch A (2002) A brief history of X-rays. Endeavour 26:137–141
6. Wu Y, Zhang T, Zhang H, Zhang X, Deng Z, Zhou G (2000) Electrical properties of polymer modified by metal ion implantation. Nucl Instrum Methods Phys Res, Sect B 169:89–93

7. Dworecki K, Drabik M, Hasegawa T, Wąsik S (2004) Modification of polymer membranes by ion implantation. Nucl Instrum Methods Phys Res, Sect B 225:483–488
8. Hubler GK (1981) Use of ion beam analysis in metal modification by means of ion implantation. Nucl Instrum Methods Phys Res 191:101–113
9. Soares MRF, Alegaonkar P, Behar M, Fink D, Muller M (2004) $^{6}Li^{+}$ ion implantation into polystyrene. Nucl Instrum Methods Phys Res, Sect B 218:300–307
10. Lee EH, Rao GR, Lewis MB, Mansur LK (1993) Ion beam application for improved polymer surface properties. Nucl Instrum Methods Phys Res, Sect B 74:326–330
11. Yuguang W, Tonghe Z, Huixing Z, Xiaoji Z, Zhiwei D (2000) Polymer modification by MEVVA source deposited and ion implantation. Surf Coat Technol 131:520–524
12. Lopatin CM, Alford TL, Pizziconi VB, Kuan M, Laursen T (1998) Ion-beam densification of hydroxyapatite thin films. Nucl Instrum Methods Phys Res, Sect B 145:522–531
13. Anders A (1997) Ion charge state distributions of vacuum arc plasmas: The origin of species. Phys Rev E 55:969
14. Chen JS, Lau SP, Sun Z, Tay BK, Yu GQ, Zhu FY, Zhu DZ, Xu HJ (2001) Structural and mechanical properties of nitrogen ion implanted ultra high molecular weight polyethylene. Surf Coat Technol 138:33–38
15. http://www.ece.gatech.edu/research/labs/vc/theory/ionimplant.html#depth, 22 June 2010
16. Kozlov EV, Ryabchikov AI, Sharkeev YP, Stepanov IB, Fortuna SV, Sivin DO, Kurzina IA, Prokopova TS, Mel'nik IA (2002) Formation of intermetallic layers at high intensity ion implantation. Surf Coat Technol 158–159:343–348
17. Evans PJ, Hyvarinen J, Samandi M (1995) Surface modification of austenitic stainless steel by titanium ion implantation. Surf Coat Technol 71:151–158
18. Ashworth V, Grant WA, Procter RPM, Wright EJ (1978) The effect of ion implantation on the corrosion behavior of pure iron-IV. Lead ion implantation. Corros Sci 18:681–685
19. Wang C, Tao YX (1985) The influence of boron ion-implantation on silica and lead glasses. J Non-Cryst Solids 71:397–402
20. Archos LLC. http://www.archos-llc.com/Material_Guide_2.html, 6 Oct 2011
21. Noor Azman NZ, Siddiqui SA, Ionescu M, Low IM (2012) Synthesis and characterisation of ion-implanted epoxy composites for X-ray shielding. Nucl Instrum Methods Phys Res, Sect B 287:120–123
22. Sprawls P (1993) The physical principles of medical imaging, 2nd edn. Aspen Publishers, Gaithersburg, MD

Chapter 8
A Comparative Study of X-Ray Shielding Capability in Ion-Implanted Acrylic and Glass

Abstract Samples of acrylic and glass were implanted with tungsten (W) and lead (Pb) to investigate their X-ray attenuation characteristics. The near-surface composition depth profiles of ion-implanted acrylic and glass samples were studied using ion-beam analysis (Rutherford backscattering spectroscopy—RBS). The effect of implanted ions on the X-ray attenuation ability was studied using a conventional laboratory X-ray machine with X-ray tube voltages ranging from 40 to 100 kV at constant exposure 10 mAs. The results were compared with previous work on ion-implanted epoxy. As predicted, the RBS results and X-ray attenuation for both ion-implanted acrylic and glass increase with the type of implanted ions when compared to the controls. However, since the glass is denser than epoxy or acrylic, it has provided the higher X-ray attenuation property and higher RBS ion concentration implanted with a shorter range of the ion depth profile when compared to epoxy and acrylic. A prolonged time is necessary for implanting acrylic with a very high nominal dose to minimize a high possibility of acrylic to melt during the process.

8.1 Introduction

Hitherto, the application of ion implantation has become increasingly used due to the capability of accurate control on the number of implanted ions and the implanted depth distribution profile. This enables scientists to further improve the X-ray absorption capacity of shielding materials such as glass and polymers [1–11]. For example, a recent research by Rodríguez et al. [12] has shown that ion implantation is an effective technology for implanting elements into polymers for surface modification to improve their mechanical properties such as hardness and elastic modulus. In addition, promising material comprising Cu nanoparticles in a ZnO matrix for exhibiting the phenomenon of self-defocusing and possessing a high nonlinear absorption coefficient for the usage as an active light intensity limiter in the visible spectral range was successfully obtained by the ion implantation technique by Stepanov et al. [13]. Furthermore, our previous work on epoxy implanted with lead, tungsten and gold ions showed a higher X-ray attenuation of when compared to pure epoxy [14].

© Springer Nature Singapore Pte Ltd. 2020

I. M. Low and N. Z. Noor Azman, *Polymer Composites and Nanocomposites for X-Rays Shielding*, Composites Science and Technology,
https://doi.org/10.1007/978-981-13-9810-0_8

Glass is one example of materials used in shielding of ionizing radiations, especially for X-rays and gamma-rays, but it is heavy, expensive and very brittle. So, it is not surprising that the application of polymers in X-ray shielding technology is increasing steadily. This is due to a number of advantages that glass could not meet because of their unique properties, such as low manufacturing cost and rugged shatter-resistant material [3, 9]. But due to its high density as compared to polymer, glass is still in use for ionizing radiation shielding purposes since it can provide higher attenuation than polymer of the same thickness [15].

The aim of the present work was to synthesize, characterize and compare the X-ray attenuation properties and near-surface composition profiles of acrylic and glass implanted with tungsten and lead for X-ray shielding purposes. These results were also compared with our previous work done on ion-implanted epoxy [14].

8.2 Results and Discussion

The list of samples implanted with different ions is shown in Table 8.1. Figure 8.1 shows the RBS results plotted as the yield versus channel number for acrylic and glass samples (B1–C3) implanted with W and Pb.

The RBS composition of acrylic and glass was used to calculate the range of implanted ions, using Monte Carlo simulation (SRIM 2010). The range of 122.8 keV W in acrylic is 84 nm and in glass is 48 nm, and the range of 66.4 keV Pb in acrylic is 56 nm and in glass is 32 nm. These values are similar with the depth distribution calculated from RBS results and shown in Fig. 8.2, where for comparison reasons we also show the results of depth distribution of W and Pb in epoxy.

Table 8.1 List of polymer composites and glass prepared with different implanted ions and their concentrations

Sample ID	Matrix	Nominal dose [ions/cm^2]	Implanted ion	RBS ion concentration [at.%]
A1	Epoxy	7.0×10^{14}	W	0.055
A2		7.0×10^{14}	Pb	0.250
A3		1.4×10^{15}	Pb	0.390
B1	Acrylic	7.0×10^{14}	W	0.050
B2		7.0×10^{14}	Pb	0.200
B3		1.4×10^{15}	Pb	0.430
C1	Glass	7.0×10^{14}	W	0.100
C2		7.0×10^{14}	Pb	0.290
C3		1.4×10^{15}	Pb	0.850

For comparison reasons, we included previous results on the epoxy

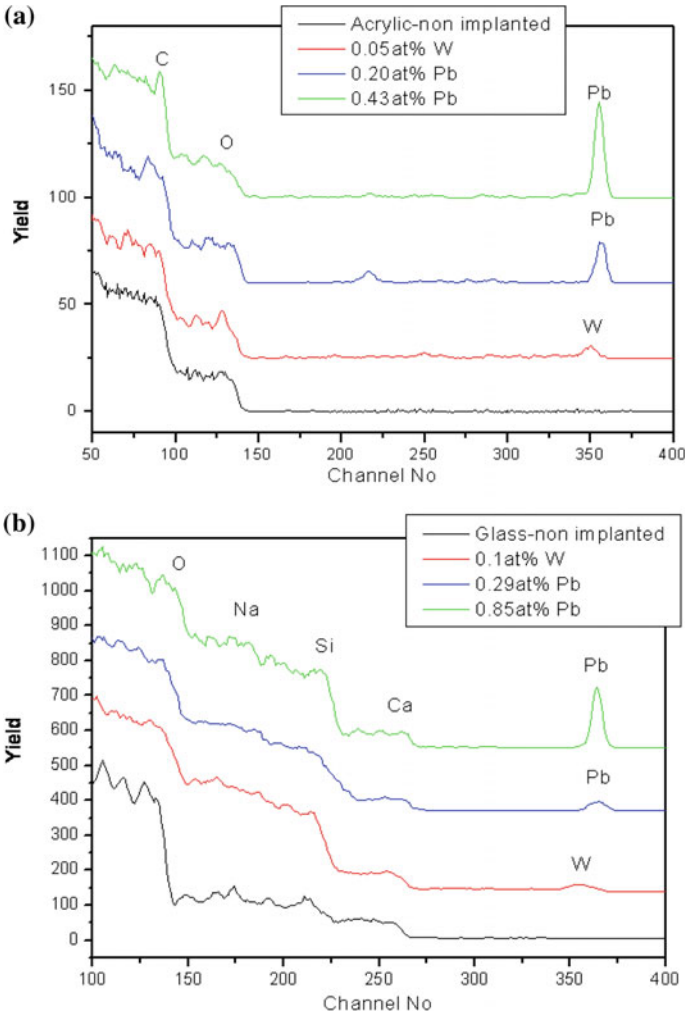

Fig. 8.1 RBS result for **a** acrylic implanted samples B1 (W), B2 and B3 (Pb); and **b** glass implanted samples C1 (W), C2 and C3 (Pb) [16]

The results confirmed that the range of implanted ions is inversely proportional with the atomic number (Z) of implanted ion (Pb = 82, W = 74) and with the density of the matrix. In addition, RBS shows specific variations in range and concentration of implanted ions, which are the result of specific sample matrix inhomogeneity. For example (Fig. 8.2), for W-implanted acrylic (B1), a maximum W concentration of 0.05 at. % has been implanted down to a depth of about 1000 mono layers (ML) and then it drops to about 0.025 at.% for the next 200 ML. For W-implanted glass (C1), a maximum W concentration of 0.1 at.% has been implanted down to a depth of about 1000 ML, and as the density of glass is higher than the density of acrylic,

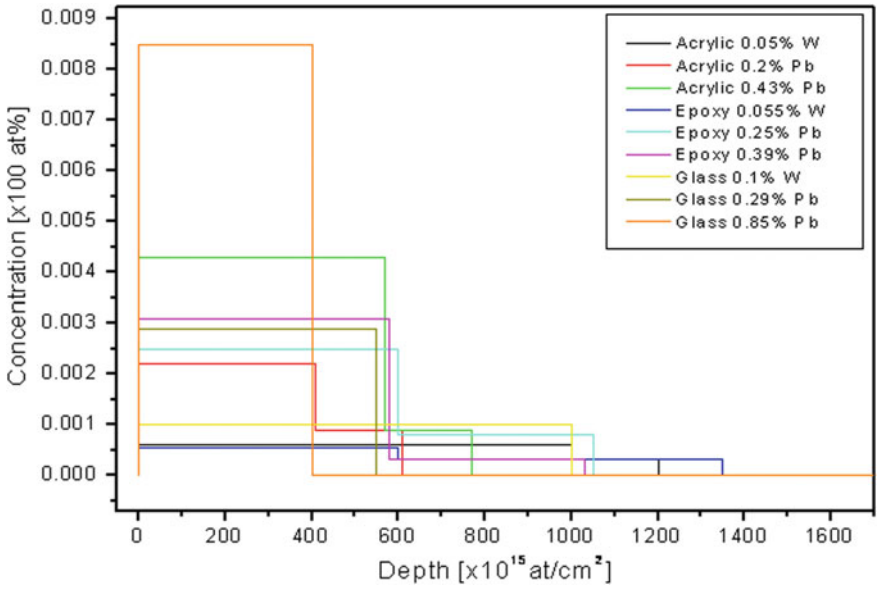

Fig. 8.2 RBS depth profile of implanted elements, for samples listed in Table 8.1. For comparison reasons we included the previous results on epoxy [16]

one would expect the W implantation depth to be smaller than the W implantation depth in acrylic, but this is not the case due to local inhomogeneities. Even for the same sample matrix (acrylic), the same ion may have a different depth profile, and this again, is attributed to the differences in the local density of the acrylic itself. Similar depth profile RBS results were also obtained for composite samples of glass as a matrix base and also our previously epoxy samples [14].

In Table 8.1, the differences between the measured RBS concentration of W and Pb ion at the same nominal implantation dose are explained by two factors: the different sputtering properties of the two ions, and the uncertainty in the dose measurement between different implantation runs. The glass is a denser (2.45 g/cm^3) matrix when compared to the acrylic or epoxy and contains heavier elements (Si, Na) hence it has a higher stopping power to slow down the ions as they travel within it. Further, a denser material has a lower projected range/depth profile (because ions have a greater chance of colliding with the atoms within the material especially near the surface). In contrast, epoxy and acrylic have nearly the same density (average 1.15 g/cm^3) and hence they do not show significant differences in the RBS concentration between them. These statements are supported by the results in Fig. 8.2 since Pb-implanted glass (C3) has a shorter depth profile as compared to Pb-implanted epoxy (A3) and Pb-implanted acrylic (B3) of the same nominal dose of Pb 1.4×10^{15} ions/cm^2.

Besides, there is a huge difference in ion concentration between sample A3 or B3 with C3 when we double the nominal dose (1.4×10^{15} ions/cm^2) as shown in Table 8.1. After the ions entering a matrix, the energy that an ion loses is converted to

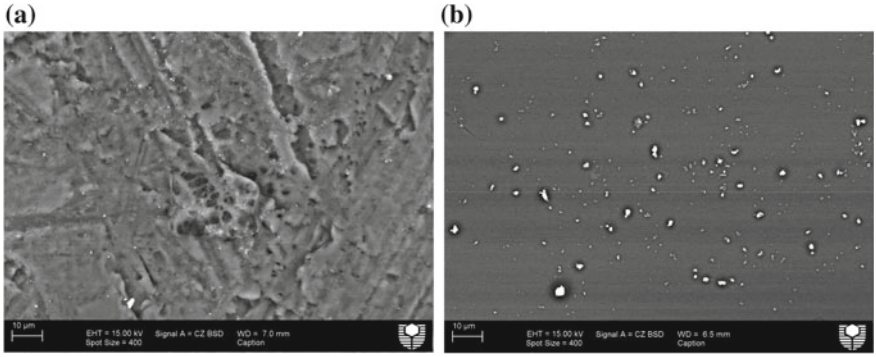

Fig. 8.3 SEM image of the surface of **a** acrylic implanted with Pb (sample B3) showing the region being melted during the higher nominal dose of implantation; and **b** glass implanted with Pb (sample C3) [16]

heat when slowing down within the material as the atoms dissipate the kinetic energy in a series of collisions. Moreover, the melting point of acrylic or epoxy is ~160 °C while for the glass is >1000 °C. So there is a high possibility of acrylic being altered (Fig. 8.3) by the energetic ions (with average velocity around 2.0×10^5 m/s) when they bombard the surface and cause bond breaking along the ion tracks, some of the matrix atoms (H, O) could be lost and escape by diffusion. These altered regions of the polymer may play an additional role in absorbing the X-ray, but this is yet to be tested in a future experiment.

Figure 8.4 shows the linear attenuation coefficient, μ as a function of X-ray tube voltage for all samples listed in Table 8.1, and for non-implanted samples of each material used for ion implantation. The result of μ for W—implanted acrylic and glass with the nominal dose of 7.0×10^{14} ions/cm^2 is nearly the same with the result of μ for non-implanted material, at each X-ray tube voltage. Meanwhile, with the decreasing of μ with the increasing of X-ray tube voltage we noticed that μ is also increasing with the atomic number of implanted elements. For the same X-ray tube voltage, the heavier the implanted ion or in other words the higher the atomic number of implanted ion, the higher is the value of μ and can be differentiated from the μ for pure matrix composite especially at lower X-ray tube voltage (40–70 kV). This showed that the attenuation of the primary X-ray beam by the absorbing material is highly dependent on the atomic number of the absorbing material itself. Notice that the atoms of higher atomic number absorbing material present larger targets for the radiation to strike and hence the chances of interactions via the photoelectric interaction are relatively high. Hence, the attenuation should therefore be relatively large. Meanwhile, in the case of lower atomic number absorbing material however the individual atoms are smaller and hence the chances of interactions are reduced. In other words, the radiation has a greater probability of being transmitted through the absorbing material and the attenuation is consequently lower than in the high atomic number case. The photoelectric interaction usually dominates in the lower X-ray energy range and also for the high atomic number of absorbing material

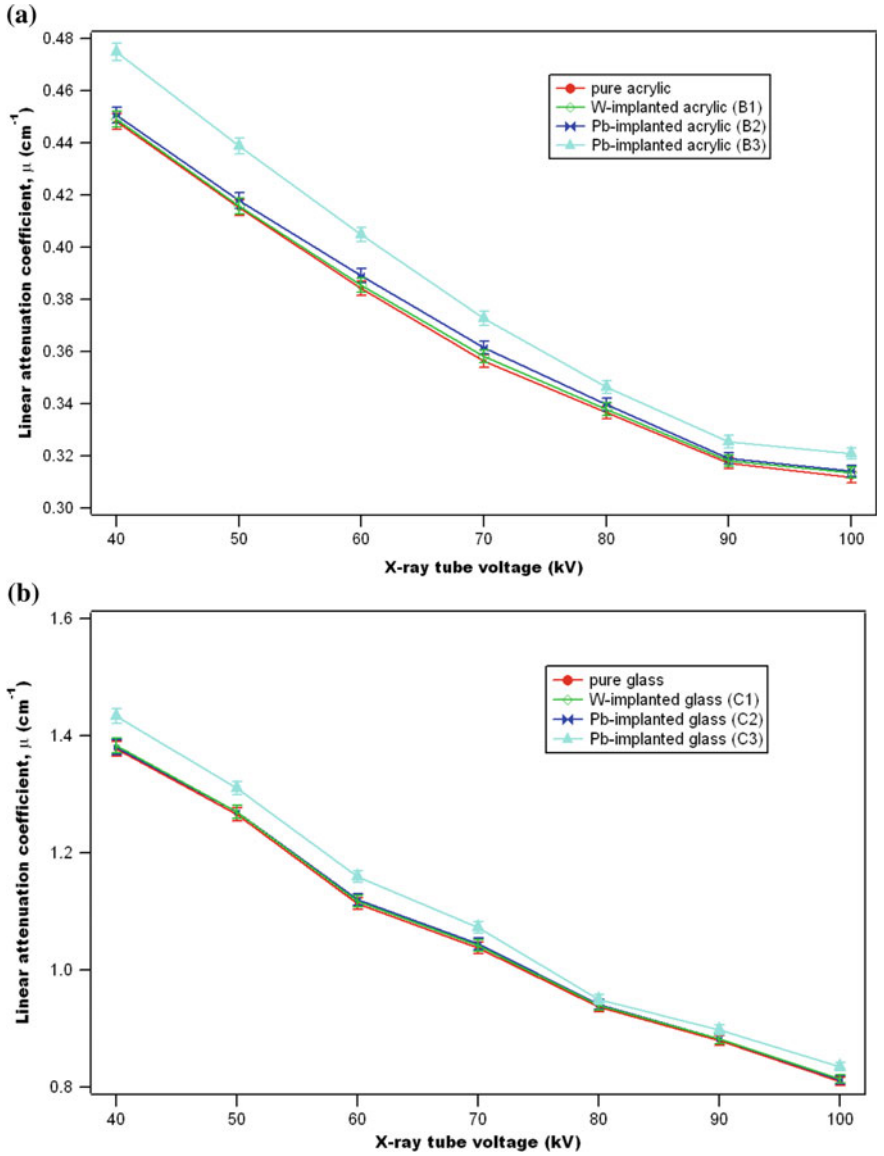

Fig. 8.4 Comparison of μ versus X-ray tube voltage for **a** pure acrylic and acrylic implanted samples B1 (W), B2 and B3 (Pb); and **b** pure glass and glass implanted samples C1 (W), C2 and C3 (Pb) [16]

(implanted ions). The probability for the photoelectric interaction to occur is dependent on Z^3/E^3 where Z is the atomic number of the absorbing material, and E is the photon (X-ray/gamma-ray) energy [17]. Additionally, the ion-implanted glass shows the highest attenuation compared to acrylic/epoxy since it is denser and has the highest RBS ion concentration of the same ion (Fig. 8.5) because more primary X-ray beam being attenuated by a denser absorbing material than a lower density absorbing material since the chances of an interaction between the radiation and the atoms of the absorbing material are relatively higher. In most cases, high density absorbing materials are more effective than low density alternatives for blocking or reducing the intensity of radiation. However, low density absorbing materials can compensate for the disparity with increased thickness, which is as significant as density in shielding applications.

From the above analyses, glass is still the best candidate for implanting with high RBS ion concentration and thus able to attenuate more X-rays as compared to pure acrylic/epoxy but it is fragile and easy to break; thus we need to handle it carefully for using as X-ray shielding. In contrast, even though acrylic is inferior in terms of density, melting point and seems not an ideal applicant but an implanted acrylic can still be chosen as a candidate for X-ray shielding because it is tougher and lighter as compared to glass but prolonged time is needed when implanted it with a high nominal dose to prevent it to melt during the implantation process. Besides, it also can provide similar X-ray attenuation like glass with increased thickness, which is as significant as density in shielding applications.

8.3 Conclusions

Ion-implantation has been successfully used to modify the near-surface of acrylic and glass with W and Pb ions to improve X-ray attenuation for X-ray shielding for diagnostic radiology purposes. The X-ray attenuation is higher for the composite with the denser sample matrix and the composite having the higher RBS ion concentration. However, the number of implanted doses will need to be significantly increased so that this approach can be feasible for designing new shielding materials for the X-ray technologists. Even though glass provided the best results for both RBS ion concentration and X-ray attenuation, its usage as X-ray shielding needs extra care since it is easy to break. In contrast, implanted acrylic can be a good candidate for X-ray shielding but much time is needed when implanted acrylic with a very high nominal dose since it has a low melting point and by increasing its thickness.

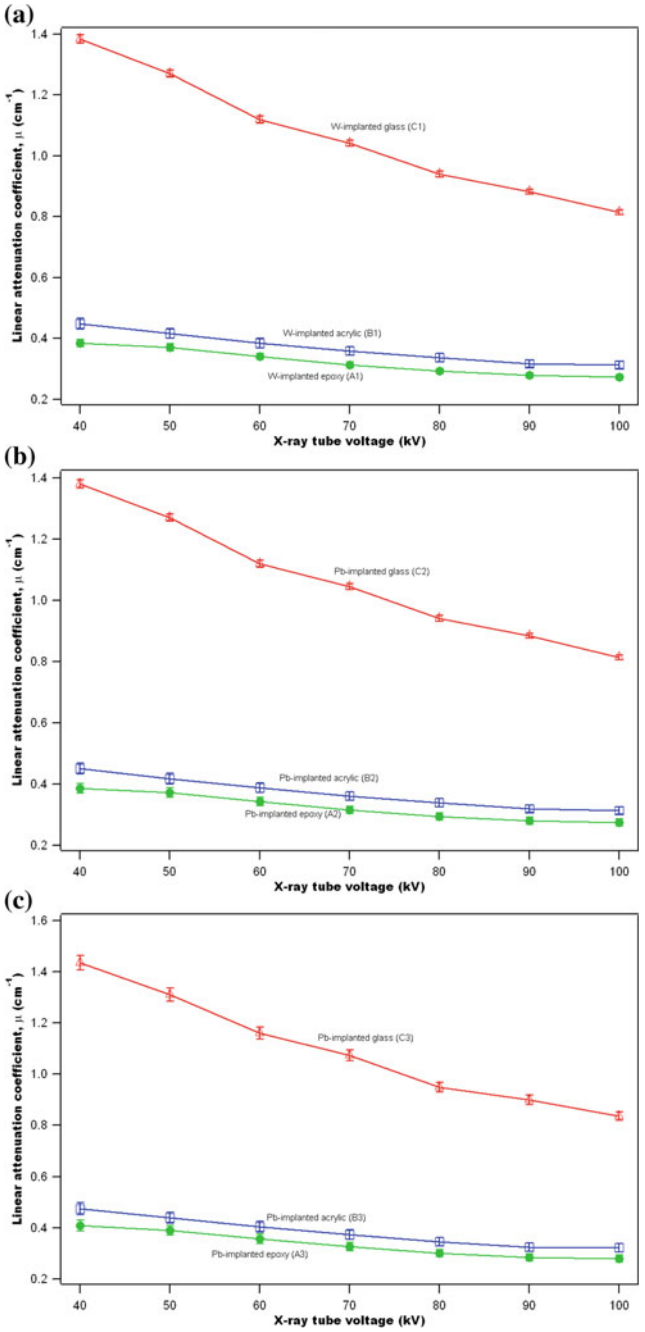

Fig. 8.5 Comparison of μ versus X-ray tube voltage for **a** W-implanted epoxy (A1), acrylic (B1) and glass (C1); **b** Pb-implanted epoxy (A2), acrylic (B2) and glass (C2); and (c) Pb-implanted epoxy (A3), acrylic (B3) and glass (C3) [16]

Acknowledgements The work on ion-implantation and ion-beam analysis was conducted at the Australian Nuclear Science and Technology Organization with financial support from AINSE (AINGRA 11-135).

References

1. Anders A (1997) Ion charge state distributions of vacuum arc plasmas: the origin of species. Phys Rev E 55:969–981
2. Chen JS, Lau SP, Sun Z, Tay BK, Yu GQ, Zhu FY, Zhu DZ, Xu HJ (2001) Structural and mechanical properties of nitrogen ion implanted ultra high molecular weight polyethylene. Surf Coat Technol 138:33–38
3. Dworecki K, Drabik M, Hasegawa T, Wąsik S (2004) Modification of polymer membranes by ion implantation. Nucl Instrum Methods Phys Res, Sect B 225:483–488
4. Evans PJ, Hyvarinen J, Samandi M (1995) Surface modification of austenitic stainless steel by titanium ion implantation. Surf Coat Technol 71:151–158
5. Hubler GK (1981) Use of ion beam analysis in metal modification by means of ion implantation. Nucl Instrum Methods Phys Res 191:101–113
6. Kozlov EV, Ryabchikov AI, Sharkeev YP, Stepanov IB, Fortuna SV, Sivin DO, Kurzina IA, Prokopova TS, Mel'nik IA (2002) Formation of intermetallic layers at high intensity ion implantation. Surf Coat Technol 158–159:343–348
7. Lee EH, Rao GR, Lewis MB, Mansur LK (1993) Ion beam application for improved polymer surface properties. Nucl Instrum Methods Phys Res, Sect B 74:326–330
8. Lopatin CM, Alford TL, Pizziconi VB, Kuan M, Laursen T (1998) Ion-beam densification of hydroxyapatite thin films. Nucl Instrum Methods Phys Res, Sect B 145:522–531
9. Soares MRF, Alegaonkar P, Behar M, Fink D, Müller M (2004) $^{6}Li^{+}$ ion implantation into polystyrene. Nucl Instrum Methods Phys Res, Sect B 218:300–307
10. Wu Y, Zhang T, Zhang H, Zhang X, Deng Z, Zhou G (2000) Electrical properties of polymer modified by metal ion implantation. Nucl Instrum Methods Phys Res, Sect B 169:89–93
11. Yuguang W, Tonghe Z, Huixing Z, Xiaoji Z, Zhiwei D (2000) Polymer modification by MEVVA source deposited and ion implantation. Surf Coat Technol 131:520–524
12. Rodríguez RJ, Medrano A, García JA, Fuentes GG, Martínez R, Puertolas JA (2007) Improvement of surface mechanical properties of polymers by helium ion implantation. Surf Coat Technol 201:8146–8149
13. Stepanov AL, Khaibullin RI, Can N, Ganeev RA, Ryasnyansky AI, Buchal C, Uysal S (2004) Application of ion implantation for synthesis of copper nanoparticles in a zinc oxide matrix for obtaining new nonlinear optical materials. Tech Phys Lett 30:846–849
14. Noor Azman NZ, Siddiqui SA, Ionescu M, Low IM (2012) Synthesis and characterisation of ion-implanted epoxy composites for X-ray shielding. Nucl Instrum Methods Phys Res, Sect B 287:120–123
15. Chanthima N, Kaekwkhao J, Kedkaew C, Chewpraditkul W, Pokaipisit A, Limsuwan P (2011) Study on interaction of Bi_2O_3, PbO and BaO in silicate glass system at 662 keV for development of gamma-rays shielding materials. Prog Nucl Sci Technol 1:106–109
16. Noor Azman NZ, Siddiqui SA, Ionescu M, Low IM (2013) A comparative study of X-ray shielding capability in ion-implanted acrylic and glass. Radiat Phys Chem 85:102–106
17. Sprawls P (1993) The physical principles of medical imaging, 2nd edn. Aspen Publishers, Gaithersburg, MD

Chapter 9
Characteristics of X-Ray Attenuation in Electrospun Bismuth Oxide/Poly-lactic Acid Nanofibre Mats

Abstract The characteristics of X-ray transmission in electrospun nano(n)- and micro(m)-Bi_2O_3/poly lactic acid (PLA) nanofibre mats with different Bi_2O_3 loadings were compared using mammography (22–49 kV) and X-ray absorption spectroscopy (XAS) (7–20 keV). Results indicate that X-ray transmissions by electrospun m-Bi_2O_3/PLA nanofibre mats are distinctly higher than those of n-Bi_2O_3/PLA nanofibre mats at all energies investigated. In addition, with increasing the filler loading (n-Bi_2O_3 or m-Bi_2O_3), the porosity of electrospun Bi_2O_3/PLA nanofibre mats decreased thus decreasing the X-ray transmission except for the nanofibre mat containing 38 wt% of Bi_2O_3 (the highest loading in the present study). The latter showed higher porosity with some beads formed thus resulting in a sudden increase in X-ray transmission.

9.1 Introduction

Nanoparticles, i.e. nanometric sized particles, have attracted much attention amongst researchers in different fields of physics, chemistry, material science, medicine, and biology, because of their unique and often superior electronic, magnetic, optical, mechanical, physical and chemical properties [1–7]. For example, in the medical field, nanoparticles have been widely used in diagnosis, tissue engineering and also as drug delivery devices [8]. Gold nanoparticles are one of the most useful nanoparticles in industry and medicine [3]. For instance, in the medical field, gold nanoparticles show significant improvement in the treatment of cancers by enhancing the sensitivity of radiation from a radiotherapy unit with minimal adverse effects on surrounding normal tissues [1, 2].

Additionally, this size-effect has also become one of the virtues in designing materials for shielding of ionizing radiations. Some X-ray technologists believe that this effect will improve the X-ray attenuation ability of the composite since nano-sized fillers are able to be dispersed more uniformly within the matrix with fewer agglomerations as compared to micro-sized fillers [9, 10]. The latest work done by Buyuk et al. [11] proved that decreasing the titanium diboride particle size in the titanium diboride reinforced boron carbide-silicon carbide composites causes

© Springer Nature Singapore Pte Ltd. 2020

I. M. Low and N. Z. Noor Azman, *Polymer Composites and Nanocomposites for X-Rays Shielding*, Composites Science and Technology,
https://doi.org/10.1007/978-981-13-9810-0_9

higher linear attenuation coefficient values for the energy of 0.662 MeV emitted by Cs-137 gamma source [11] found that the nanostructured copper oxide (CuO) is more effective in attenuation of lower X-ray beam energy (26 and 30 kV) and no significant variation in X-ray attenuation at higher X-ray beam energy (60 and 102 kV). Künzel and Okuno [12] also provided similar results, which show that the X-ray absorption is higher for a nanostructured CuO compound compared to the microstructured counterpart for low energy X-ray beams (25 and 30 kV) for all CuO concentrations incorporated into polymeric resins.

Electrospinning is a well-established polymer processing technique which has been proven to be a flexible and effective method for fabricating multilayers of microscale (>1 μm) to the nanoscale (<1000 nm) fibres from different types of polymers to be used in a wide range of applications such as in drug delivery, tissue engineering and protective clothing [13–22]. This technique provides many benefits to industry with perhaps the most important one being its versatility and simplicity, which means it is a very time efficient way to fabricate a variety of continuous nanofibrous structures. It is advantageous to use the nanofibre webs in a layered structure together with a suited substrate material such that the final product offers sufficient strength and durability. Besides, the nanofibre layers should be flexible and also have a good adherence to the substrates without being easily broken or delaminated [23–25].

In the present study, due to the simplicity of the technique, it is investigated whether electrospinning can also be used to produce nanofibre mat for the efficient shielding of ionizing radiations. In a recent work on WO_3-filled epoxy composites [25], we investigated the effect of nano-sized and micro-sized filler reinforced epoxy composites by melt-mixing method on the X-ray attenuation in the X-ray tube voltage range of 22–127 kV. Our results showed that nano-sized WO_3 was more effective than micro-sized WO_3 in X-ray attenuation at the low X-ray tube range of 22–35 kV since photoelectric interaction dominates at lower photon (X-ray) energy range and also the number of W particles/gram in the nano-sized WO_3-epoxy composite is higher than that for the micro-sized WO_3-epoxy composite. The size effect was not apparent at the higher X-ray tube voltage range of 40–120 kV. Hence, the objective of our present study is to synthesize new radiation shielding materials using the electrospinning technique with the preparation of well-dispersed Bi_2O_3 of different particle sizes in PLA fibre mat. The effectiveness of electrospun nano-Bi_2O_3/PLA nanofibre mats in radiation protection during diagnostic imaging using low X-ray energies is also reported, with the ultimate goal of offering a new approach to radiation protection, based on nanotechnology and electrospinning.

9.2 Results and Discussion

9.2.1 Thickness Measurement

The t_{ave} of all the electrospun Bi_2O_3/PLA nanofibre mats used in Eq. (2.5) is (0.0300 $\pm$ 0.0002) cm which is the chosen constant average thickness of the sample used for the X-ray transmission comparison. On the other hand, t_{ave} of all Bi_2O_3/PLA thin films is (0.0490 $\pm$ 0.0002) cm.

9.2.2 Porosity Measurement

From Table 9.1, the apparent density ρ of each thin film (the last two columns to the right of the table) of the same filler (Bi_2O_3) category increased by the increment of filler content in the PLA solution. The density found in thin films illustrated that m-Bi_2O_3/PLA thin film gives lower density compared to n-Bi_2O_3/PLA thin film but both of them did not make a great difference compared to the theoretical value. However, the apparent density results of the electrospun Bi_2O_3/PLA nanofibre mat underestimated the theoretical values due to the nanofibres were highly porous, randomly oriented and aligned. As can be seen, the density of the electrospun Bi_2O_3/PLA nanofibre mat increased with the filler loading except for the electrospun Bi_2O_3/PLA nanofibre mat of 38 wt% Bi_2O_3 loading; there is a sudden decreased in the density due to the higher porosity found (Table 9.2) and also the formation of PLA beads.

Porosity is an important parameter when preparing the absorbing material for the X-ray attenuation experiment. As can be seen from Table 9.2, the porosity of both electrospun n-Bi_2O_3/PLA nanofibre mat and electrospun m-Bi_2O_3/PLA nanofibre mat was over 70% probably due to the entangled structure of the randomly-oriented nanofibres, indicating that they were highly porous and thus were not really beneficial for the X-ray attenuation by the electrospun nanofibre mat especially with the filler $\geq$38 wt%. Further increases of filler wt% (>38 wt%) was not performed due to the decrease in the sample's density and increasing of the porosity measured

Table 9.1 Density of electrospun Bi_2O_3-PLA nanofibre mats and Bi_2O_3-PLA thin films

Filler (Bi_2O_3) weight fraction (wt%)	Density (cm^3/g)				
	Theoretical	Electrospun nanofibre mat		Thin films	
		Nano	Micro	Nano	Micro
24	1.56	0.27	0.25	1.54	1.50
28	1.63	0.40	0.39	1.59	1.52
34	1.75	0.49	0.45	1.69	1.64
38	1.84	0.30	0.24	1.77	1.72

Table 9.2 Porosity of electrospun Bi_2O_3-PLA nanofibre mats

Filler (Bi_2O_3) weight fraction (wt%)	Porosity (%)	
	Nano-Bi_2O_3 PLA nanofibre mat	Micro-Bi_2O_3 PLA nanofibre mat
0	88.8	88.8
24	83.0	84.0
28	75.4	76.1
34	72.1	74.3
38	83.6	87.0

which can not give any advantages for future X-ray transmission experiments. The porosity found from the control electrospun PLA nanofibre mat was 88.8%. So, if a further investigation was performed for higher filler wt% (>38 wt%), the electrospun Bi_2O_3/PLA nanofibre mat would probably have similar or even higher porosity than this controlled sample.

9.2.3 X-Ray Transmissions

Figure 9.1 shows the XAS X-ray linear attenuation coefficient (μ) results of elec-

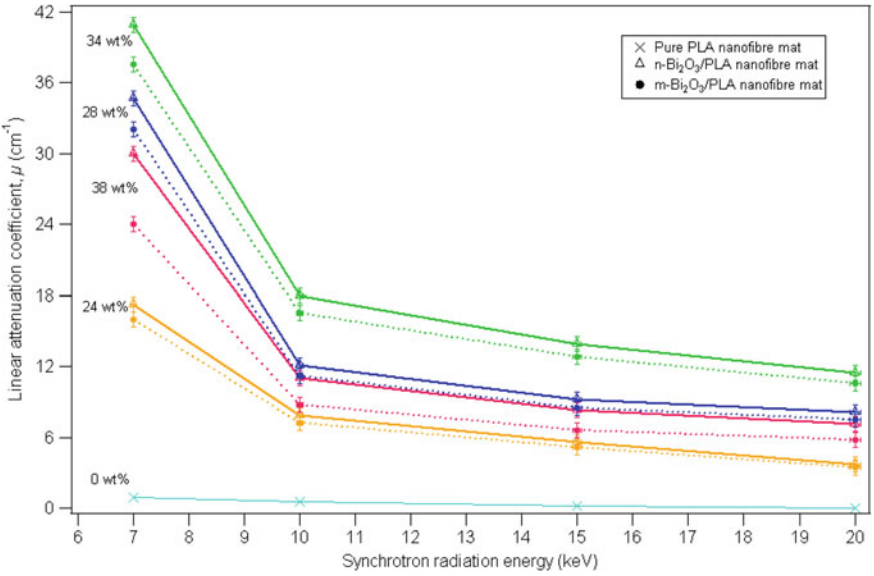

Fig. 9.1 Linear attenuation coefficient as a function of synchrotron radiation energy operated by XAS (7–20 keV) for all Bi_2O_3 loading (0–38 wt%) of the electrospun n-Bi_2O_3/PLA and m-Bi_2O_3/PLA nanofibre mats [28]

trospun nanofibre mats for X-ray energy of 7–20 keV for 0–38 wt% Bi_2O_3 loading. It clearly shows a big difference in T between electrospun n-Bi_2O_3/PLA nanofibre mats and electrospun m-Bi_2O_3/PLA nanofibre mats of the same filler loadings as the X-ray energy increased. Additionally, Fig. 9.2 also shows a distinct difference in μ between electrospun n-Bi_2O_3/PLA nanofibre mats and electrospun m-Bi_2O_3/PLA nanofibre mats at the same filler loadings for the X-ray beams generated by 22–49 kV X-ray tube voltages from the mammography unit. These X-ray tube voltages provided the X-ray effective energy in the range of 15.2–20.8 keV (Fig. 9.3) which were determined using half-value layer (HVL) experiments done by Suk et al. on the mammography unit [26].

As can be seen from both Figs. 9.1 and 9.2, the X-ray μ was reduced with an increase of the filler loading within the PLA matrix for both electrospun n-Bi_2O_3/PLA and m-Bi_2O_3/PLA nanofibre mats except for 38 wt% Bi_2O_3 loading; there is a sudden decrease in X-ray attenuation. These findings support the density and porosity results discussed previously, including the 38 wt% of Bi_2O_3/PLA nanofibre mats which showed low density and high porosity, thus leading to decreased X-ray attenuation. Meanwhile, the comparison of thin-films between m-Bi_2O_3/PLA and n-Bi_2O_3/PLA does not totally support the results found from this study for the electrospun Bi_2O_3/PLA nanofibre mats. As the image in Fig. 9.4 indicate, as the effective X-ray energy increased to >17.4 keV (X-ray tube voltage >35 kV), for the same wt% of Bi_2O_3 filler within this thin film sample, X-ray attenuation for m-Bi_2O_3

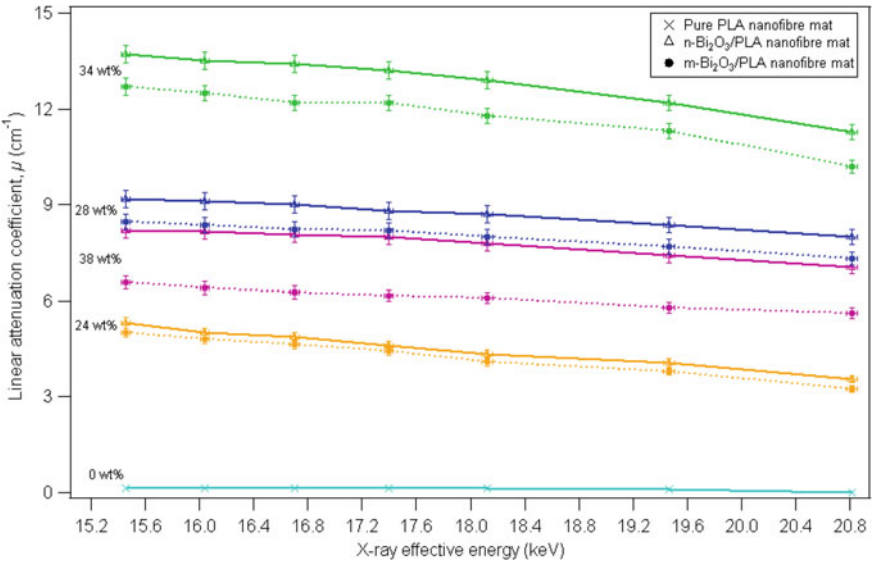

Fig. 9.2 Linear attenuation coefficient as a function of effective energy operated by various X-ray tube voltages of the mammography unit (22–49 kV) for all Bi_2O_3 loading (0–38 wt%) of the electrospun n-Bi_2O_3/PLA and m-Bi_2O_3/PLA nanofibre mats [28]

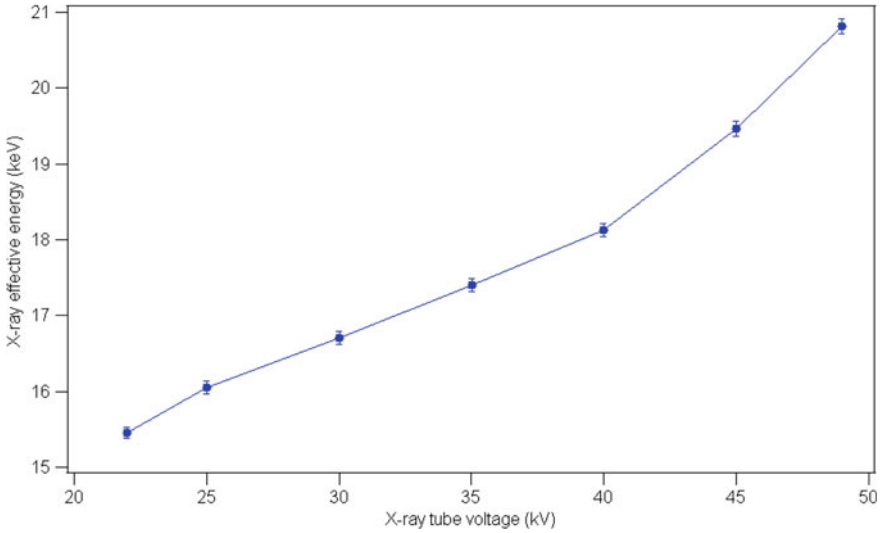

Fig. 9.3 Effective energy as a function of the X-ray tube voltages operated by the mammography unit determined from half-value layer measurements [28]

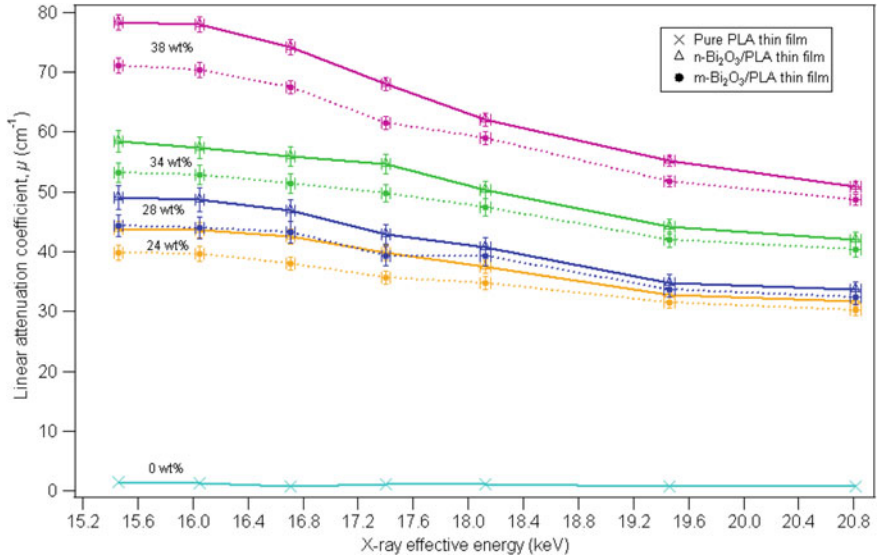

Fig. 9.4 Linear attenuation coefficient as a function of the effective energy operated by various X-ray tube voltages of the mammography unit (22–49 kV) for all Bi_2O_3 loading (0–38 wt%) of the n-Bi_2O_3/PLA and m-Bi_2O_3/PLA thin films [28]

PLA thin film and n-Bi_2O_3/PLA thin film become comparable. They only show significant X-ray attenuation differences for lower X-ray effective energy <17.4 keV (X-ray tube voltage 22–35 kV) operated from the mammography unit.

As in our previous study for the comparison of different sizes of WO_3 particles-epoxy composite [25], we also get similar results for electrospun Bi_2O_3/PLA nanofibre mats which showed that *X-ray attenuation* by electrospun n-Bi_2O_3/PLA nanofibre mat is higher than the *X-ray attenuation* by electrospun m-Bi_2O_3/PLA nanofibre mat with same filler loading (wt%) for lower X-ray tube voltage ranges (22–35 kV) operated from mammography unit. However, by increasing the X-ray tube voltage beyond 35 kV, X-ray attenuation for electrospun n-Bi_2O_3/PLA nanofibre mat is still higher than X-ray attenuation for electrospun m-Bi_2O_3/PLA nanofibre mat. In contrast, in our previous work, the differences in the attenuation by micro-sized WO_3-epoxy composites and nano-sized WO_3-epoxy composites become indistinguishable when the X-ray tube voltage was increased beyond 35 kV [25]. Only Bi_2O_3/PLA thin film has a good agreement with our previous results for X-ray tube voltages greater than 35 kV, which shows the indistinguishability in attenuation between m-Bi_2O_3/PLA thin film and n-Bi_2O_3/PLA thin film.

Figure 9.5 presents the value of μ for electrospun n-Bi_2O_3/PLA nanofibre mats for all the X-ray beam energies generated by XAS and the mammography unit. The results found from XAS unit were correlated with those from the mammography unit since the mammography unit produced effective energies of 15–21 keV with the Mo and Rh anode/filter characteristic X-ray energies of 17.5–22.7 keV, while the X-ray energy used with XAS was ~7–20 keV.

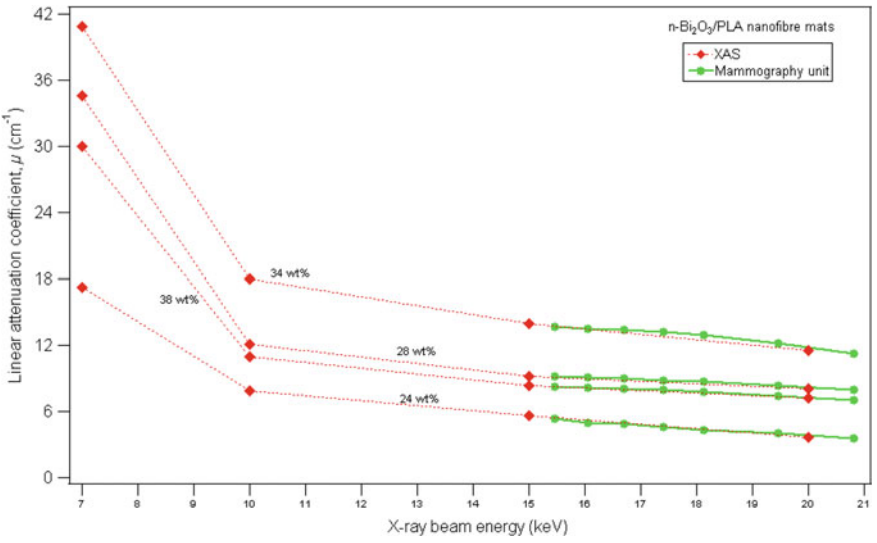

Fig. 9.5 Comparison of the linear attenuation coefficient for the electrospun n-Bi_2O_3/PLA nanofibre mats for all X-ray beam energies generated by XAS and the mammography unit [28]

Therefore, electrospun n-Bi_2O_3/PLA nanofibre mats are superior to their micro-sized counterparts in X-ray attenuation for all the X-ray beam energies (i.e. 7–20 keV and 22–49 kV) generated by XAS and mammography respectively. In contrast, n-Bi_2O_3/PLA thin films are a good X-ray shielding candidate only for the mammography unit of 22–35 kV when compared to m-Bi_2O_3/PLA thin films. Both can be chosen as X-ray shielding materials for X-ray voltages greater than 35 kV.

Basically, the total X-ray attenuation by the absorbing material is determined by three energy-dissipative mechanisms, namely photoelectric effect, Compton scattering and pair production. Pair production was not considered in this study because this mechanism will only occur when the photon energy is beyond 611 keV. In the photoelectric absorption process, a photon undergoes an interaction with an absorber atom in which the photon completely disappears. In its place, an energetic photoelectron is ejected from one of the bound shells of the atom. The photoelectric process is the predominant mode of photon interaction at relatively low photon energies and high atomic number Z, i.e. $(Z/E)^3$. Meanwhile, Compton scattering takes place between the incident photon and one of the outer shell electrons of an atom in the absorbing material. The probability of Compton scattering is almost independent of atomic number Z and X-ray energy E. It is most dominant as the photon energy increases due to a concomitant decrease in the photoelectric effect.

In addition, the number of Bi particles/gram in both n-Bi_2O_3/PLA fibre-mats and thin-films is higher than their micro-sized counterparts. Hence, the probability of X-rays with lowers energies (i.e. 7–20 keV and 22–35 kV) to interact and be absorbed by n-Bi_2O_3 filler is higher when compared to their micro-sized counterparts since the photons interact with the absorbing materials mainly by photoelectric effect.

When the X-ray tube voltage of the mammography unit is more than 35 kV (or characteristic X-ray energy >20 keV), PLA thin-films of n-Bi_2O_3 or m-Bi_2O_3 gave similar X-ray transmission for X-ray tube voltages greater than 35 kV and hence these films can be used for attenuating X-rays generated from these X-ray sources. The observed similarity in the X-ray transmission results may be attributed to: (a) the decrease of the photoelectric effect, and (b) the domination of the Compton scattering effect when the photon (X-ray) energy increases. The latter effect results in less interaction and absorption of the photon by Bi particles of these thin films; thus, the X-ray transmission of these thin films is similar. In contrast, electrospun n-Bi_2O_3/PLA nanofibre mat is superior to their micro-sized counterparts in X-ray attenuation at the same energy range. The observed large differences in X-ray attenuation of these fibre-mats may be explained by the difference in uniformity of dispersion between nano and micro-sized Bi particles within the PLA matrix where large agglomerations tend to occur for the latter.

Hence, the electrospun n-Bi_2O_3/PLA nanofibre mats of all filler loadings (24–38 wt%) are potential candidates in X-ray shielding for all the incident X-ray energy studied either by XAS (7–20 keV) or mammography (22–49 kV) when compared to their micro-sized counterparts. However, the latter may still be a suitable candidate for X-ray shielding of scattered radiations which requires very low energy. These electrospun Bi_2O_3/PLA nanofibre mats can be used as a coating material for X-ray

shielding because PLA nanofibres provide many benefits such as better tenacity, resistance to degradation and mechanical properties [18, 27].

Meanwhile, n-Bi_2O_3/PLA thin films are a good X-ray shielding candidate only for the mammography unit of 25–35 kV when compared to m-Bi_2O_3/PLA thin films. Both can be chosen as the X-ray shielding material for X-ray tube voltage greater than 35 kV.

9.2.4 Microstructure Analyses

The microstructure analysis of the electrospun nanofibres was done using both backscattered electrons and the secondary electrons to clearly show the difference between the PLA polymer and the embedded Bi elements. Figure 9.6a shows the SEM image of control electrospun PLA nanofibres without any Bi_2O_3 filler. The average diameter of these fibres was 854 ± 35 nm. The average diameter of PLA nanofibre increase when 24–34 wt% Bi_2O_3 was added in the PLA solution. For instance, Fig. 9.6b shows the homogenous nanofibres of 28 wt% of n-Bi_2O_3 filler with an average diameter of 971 ± 22 nm. Meanwhile, in Fig. 9.6c the average diameter of 28 wt% m-Bi_2O_3/PLA nanofibres is 911 ± 41 nm with a large variation and agglomerations can be observed.

This indicates that by increasing the solution viscosity while both the conductivity and the surface tension decreased with the increment of filler (Bi_2O_3) loadings within PLA solution, the average nanofibre diameter was increased. The significant increase in the viscosity of solution with increasing filler loadings was due to the increased molecular entanglement which enabled the charged jet to withstand a larger stretching force (from the Coulombic repulsion) resulting in the coarsening of the nanofibres.

In contrast, further increase of Bi_2O_3 loading to 38 wt% caused a decrease in the average diameter to 496 ± 32 nm for n-Bi_2O_3/PLA nanofibres which have a maximum diameter of 2.06 ± 0.49 μm and a minimum of 114 ± 2 nm (Fig. 9.6d). Meanwhile, the average diameter of m-Bi_2O_3/PLA nanofibres is 406 ± 71 nm with a maximum diameter of 1.13 ± 0.23 μm and a minimum of 111 ± 2 nm (Fig. 9.6e). The unexpected decrease in the average fibre diameter may be attributed to the domination of electrical conductivity when filler loading or viscosity of solution increases. As a result, this leads to the production of fibres with non-uniform diameters, as well as formation of beads and particle agglomerations.

Images in Fig. 9.7a–c illustrate the EDS results for the electrospun n-Bi_2O_3/PLA nanofibre mat with 34 wt% filler loading which confirms the existence of Bi element from the filler together with elements C and O from PLA matrix. The SEM images of m-Bi_2O_3/PLA and n-Bi_2O_3/PLA thin films with 28 wt% filler loading are shown in Fig. 9.8 which indicate the presence of agglomerations within PLA matrix.

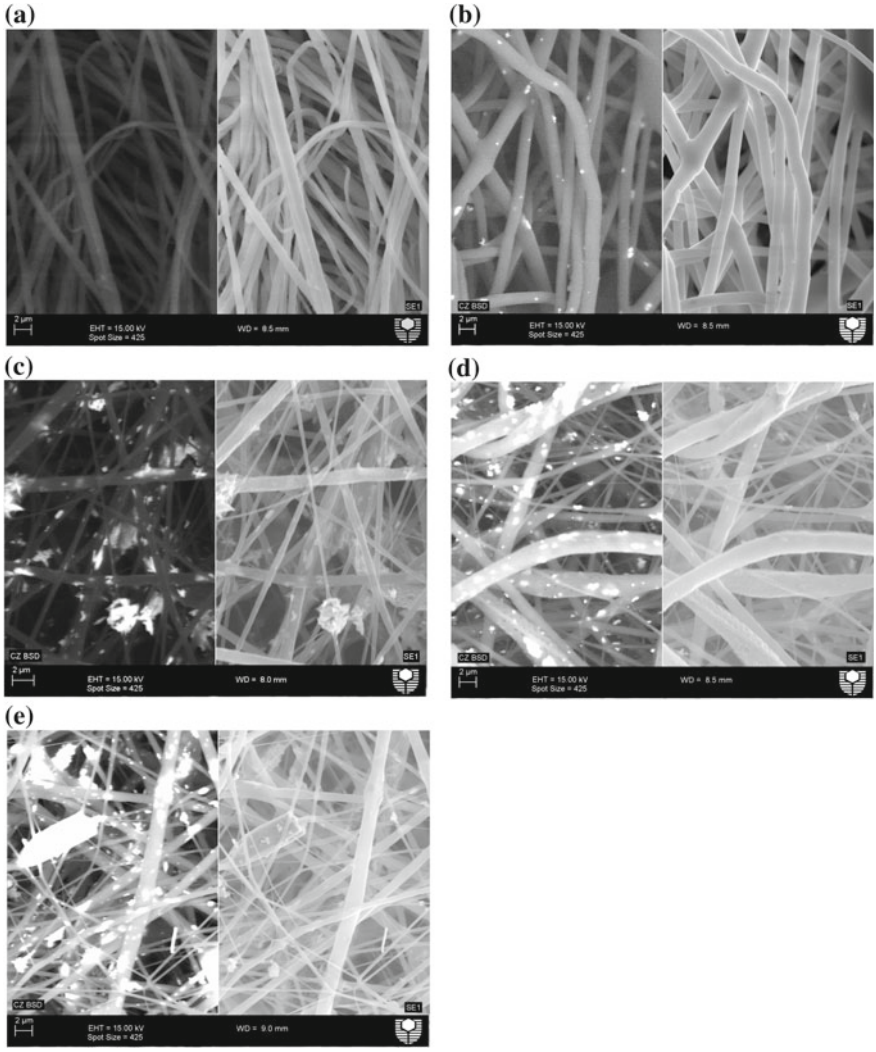

Fig. 9.6 SEM image showing the images performed by backscattered electron technique on the left and the secondary electron technique on the right for **a** the control electrospun PLA nanofibres without any particles (0 wt% of Bi_2O_3); **b** 28 wt% Bi_2O_3 of electrospun n-Bi_2O_3/PLA nanofibres; **c** 28 wt% Bi_2O_3 of electrospun m-Bi_2O_3/PLA nanofibres; **d** 38 wt% Bi_2O_3 of electrospun n-Bi_2O_3/PLA nanofibres; and **e** 38 wt% Bi_2O_3 of electrospun m-Bi_2O_3/PLA nanofibers [28]

9.3 Conclusions

The electrospun nanofibre mats of n-Bi_2O_3/PLA and m-Bi_2O_3/PLA with filler loadings of 24–38 wt% were successfully fabricated. From the analyses, the electrospun n-Bi_2O_3/PLA nanofibre mats of all filler loadings are superior in attenuating X-rays

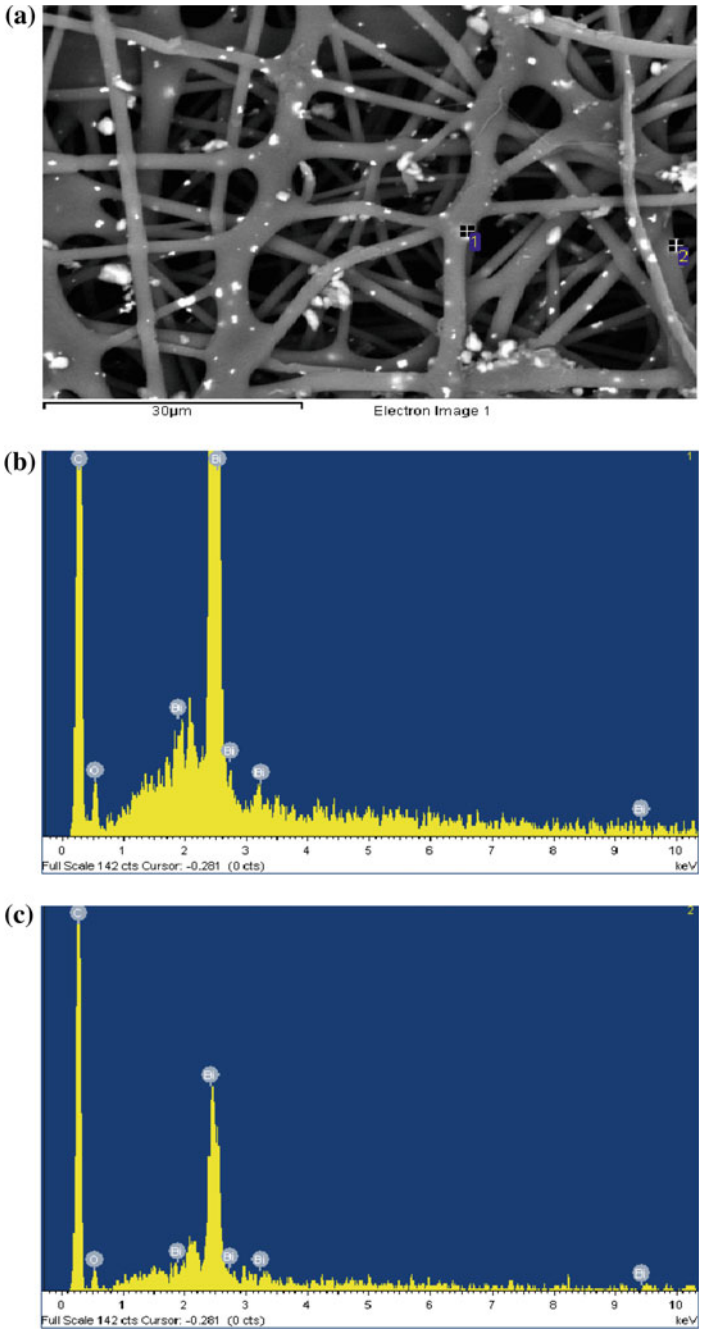

Fig. 9.7 **a** SEM image used for EDS analyses on 34 wt% Bi_2O_3 of the electrospun n-Bi_2O_3/PLA nanofibres to prove that only Bi particles detected other than C and O which is the composition of PLA; EDS analyses for **b** point 1 and; **c** point 2 marked in **a** [28]

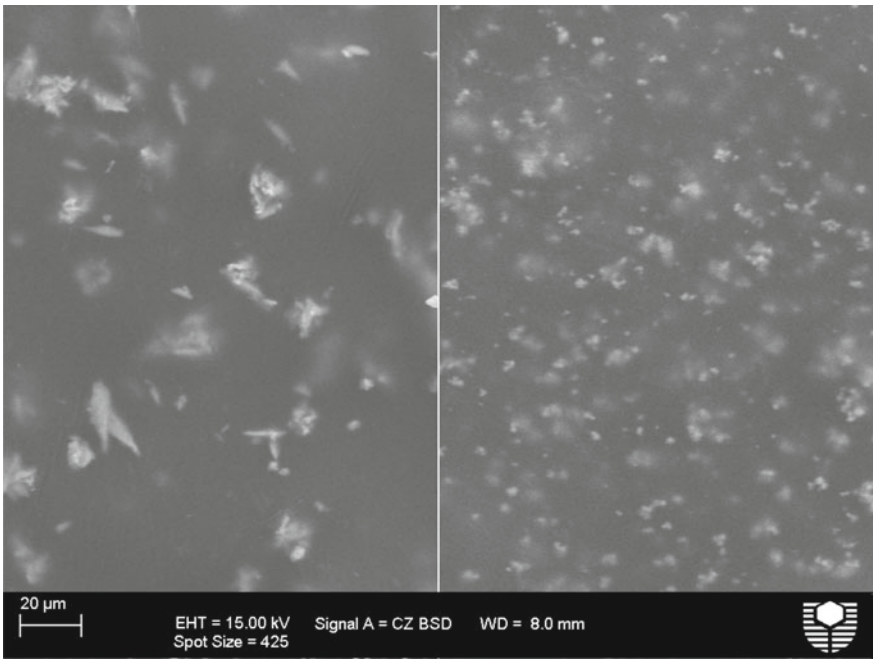

Fig. 9.8 SEM images of the thin film of 28 wt% Bi_2O_3 for m-Bi_2O_3/PLA on the left showing agglomerations and n-Bi_2O_3/PLA on the right [28]

as compared to their micro-sized counterparts because the X-ray transmission is strongly dependent on the particle size and the photoelectric interaction. However, the electrospun Bi_2O_3/PLA nanofibre mats with 38 wt% loading is not recommended for X-ray shielding because of higher porosity as compared to the lower filler loadings. The n-Bi_2O_3/PLA thin films are a good X-ray shielding candidate only for the mammography unit of 22–35 kV when compared to the m-Bi_2O_3/PLA thin films. The particle size effect on X-ray attenuation diminished as the X-ray tube voltage exceeds 35 kV.

Acknowledgements The collection of X-ray absorption spectroscopy (XAS) data was funded by the Australian Synchrotron (AS123/XAS5341). We thank our colleagues Dr. C. Ng and A/Prof. Z. Sun for assistance with XAS data collection. Also, we would like to thank Carolyn Madeley of Breast Assessment Centre, Royal Perth Hospital, Western Australia for giving us the opportunity to use the mammography unit.

References

1. Patra CR, Bhattacharya R, Mukhopadhyay D, Mukherjee P (2010) Fabrication of gold nanoparticles for targeted therapy in pancreatic cancer. Adv Drug Deliv Rev 62:346–361
2. Huang X, El-Sayed MA (2010) Gold nanoparticles: optical properties and implementations in cancer diagnosis and photothermal therapy. J Adv Res 1:13–28
3. Granmayeh Rad A, Abbasi H, Afzali MH (2011) Gold nanoparticles: Optical properties and implementations in cancer diagnosis and photothermal therapy. Phys Procedia 22:203–208
4. Sahare PD, Ranju R, Numan S, Lochab SP (2007) K3Na(SO4)2: Eu nanoparticles for high dose of ionizing radiation. J Phys D Appl Phys 40:759
5. Lines MG (2008) Nanomaterials for practical functional uses. J Alloy Compd 449:242–245
6. Haiwen X, Kai-Zhong G, Yiming S, Song X (2006) Precessional dynamics of single domain magnetic nanoparticles driven by small ac magnetic fields. J Phys D Appl Phys 39:4746
7. Popov A (2009) Sun protection using nanoparticles 24:1–2
8. Storrie H, Mooney DJ (2006) Sustained delivery of plasmid DNA from polymeric scaffolds for tissue engineering. Adv Drug Deliv Rev 58:500–514
9. Botelho MZ, Künzel R, Okuno E, Levenhagen RS, Basegio T, Bergmann CP (2011) X-ray transmission through nanostructured and microstructured CuO materials. Appl Radiat Isot 69:527–530
10. El Haber F, Froyer G (2008) Transparent polymers embedding nanoparticles for x-rays attenuation (Review). J Univ Chem Technol Metall 43:283–290
11. Buyuk B, Tugrul AB, Akarsu AC, Addemir AO (2012) Investigation on the effects of titanium diboride particle size on radiation shielding properties of titanium diboride reinforced boron carbide-silicon carbide composites'. J Nano- Electron Phys 4:01010(01011)–01010(01014)
12. Künzel R, Okuno E (2012) Effects of the particle sizes and concentrations on the X-ray absorption by CuO compounds. Appl Radiat Isot 70:781–784
13. Faccini M, Vaquero C, Amantia D (2012) Development of protective clothing against nanoparticle based on electrospun nanofibres. J Nanomater 2012:1–9
14. Molamma PP, Venugopal J, Casey KC, Ramakrishna S (2008) Surface modified electrospun nanofibrous scaffolds for nerve tissue engineering. Nanotechnology 19:455102
15. Sill TJ, von Recum HA (2008) Electrospinning: Applications in drug delivery and tissue engineering', Biomaterials 29:1989–2006
16. Russo G, Lamberti G (2011) Electrospinning of drug-loaded polymer systems: Preparation and drug release. J Appl Polym Sci 122:3551–3556
17. Huang S, Kang X, Cheng Z, Ma P, Jia Y, Lin J (2012) Electrospinning preparation and drug delivery properties of Eu3+/Tb3+ doped mesoporous bioactive glass nanofibres. J Colloid Interface Sci 387:285–291
18. Haroosh HJ, Chaudhary DS, Dong Y (2012) Electrospun PLA/PCL fibres with tubular nanoclay: Morphological and structural analysis. J Appl Polym Sci 124:3930–3939
19. Yiin-Kuen F, Li-Chih L (2013) Pattern transfer of aligned metal nano/microwires as flexible transparent electrodes using an electrospun nanofiber template. Nanotechnology 24:055301
20. Rajeswari R, Jayarama Reddy V, Subramanian S, Shayanti M, Radhakrishnan S, Seeram R (2012) Minimally invasive injectable short nanofibres of poly(glycerol sebacate) for cardiac tissue engineering. Nanotechnology 23:385102
21. Hu W, Huang ZM, Liu XY (2010) Development of braided drug-loaded nanofibre sutures. Nanotechnology 21:315104
22. Yu DG, Shen XX, Chris BW, Kenneth W, Zhu LM, Bligh SWA (2009) Oral fast dissolving drug delivery membranes prepared from electrospun polyvinylpyrrolidone ultrafine fibres. Nanotechnology 20:055104
23. Lee S, Obendorf SK (2007) Use of electrospun nanofibre web for protective textile materials as barriers to liquid penetration. Text Res J 77:696–702
24. Brettmann BK, Tsang S, Forward KM, Rutledge GC, Myerson AS, Trout BL (2012) Free surface electrospinning of fibres containing microparticles. Langmuir 28:9714–9721

25. Noor Azman NZ, Siddiqui SA, Hart R, Low IM (2013) Effect of particle size, filler loadings and x-ray tube voltage on the transmitted x-ray transmission in tungsten oxide-epoxy composites. Appl Radiat Isot 71:62–67
26. Suk CC, Wei LJ, Harun AZ (2012) Evaluation of X-ray beam quality based on measurements and estimations using SpekCalc and Ipem78 models', Malays J Med Sci 19:22–28
27. Farrington DW, Lunt J, Davies S, Blackburn RS (2005) Biodegradable and sustainable fibres', in Poly (lactic acid) fibres. Woodhead Publishing Series in Textiles, Cambridge, United Kingdom, pp 191–220
28. Noor Azman NZ, Siddiqui SA, Haroosh HJ, Albetran HM, Johannessen B, Dong Y, Low IM (2013) oxide/polylactic acid nanofibre mats. J Synchrotron Radiat 20:741–748

Chapter 10
Effect of Bi_2O_3 Particle Sizes and Addition of Starch into Bi_2O_3–PVA Composites for X-Ray Shielding

Abstract The effect of Bi_2O_3 particle sizes filled PVA composites on X-ray transmission for X-ray shielding purpose had been successfully fabricated and analyzed by using X-ray fluorescent spectroscopy (XRF) and mammography units with various low X-ray energy ranges. Besides, a preliminary investigation was carried out by using XRF unit to obtain the effect of starch addition into the composite on the X-ray transmissions by both particle sizes of Bi_2O_3–PVA composites. The results showed that the ability of the composite to attenuate the initial X-ray beam was augmented with the increased Bi_2O_3 weight percentage (wt%). The density of both particle sizes of Bi_2O_3–PVA composites was compared with the addition of 1 and 3 wt% starch, while a fluctuation of density occurred for the composites without starch. Moreover, the nanosized Bi_2O_3–PVA composite without starch did not exemplify better X-ray attenuation capability compared to its micro-sized counterpart even though their density was higher than the micro-sized Bi_2O_3–PVA composite. However, the nano-sized Bi_2O_3–PVA composite with starch offered better particle size effect for X-ray shielding ability than its micro-sized counterpart compared to the Bi_2O_3–PVA composites without starch.

10.1 Introduction

The ionizing radiation (X-rays or gamma rays) is harmful to the environment, especially toward the human health, causing diffuse damage at the cellular level and throughout the body. Thus, the basic principle of radiation protection should be considered by applying the three rules, such as the shortest time, the longest distance, and the shielding materials. Radiation shielding plays an important role in handling radiation, especially X-rays and gamma rays [1–4]. Prior to this reason, lead and thick concrete materials are suitable to reduce radiation intensities. The lead glass has been widely used as radiation shielding due to its ability to attenuate radiation. Unfortunately, lead glass is considered as toxic to environmental. However, lead glass is considered as heavy, fragile, and also an expensive product for radiation shielding purposes [3–7]. Therefore, many researchers have attempted to fabricate

© Springer Nature Singapore Pte Ltd. 2020

I. M. Low and N. Z. Noor Azman, *Polymer Composites and Nanocomposites for X-Rays Shielding*, Composites Science and Technology,
https://doi.org/10.1007/978-981-13-9810-0_10

polymer composite in order to replace lead as the radiation shielding material. Polymer exhibits property's enhancement, including low density, low manufacturing cost, good film forming, and it is also easy to produce. Composite is defined as a combination of a variety of fibers bonding with a matrix material that offers better mechanical properties.

Based on these excellent mechanical properties, the usage of polymer composite has been widely developed nowadays. The fundamental understanding between polymer composite and radiation shielding is that the presence of polymer composite reduces X-ray transmission [2, 3, 8–13]. In comparison with other polymers, polyvinyl alcohol (PVA) is the most important polymer due to its exclusive chemical and physical features. It is a hydrophilic and semicrystalline polymer that has received much attention due to its good chemical resistance, good thermal stability good physical properties, excellent biocompatibility, and inexpensive. Moreover, it also has been frequently used in medical devices due to its biocompatibility, low protein adsorption characteristics, and chemical resistance [14]. Besides, PVA is also capable of interacting with both organic and inorganic compounds due to the presence of hydroxyl group, besides possessing an uncomplicated chemical structure and modifications are possible by simple chemical reactions [15]. Furthermore, PVA also offers good film forming and emulsification that has been used in film and fibers. Hence, these properties of PVA have made it adaptable for many applications, such as for image storage, photovoltaic cells, textile industries, sensors, and medical devices. In fact, some researchers have stated that PVA is suitable to be mixed together with natural polymers due to its high polar attribute [7]. Other than that, among natural polymers, the use of starch is applied in different fields as it is one of the most promising biocompatible and biodegradable materials that is universally available and of low cost. Starch, as a widely available raw material, seems to be a very good substrate for preparation of nanoparticles [16, 17]. In fact, starch, such as potato or corn starch, is an example of natural polymer that offers unique properties, such as low in price, renewable, found in abundance, and can be obtained from a variety of plant sources. However, it is sensitive to water, like polymers. This limitation, nonetheless, can be improved by blending it together with another polymer [18]. The combination of starch with PVA, eventually, changes the thermomechanical properties of the composite as this combination affects the structure of both polymers. As starch interacts with the polar synthetic of PVA, the presence of bonding hydroxyl functional group (–OH) tends to build strong hydrogen bonding among the molecules and to have better system integrity [9, 19]. Meanwhile, as for X-ray shielding purpose, metal elements with high atomic number and high density can impart higher shielding protection. For instance, Maghrabi et al. [20] proposed that Bi_2O_3 compound in a suitable resin matrix can be coated on fabrics, and it had been an effective method to produce flexible, wearable, and lead-free aprons since bismuth (Bi) has high atomic number ($Z = 83$) and high density (8.90 g/cm^3). Besides, Nambiar et al. [21, 22] prepared polydimethylsiloxane (PDMS) composites with different mixtures of high atomic number Bi compounds, including $(WO_4)_3$ and bismuth oxide (Bi_2O_3), for X-ray shielding purposes. Furthermore, they found that a PDMS composite with $Bi_2(WO_4)_3$ had an increased X-ray attenuation compared

to PDMS-only materials [21]. On top of that, they also found that a PDMS/Bi_2O_3 nanocomposite with 44.44 wt% Bi_2O_3 was equally capable of attenuating an X-ray beam produced at 60 kV, which is a beam commonly used in interventional radiology procedures [22].

In the early 21st century, microtechnology and nanotechnology have a great impact on society. Researches in both particle size technologies have been a breakthrough as an intelligent system, sensing, processing, and functions. In terms of X-ray shielding, the comparison between both micro- and nano-sized particles has been investigated by various researchers. The investigation of the effect of different-sized particles and its concentration on the radiation absorption become important in order to yield lead-free based compound. Moreover, it was understood that the ability of X-ray attenuation can be improved based on the dispersion concept of nano-sized particles since they are able to disperse significantly and display better uniformity compared to those micro-sized particles. In fact, some available nano-sized particles used as polymer filler for radiation shielding are copper (II) oxide (CuO), tungsten (III) oxide (WO_3), and lead (II) oxide (PbO) [11–13, 23]. With that, the present study synthesized PVA composite with Bi_2O_3 filler for measurement of X-ray transmission. The X-ray transmission of both nano- and micro-sized particles had been characterized by using different modalities at low X-ray energy ranges. On top of that, the effect of starch addition into the Bi_2O_3–PVA composites toward X-ray transmission was also studied.

10.2 Results and Discussion

10.2.1 Density of the Composites

The usage of different wt% bismuth (III) oxide (Bi_2O_3) had been found to significantly affect the density of the Bi_2O_3–PVA composite, as clearly shown in Table 10.1. The increment of Bi_2O_3 filler loading (wt%) to the composite mixture increased the density of the composite material due to the heavier density of filler (8.90 g/cm^3).

Table 10.1 Density of Bi_2O_3–PVA composite without starch

Filler (wt%)	Density (g/cm^3)	
	Micro-sized Bi_2O_3–PVA	Nano-sized Bi_2O_3–PVA
0	1.16	1.16
8	1.19	1.25
12	1.28	1.32
15	1.32	1.33
18	1.37	1.38
21	1.41	1.41

Table 10.2 Density of Bi_2O_3–PVA with addition of 0–3 wt% of starch

Filler (wt%)	Density (g/cm^3)					
	Micro-sized Bi_2O_3–PVA			Nano-sized Bi_2O_3–PVA		
	Starch (0 wt%)	Starch (1 wt%)	Starch (3 wt%)	Starch (0 wt%)	Starch (1 wt%)	Starch (3 wt%)
8	1.19	1.17	1.19	1.25	1.18	1.21
12	1.28	1.19	1.22	1.32	1.20	1.23
15	1.31	1.20	1.26	1.33	1.22	1.26

Similarly, the outcome was also agreed by the composite with the addition of starch into the composite. The combination of highdensity filler compound and low-density polymer matrix, respectively, caused the density of the composites to increase [23–26]. Meanwhile, for 8 wt% filler (Table 10.2), the density for micro-sized Bi_2O_3–PVA composite with the addition of 3 wt% starch had been similar to that with 0 wt% starch. Nevertheless, by adding 1 wt% starch, the density was decreased compared to them. This had been due to the lack of PVA to completely cover the surfaces of Bi_2O_3 filler powder, resulting in the concomitant increase in the number of pores and, thus, reducing the density of the composite since starch is known as a pore-forming agent [27]. Moreover, Emrullahoğlu Abi and Yanar [27] concluded that the porosity of materials can be controlled by the amount (nominal content) of starch added to the suspension and that the pore size can be controlled by the type of pore-forming agent. In addition, all the density values of Bi_2O_3–PVA composites with the addition of 1 wt% starch into both microsized and nano-sized mixture composites were lesser than those with 3 wt% starch and 0 wt% starch, respectively. Even though the densities of Bi_2O_3–PVA composites with the addition of 1 and 3 wt% starch were lesser than that with 0 wt% starch, the density for both micro-sized and nano-sized Bi_2O_3–PVA composites had been comparable, while the composites without starch (0 wt%) showed a fluctuation in the densities.

10.2.2 X-Ray Transmission by the Composites Without Starch

Figure 10.1 shows the reduction of X-ray transmission by both micro-sized and nano-sized Bi_2O_3–PVA composites (without the addition of starch) with the increment of filler loading for the X-ray energy of 16.59 keV (Fig. 10.1a), 17.46 keV (Fig. 10.1b), 21.21 keV (Fig. 10.1c), 22.20 keV (Fig. 10.1d), and 25.2 keV (Fig. 10.1e) of XRF unit, respectively. The trends of the X-ray transmission obtained for the samples looked similar, which further implied that the nano-sized Bi_2O_3–PVA composite exhibited higher X-ray transmission than its micro-sized counterpart for all the X-ray energies, except for X-ray energy at 16.59 keV, which showed lower X-ray transmission by 8 wt% of nanosized Bi_2O_3–PVA composite compared to the same wt% of micro-sized Bi_2O_3–PVA composite. Without the addition of starch into the composite, the pattern

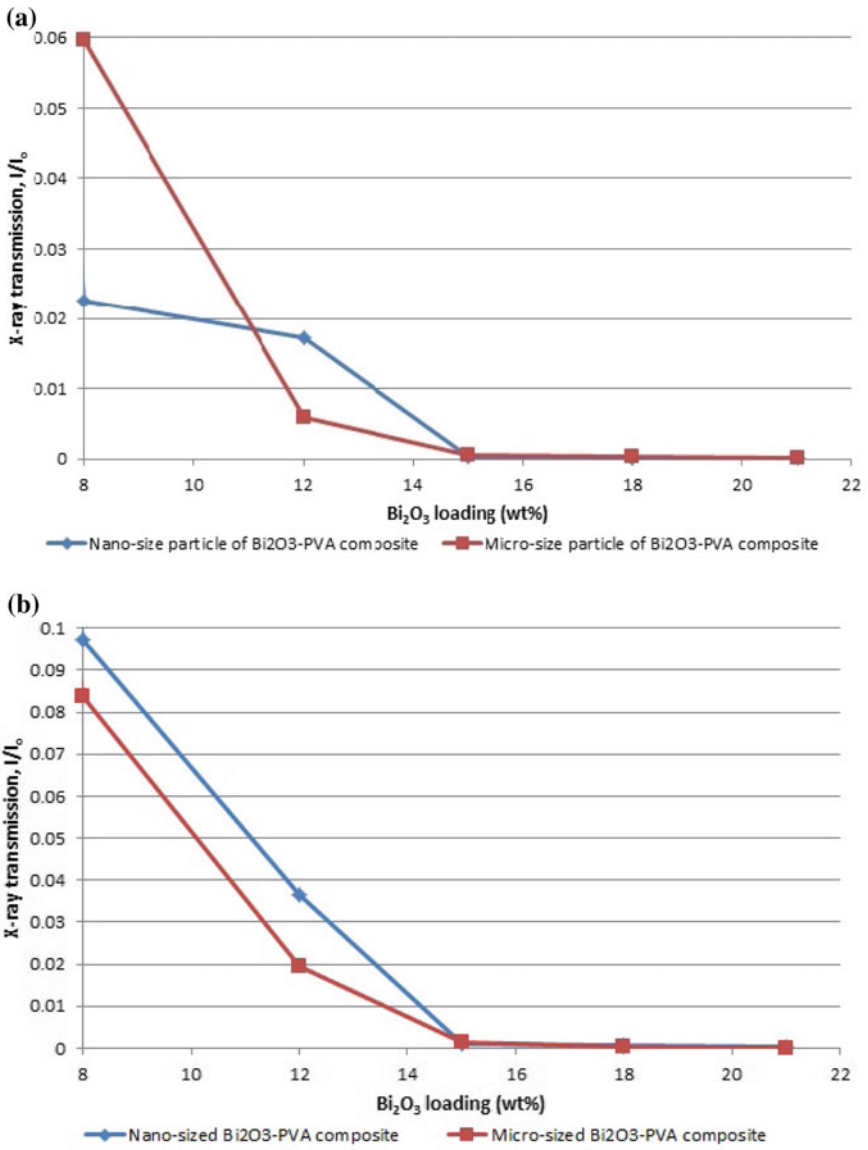

Fig. 10.1 X-ray transmission comparison between nano-sized and micro-sized Bi_2O_3–PVA composites without starch at XRF X-ray energy: **a** 16.59 keV, **b** 17.46 keV, **c** 21.21 keV, **d** 22.20 keV, and **e** 25.2 keV [31]

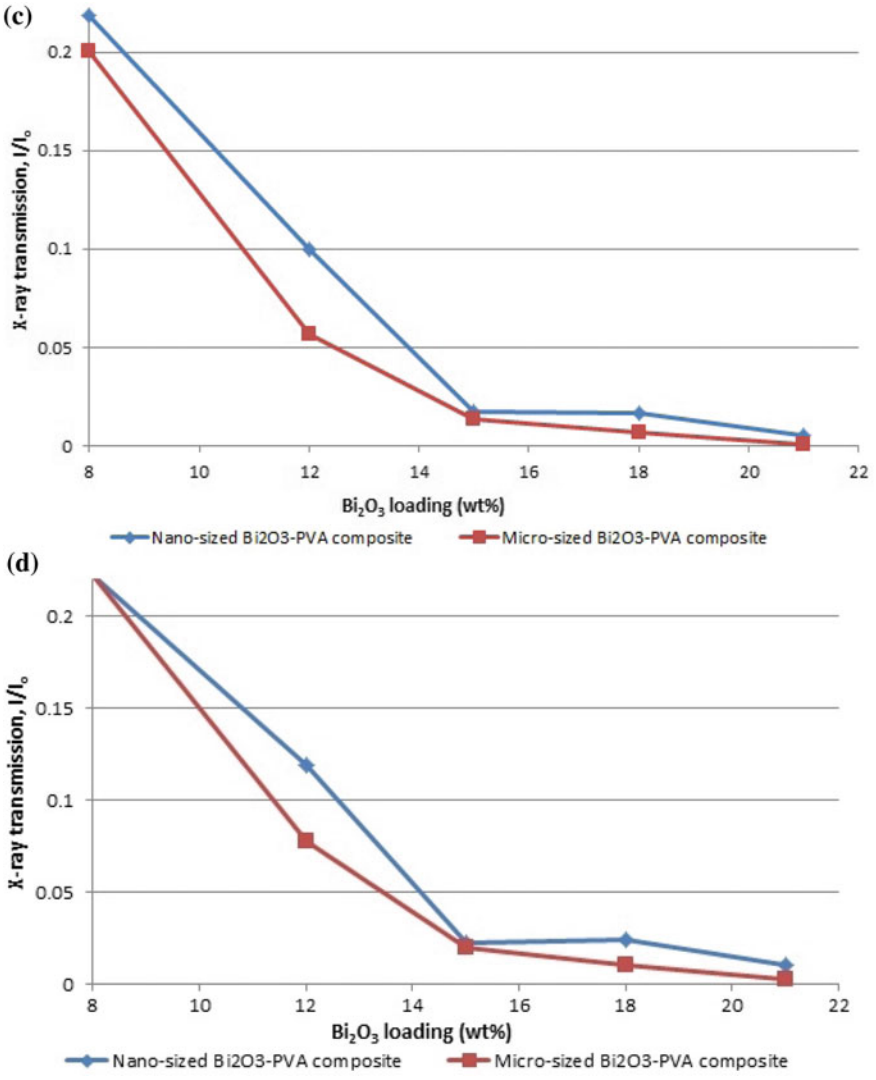

Fig. 10.1 (continued)

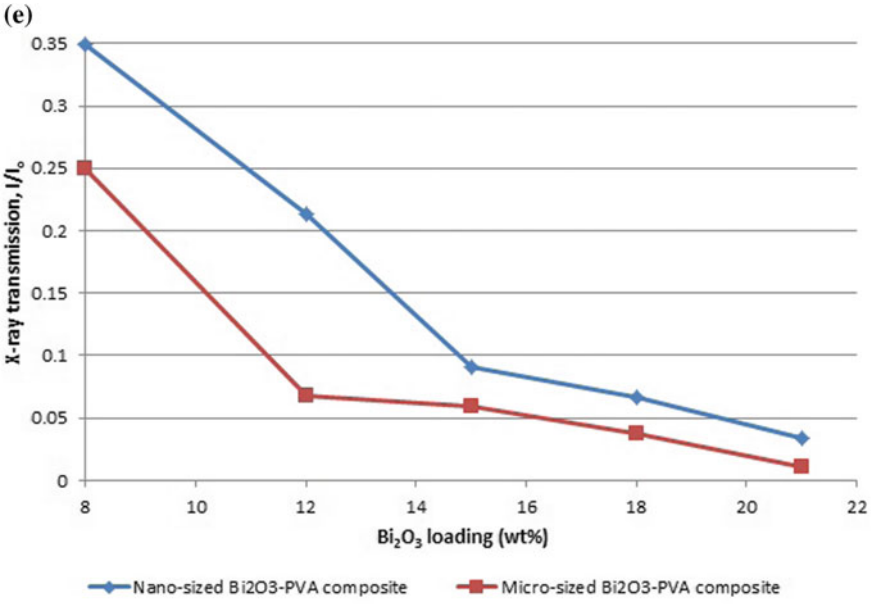

Fig. 10.1 (continued)

of X-ray transmission for both Bi_2O_3 particle sizes with similar weight percentage in the composite was not uniform. In fact, the nano-sized particle Bi_2O_3 did not display better X-ray attenuation capability compared to its micro-sized counterpart, as described in other studies [3, 11], even though their density had been higher than that of the micro-sized Bi_2O_3–PVA composite (Table 10.1). Consequently, the ratio of X-ray transmission (T_m/T_n) between the micro-sized particle Bi_2O_3–PVA composites (T_m) and the nano-sized particle counterparts (T_n) for all filler wt% investigated from XRF unit of all the X-ray energies (16.59, 17.46, 22.20, 21.21, and 25.2 keV) studied in this work occurred randomly, i.e., $T_m/T_n \sim 0.7–2.64$. Moreover, the ratio (T_m/T_n) of 8 wt% of Bi_2O_3–PVA composite was within the range of 0.7–2.64. The sample with 8 wt% of nano-sized Bi_2O_3–PVA composite enhanced the attenuation compared to its micro-sized counterpart at X-ray energy 16.59 keV with $T_m/T_n = 2.64$, while for the other X-ray energies, the ratio was $T_m/T_n < 1.0$. Meanwhile, the ratios (T_m/T_n) of 12, 15, 18, and 21 wt% of Bi_2O_3–PVA composites had been in the range of 0.20–0.91 for all the X-ray energy ranges. These results showed that the sample of micro-sized particle Bi_2O_3–PVA composite exhibited better attenuation, as illustrated in Fig. 10.1. The main reason for obtaining these results might come from Bi nanoparticles that dispersed non-uniformly and non-homogeneously within the PVA solution during the drying process. Furthermore, the measurement of X-ray transmission by the Bi_2O_3–PVA composites without starch from mammography unit also depicted a similar result retrieved from the XRF unit, where the X-ray transmissions of both Bi_2O_3 particle sizes decreased as the wt% of Bi_2O_3 was increased. Moreover,

the X-ray beams, which were generated by the Mo/Mo anode/filter combination, had been composed mainly of the characteristic X-ray energies of molybdenum (17.5 and 19.6 keV). Meanwhile, the X-ray transmission of the sample at X-ray tube voltages of 25–27 kV operated from the mammography unit is illustrated in Fig. 10.2a. Illustrations in Fig. 10.2b, c portray the results at tube voltages of 29–31 and 33–35 kV, respectively. Besides, Fig. 10.2 shows that the value of X-ray transmission by the composites decreased with the increasing X-ray energy. Bi_2O_3–PVA composite of 8 wt% nano-sized Bi_2O_3 exhibited good X-ray attenuation ability compared to its micro-sized counterpart since the ratio of (T_m/T_n) was within the range of 1.2–2.4 for tube voltages of 25–33 kV. Meanwhile, the ratio (T_m/T_n) < 1.0 was found only for tube voltage of 35 kV. However, these results contradicted with the result found for X-ray energy of 16.59 keV from XRF unit, which only showed the ratio of T_m/T_n = 2.64, while T_m/T_n < 1.0 for the X-ray energy of 17.46–25.2 keV. The fluctuation in the results might be due to the effect of heat dissipation caused by the anode. Heat could be spread over a large area by rotating the anode during exposure. The usage of fine focal spot (0.1 mm) used during the irradiations successfully reduced geometrical bluntness as the spatial resolution was highly dependent upon it. However, the small area of the focal spot on the anode limited the current of the tube and the X-ray output that could be sustained without damage from excessive temperature [28]. Hence, this would be at the expense of excess heating and further affected the measurement. Nonetheless, samples with 12, 15, and 18 wt% of Bi_2O_3 had T_m/T_n in the range of 0.28–0.96. As the ratio of (T_m/T_n) was less than 1.0, it indicated that the X-ray transmitted through the sample of micro-sized Bi_2O_3–PVA composite had been lower compared to the sample of nano-sized Bi_2O_3–PVA composite. These results agreed with the results obtained from the XRF measurements. Nevertheless, the X-ray transmission generated by the mammography unit could not be compared at 21 wt% of Bi_2O_3 loading as the calculated dose parameter detected had exceeded the specified range. On top of that, in previous works conducted by other researchers, the particle size effect of Bi_2O_3–PVA composite on the X-ray transmission was negligible at high X-ray energy ranges (40 kV) as they discovered that the ratio of (T_m/T_n) ≈ 1.0, which indicated that $T_m \approx T_n$ [3, 11]. This outcome might have been due to the Compton scattering effect at high X-ray energy. As the probability of the Compton scattering effect had been high, the X-ray attenuation by the composite might be decreased. Besides, once the Compton scattering effect had been found dominant at higher X-ray energy, the interaction and the absorption were similar for both nano-sized and microsized Bi_2O_3–PVA composites [3, 11, 29, 30].

10.2.3 Effect of Starch Addition on the X-Ray Transmission

Apart from that, the addition of starch into Bi_2O_3–PVA mixture, in order to form composites, offered better dispersion of filler within the PVA matrix. Table 10.2 shows that the densities for both micro-sized and nano-sized Bi_2O_3–PVA composites had been quite similar to those added with starch compared to the composites without

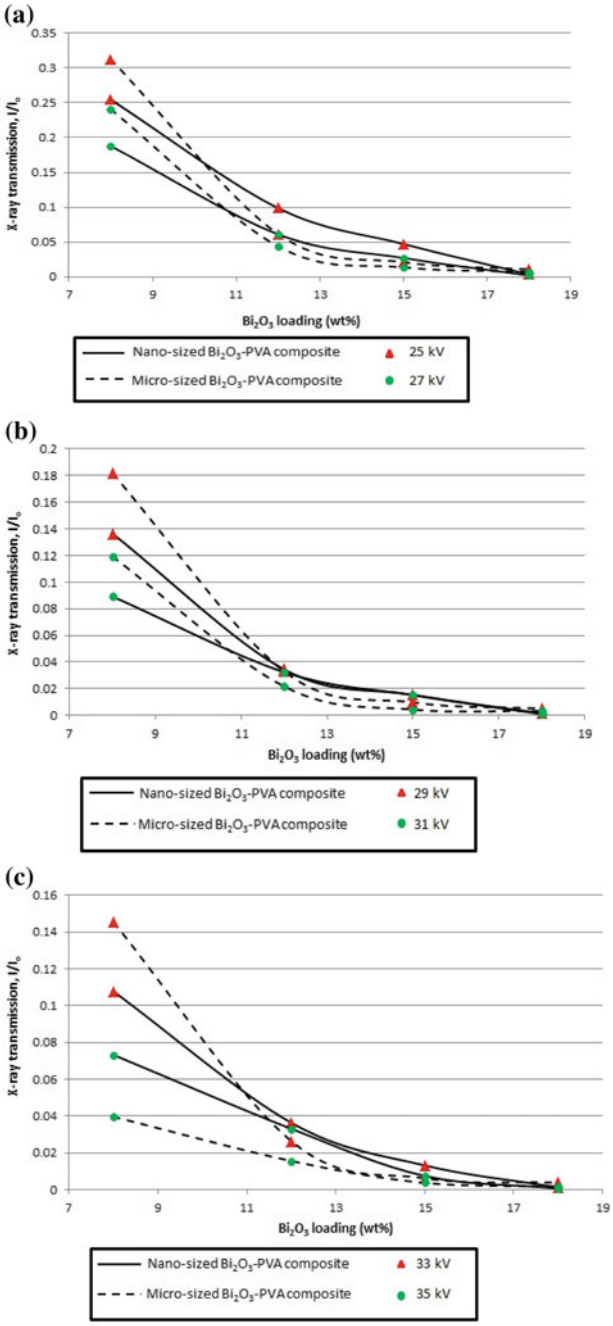

Fig. 10.2 X-ray transmission comparison between nano-sized and micro-sized Bi_2O_3–PVA composites without starch at mammography unit with tube voltage: **a** 25 and 27 kV, **b** 29 and 31 kV, as well as **c** 33 and 35 kV [31]

starch (0 wt%), even though their densities were lower than the composites without starch. Figure 10.3 shows the X-ray transmission for Bi_2O_3–PVA composites (8, 12, and 15 wt% of Bi_2O_3 loadings) with the addition of 1 and 3 wt% of starch at X-ray energy 16.59 keV (Fig. 10.3a), 17.46 keV (Fig. 10.3b), and 22.20 keV (Fig. 10.3c) of XRF unit. The decrement of X-ray transmission revealed in the sample after adding the starch into it for all the X-ray energy ranges from XRF unit was similar to the trend found from the X-ray transmission for sample without starch with increment in filler loading for both wt% of starch. Furthermore, some discrepancies of X-ray transmission were discovered between nano-sized and microsized particles without starch. However, the addition of starch into both particle sizes of Bi_2O_3–PVA composites improved the X-ray attenuating ability for all the X-ray energy ranges studied in this work from XRF unit. Once the wt% of Bi_2O_3 was increased, the ratio of (T_m/T_n) became larger (>1.0). Other than that, the ratio of (T_m/T_n) for the sample with the addition of 1 and 3 wt% of starch in 8 wt% Bi_2O_3 was in the range of 1.0–1.31. On the contrary, the sample in the absence of starch only had (T_m/T_n) 0.7–1.0, except for the X-ray energy 16.59 keV with a sudden increase to $T_m/T_n = 2.64$. Moreover, the ratio of (T_m/T_n) for 12 wt% of Bi_2O_3–PVA composites with 1 and 3 wt% of the starch was 1.1–1.45, while the ratio of (T_m/T_n) for the sample without starch was within the range of 0.35–0.65. Similarly, the ratio of (T_m/T_n) for 15 wt% of Bi_2O_3 with 1 and 3 wt% of the starch was 1.32–3.7, whereas for the sample without starch, it was only 0.8–0.9. Bi_2O_3–PVA composite without the addition of starch, nonetheless, showed that the micro-sized particle Bi_2O_3–PVA composite exhibited better attenuation compared to its nano-sized counterpart. However, obviously, with the presence of starch in the nano-sized Bi_2O_3–PVA composite, better X-ray attenuation ability was displayed as compared to that of the micro-sized Bi_2O_3–PVA composite. In fact, an X-ray transmission comparison between nano-sized and micro-sized Bi_2O_3–PVA composites without the addition of starch (0 wt% of starch) and with additional 1 and 3 wt% of starch at XRF X-ray energy 21.21 keV had been studied (Fig. 10.4). Moreover, similar tendency of the X-ray transmission by these samples was found for the rest of the X-ray energies studied. The outcomes showed that the reduction of X-ray transmission did not depend on the increment of Bi_2O_3–PVA composite density; nonetheless, interestingly, it depended on the addition of starch during the mixing process. This improvement in the composite generated the formation of hydrogen bonds that offered better stability from the starch as the stabilizing agent. Recently, Virkutyte and his colleagues [32] discovered that it is vital to select stabilizing agents that are able to avoid the undesired effects, such as aggregation of metal nanoparticles in aqueous solutions and organic solvents that opened up vast opportunities, for their utilization and potential mass production to be selective for desired applications. Furthermore, the interaction between the –OH group of starch and the –OH group of PVA promoted improvement in the composite by preventing the brittleness of the composite [9, 28]. In addition, a recent study by Nikroo and his colleagues [33] also suggested that the usage of water-soluble starch as a stabilizer for the Fe/Ni nanoparticles tended to reduce agglomeration and discrete particle. Moreover, El-Rafie et al. [34] also confirmed that maize starch played a dual role

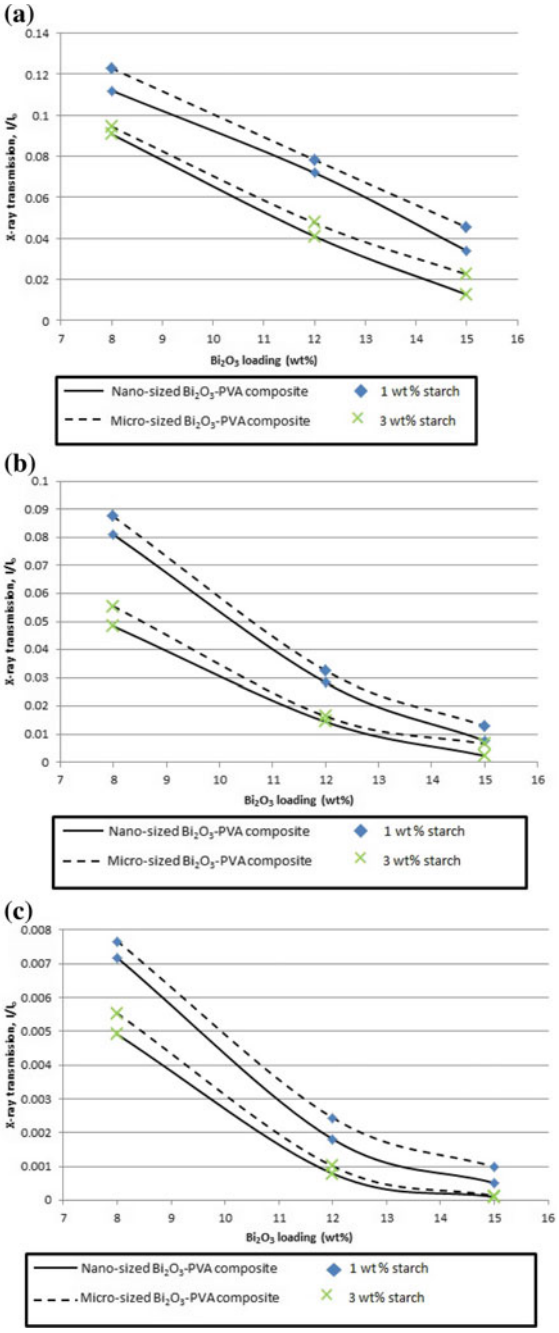

Fig. 10.3 X-ray transmission comparison between nano-sized and micro-sized Bi_2O_3–PVA composites with additional 1 and 3 wt% of starch at XRF X-ray energy: **a** 16.59 keV, **b** 17.46 keV, and **c** 22.20 keV [31]

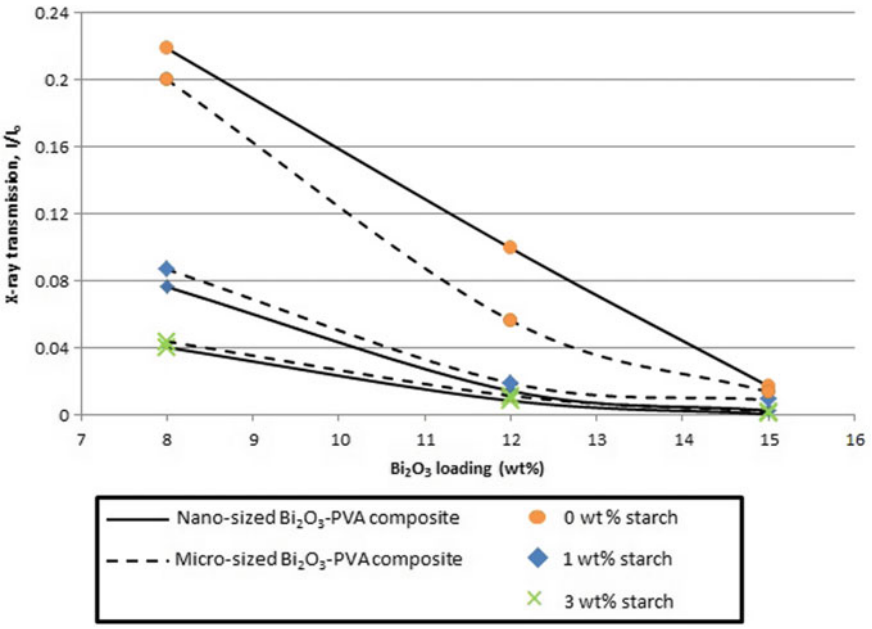

Fig. 10.4 X-ray transmission comparison between nano-sized and micro-sized Bi_2O_3–PVA composites with additional 0, 1, and 3 wt% of starch at XRF X-ray energy 21.21 keV [31]

as a reducer for silver nitrate ($AgNO_3$) and as a stabilizer for synthesizing AgNPs without using any hazardous chemical or any intermediate complicated steps.

Consequently, this result showed that the production of radiation shielding by using the nanoparticle–polymer composites with the addition of starch has become superior in terms of X-ray attenuation due to the benefits found in starch in improving the dispersion of the nanoparticles within the polymer, besides providing a better particle size effect comparison for X-ray shielding purpose. Figure 10.5 provides the preliminary analysis on the dispersion of 15 wt% Bi nanoparticles within the PVA matrix without starch (Fig. 10.5a) and with 1 wt% starch (Fig. 10.5b) addition. In fact, Bi nanoparticle agglomerations are shown in Fig. 10.5a, while Fig. 10.5b shows the improvement in the dispersion of Bi nanoparticles within PVA matrix with the support of 1 wt% starch. Nonetheless, further research is warranted to gain better understanding of the Bi particle distribution in the PVA matrix with the addition of starch. These results suggest that the nano-sized Bi_2O_3–PVA composites with starch can be effectively used for radiological protection purposes. The intended applications of these composites as X-ray shielding materials can be specifically used as a new non-Pb radiation shielding material for radiation protection by interventional radiology (IR) physicians, as well as to lessen the physical repercussions of long hours wearing unnecessarily heavy radiation protection garments.

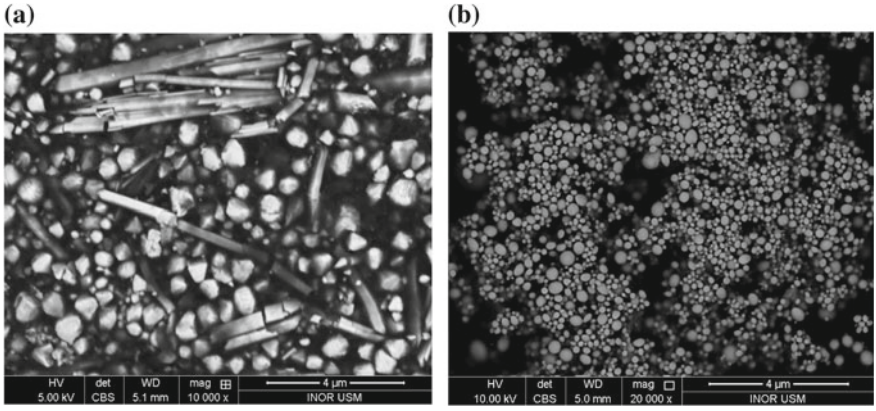

Fig. 10.5 Backscattered SEM images of 15 wt% Bi nanoparticles within PVA matrix; **a** without and **b** with 1 wt%; starch addition [31]

10.3 Conclusions

The effect of Bi_2O_3 particle sizes and the addition of starch into Bi_2O_3–PVA composites for X-ray shielding had been investigated for various X-ray energy ranges by using a variety of modalities. In the absence of starch, the X-ray transmission measurements by using XRF and mammography units displayed some variations since most of the composites had (T_m/T_n) below 1.0. Meanwhile, with the addition of starch into Bi_2O_3–PVA composite, the ratio of (T_m/T_n) from the XRF unit measurement for all filler loading (wt%) investigated had been in the range of 1.0–3.7. This indication represents the characteristic of starch, which is able to help in improving the dispersion of the Bi_2O_3 particles within a PVA matrix with minimal variance in the density readings between the micro-sized and the nano-sized Bi_2O_3–PVA composites. Hence, it has been proven that the usage of starch within the Bi_2O_3–PVA composites has helped to reduce the dependence of Bi_2O_3 particle size effect toward the density of PVA matrix, besides providing better particle size effect comparison for X-ray shielding purpose.

Acknowledgements The collection of X-ray transmission data for mammography unit was done at Advanced Medical and Dental Institute, Universiti Sains Malaysia, Bertam, 13200 Pulau Pinang, Malaysia. We also thank Mr. Mohd Anas Ahmad from Nano-Optoelectronics Research and Technology Laboratory (N.O.R), School of Physics, Universiti Sains Malaysia, Penang, 11900, Malaysia, for assistance with SEM images. This work was funded under Short-Term Research Grant, Universiti Sains Malaysia, Malaysia (304/PFIZIK/6313249).

References

1. Chang L, Zhang Y, Liu J, Fang J, Luan W, Yang X, Zhang W (2015) Preparation and characterization of tungsten/epoxy composites for γ-rays radiation shielding. Nucl Instrum Methods Phys Res B 356:88–93
2. Noor Azman NZ, Siddiqui SA, Ionescu M, Low IM (2012) A comparative study of X-ray shielding capability in ion-implanted acrylic and glass. Radiat Phys Chem 85:102–106
3. Noor Azman NZ, Siddiqui SA, Hart R, Low IM (2013) Effect of particle size, filler loadings and x-ray tube voltage on the transmitted x-ray transmission in tungsten oxide-epoxy composites. Appl Radiat Isot 71:62–67
4. Yoonkwan K, Seongeun P, Yongsok S (2015) Enhanced X-ray shielding ability of polymer–nonleaded metal composites by multilayer structuring. Ind Eng Chem Res 54:5968–5973
5. Lead X-ray glass vs. lead plastic acrylic (2013) http://www.marshield.com/nuclear-shielding/leaded-x-rayshielding-glass-and-acrylic. Viewed 15 Mar 2015
6. Noor Azman NZ, Siddiqui SA, Low IM (2013) Synthesis and characterization of epoxy composites filled with Pb, Bi or W compound for shielding of diagnostic x-rays. Appl Phys A 110:137–144
7. Jia P, Bo C, Hu L, Zhou Y (2014) Properties of poly (vinyl alcohol) plasticized by glycerin. J For Prod Ind 3:151–153
8. Jordan J, Karl IJ, Rina T, Mohammed AS, Iwona J (2005) Experimental trends in polymer nanocomposites—a review. Mater Sci Eng 393:1–11
9. Rahmat AR, Wan Abdul Rahman WA, Tin SL, Yussuf AA (2009) Approaches to improve compatibility of starch filled polymer system: A review. Mater Sci Eng C 29:2370–2377
10. Tang T, Sergio DF (2015) Computational evaluation of effective stress relaxation behavior of polymer composites. Int J Eng Sci 90:76–85
11. Botelho MZ, Künzel R, Okuno E, Levenhagen RS, Basegio T, Bergmann CP (2010) X-ray transmission through nanostructured and microstructured CuO materials. Appl Radiat Isot 69:527–530
12. Künzel R, Okuno E (2012) Effects of the particle sizes and concentrations on the X-ray absorption by CuO compounds. Appl Radiat Isot 70:781–784
13. Singh K, Sandeeo K, Kaundal RS (2014) Comparative study of gamma ray shielding and some properties of PbO-SiO2-Al2O3 and Bi2O3-SiO2-Al2O3 glass systems. Radiat Phys Chem 96:153–157
14. Ghaffari-Moghaddam M, Eslahi H (2014) Synthesis, characterization and antibacterial properties of a novel nanocomposite based on polyaniline/polyvinyl alcohol/Ag. Arab J Chem 7:846–855
15. Tang X, Alavi S (2011) Recent advances in starch, polyvinyl alcohol based polymer blends, nanocomposites and their biodegradability. Carbohydr Polym 85:7–16
16. El-Rafie MH, El-Naggar ME, Ramadan MA, Fouda MMG, Al-Deyab SS, Hebeish A (2011) Environmental synthesis of silver nanoparticles using hydroxypropyl starch and their characterization. Carbohydr Polym 86:630–635
17. Batabyal SK, Basu C, Das AR, Sanyal GS (2007) Green chemical synthesis of silver nanowires and microfibers using starch. J Biobased Mater Bioenergy 1:143–147
18. Bendaoud A, Chalamet Y (2015) Effect of a supercritical fluid on starch-based polymer processed with ionic liquid. Eur Polym J 63:237–246
19. Othman N, Azahari NA, Ismail H (2011) Thermal properties of polyvinyl alcohol (PVOH)/corn starch blend film. Malays Polym J 6:147–154
20. Maghrabi HA, Vijayan A, Deb P, Wang L (2016) Bismuth oxide-coated fabrics for X-ray shielding. Text Res J 86:649–658
21. Nambiar S, Osei E, Yeow EJ (2011) Polymer composite-based shielding of diagnostic X-Rays. Med Phys 38:3720
22. Nambiar S, Osei E, Yeow EJ (2013) Polymer nanocomposite-based shielding against diagnostic X-rays. J Appl Polym Sci 127:4939–4946

23. Singh KM, Baljit K, Gurdeep SS, Ajay K (2013) Investigations of some building materials for γ-rays shielding effectivenessRadiat. Phys Chem 87:16–25
24. Sprawls P (1993) The physical principles of medical imaging, 2nd edn. Aspen Publishers, Gaithersburg
25. Belgin EE, Aycik GA, Kalemtas A, Pelit A, Dilek DA, Kavak MT (2015) Preparation and characterization of a novel ionizing electromagnetic radiation shielding material: Hematite filled polyester based compositesRadiat. Phys Chem 115:43–48
26. Plionis AA, Garcia SR, Gonzales ER, Porterfiled DR, Peterson DS (2009) Replacement of lead bricks with non-hazardous polymer-bismuth for low-energy gamma shielding. J Radioanal Nucl Chem 282:239–242
27. Emrullahoğlu Abi CB, Yanar T (2013) Production of cordierite-mullite ceramic composite from olivine. Mach Technol Mater 12:7–11
28. Bushberg JT, Boone JM (2012) The essential physics of medical imaging. Lippincott Williams & Wilkins, Philadelphia
29. Mao L, Syed I, Sherald G, Patrizia C, Emo C (2000) Extruded Cornstarch-Glycerol-Polyvinyl Alcohol Blends: Mechanical Properties, Morphology, and Biodegradability. J Polym Environ 8:205–211
30. Akkurt I, Akyildirim H, Mavi B, Kilincarslan S, Basyigi C (2010) Gamma-ray shielding properties of concrete including barite at different energies. Prog Nucl Energy 52:620–623
31. Noor Azman NZ, Musa NFL, Nik Ab Razak NNA, Ramli RM, Mustafa IS, Abdul Rahman A, Yahaya NZ (2016) Effect of Bi_2O_3 particle sizes and addition of starch into Bi_2O_3–PVA composites for X-ray shielding. Appl Phys A 122:818
32. Virkutyte J, Varma RS (2011) Green synthesis of metal nanoparticles: Biodegradable polymers and enzymes in stabilization and surface functionalization. Chem Sci 2:837–846
33. Nikroo R, Alemzadeh I, Vossoughi M, Haddadian K (2016) Evaluation of trichloroethylene degradation by starch supported Fe/Ni nanoparticles via response surface methodology. Water Sci Technol 73:935–946
34. El-Rafie MH, Ahmed HB, Zahran MK (2014) Facile precursor for synthesis of silver nanoparticles using alkali treated maize starch. Int Sch Res Notices 2014:1–12

Chapter 11
Summary and Concluding Remarks

Abstract The use of viable processing methodologies for designing new materials with advanced nanotechnology to enhance radiation shielding purposes in order to meet the safety requirements for use in medical X-ray imaging facilities has been achieved. However, very limited or little information is still available in this emerging research field. This leaves a wide scope for future investigators to make further advances in new materials design and processing.

11.1 Summary

11.1.1 Filler Dispersion Within Epoxy Resins by Melt-Mixing Method

- Epoxy composites filled with dispersed lead oxide (PbO and Pb_3O_4) particles of 1–5 μm for composites with filler loading of ≤30 wt% and 5–15 μm for composites with filler loading of ≥50 wt% have been successfully fabricated. The phase composition analyses proved that lead oxides used in this study were single-phase pure without impurity. Meanwhile, the microstructure analyses from OM and SEM illustrated that the fractured surfaces were quite rough, and the fillers (lead oxides) were well dispersed and firmly embedded in the epoxy matrix due to their relatively small particle size and good compatibility with the epoxy matrix. The attenuation ability of the lead oxide-epoxy composites was dependable on the filler loading and composite density. They showed good X-ray attenuation properties and could be considered as a potential candidate for radiation shielding in diagnostic radiology purposes. In addition, the lead oxide-epoxy composites in this study are superior to the lead oxide-isophthalate resin composite previously investigated by other researchers since with the same wt% of lead oxide; lead oxides-epoxy composite provides better attenuation on the Gamma-rays of energy 0.662 MeV emitted from Cs-137 point source than lead oxide-isophthalate. Hence, the usage of lead oxides can be minimal in the fabrication of lead oxide-epoxy composites to provide similar attenuation ability with the lead oxide-isophthalate, and thus reduce the health risks associated with lead oxides.

© Springer Nature Singapore Pte Ltd. 2020

I. M. Low and N. Z. Noor Azman, *Polymer Composites and Nanocomposites for X-Rays Shielding*, Composites Science and Technology,
https://doi.org/10.1007/978-981-13-9810-0_11

- Epoxy composites filled with fairly dispersed $PbCl_2$, Bi_2O_3 or WO_3 have been successfully fabricated. Their attenuation ability was dependable on the filler loading and composite density. They also provide good X-ray shielding ability, and hence can be considered as candidate materials for X-ray shielding of radiological rooms. The 8 mm thick Bi_2O_3-epoxy composite with 70 wt% Bi_2O_3 is comparable to a 10 mm thick commercial lead glass which contains 56 wt% Pb while the 8 mm thick of 70 wt% $PbCl_2$- or WO_3-epoxy composites were not comparable with the lead glass unless they were prepared with a thickness greater than 10 mm. Both flexural modulus and hardness of composites increased with increasing filler loading, but the flexural strength decreased markedly when the filler loading was equal to or greater than 30 wt%.
- Epoxy composites filled with the dispersed WO_3 showed that for the same WO_3 loading, nano-sized WO_3-epoxy composite has better attenuation ability to attenuate the X-ray beams generated by lower tube voltages (25–35 kV) operated by mammography unit when compared to the micro-sized WO_3-epoxy composite. As the machine's tube voltage selected is greater than 40–49 kV, they attenuate similar amount of X-ray beams or in other word, the attenuation ability of the nano-sized and micro-sized WO_3 reinforced epoxy is indistinguishable. Meanwhile, the role of particle size in X-ray shielding was also insignificant at all tube voltage ranges (40–120 kV) for radiography unit.
- Epoxy composites filled with the dispersed WO_3 of different wt% showed that the size-effect on X-ray attenuation was profoundly dependent on the energy of synchrotron radiations. The particle size-effect was more obvious at lower synchrotron radiation energies (10–20 keV) since X-ray transmission in nano-sized WO_3-epoxy composite was less than their micro-sized counterparts. In contrast, this size-effect became insignificant at higher energies between 20 and 40 keV because the X-ray transmissions in both nano-sized and micro-sized WO_3-epoxy composites were very similar. The equivalent energy for mammography unit (25–49 kV) tube voltages are in the range of synchrotron radiation energies of 15–25 keV. Similarly, for radiography unit, the X-ray tube voltages 40–60 kV are equivalent to 25–40 keV energies. As the composite of the same WO_3 loading thickness increased, the size-effect on the X-ray attenuation tested with mammography and radiography unit was showing similar results as in (iii). Meanwhile, the effect of WO_3 loading on the mechanical properties showed an initial optimum improvement but further increase in the filler loading caused these properties to deteriorate.

11.1.2 Filler Dispersion Within Epoxy, Acrylic and Glass by Ion-Implantation Method

- Epoxy samples implanted with W, Au and Pb at various concentrations showed that the threshold of implanted ions above which the mass attenuation coefficient, μ_m of the ion-implanted epoxy composite is distinguishably higher than the μ_m of the pure epoxy is different for different ion types. The practical concentrations of W, Au and Pb in epoxy composite which could provide good X-ray attenuation properties and could be considered as candidates for effective X-ray shielding in diagnostic radiology by increasing the ion concentration than the one used in this work.
- Acrylic and glass implanted with W and Pb ions showed higher X-ray attenuation for the composite with the denser sample matrix and the composite having the higher RBS ion concentration. However, the number of implanted doses should be significantly increased so that this approach can be feasible for designing new shielding materials for the X-ray technologists. Even though glass provided the best results for both RBS ion concentration and X-ray attenuation, its usage as X-ray shielding needs extra care since it is easy to break. In contrast, implanted acrylic can be a good candidate for X-ray shielding but much time is needed when implanted acrylic with a very high nominal dose since it has a low melting point.

11.1.3 Filler Dispersion Within PLA Nanofibre Mats by Electrospinning Method

- PLA nanofibre mats dispersed with n-Bi_2O_3 and m-Bi_2O_3 showed that the electrospun n-Bi_2O_3/PLA nanofibre mats of all filler loadings (24–38 wt%) were found to be superior in attenuating X-rays compared to their micro-sized counterparts because the usage of n-Bi_2O_3 provides the fabrication of more uniform materials since the particle size can affect the microstructure and consequently the density and composition that will then modify the attenuation coefficient of the composite. However, the electrospun Bi_2O_3/PLA nanofibre mats with 38 wt% loading are not recommended for X-ray shielding because of higher porosity compared with the lower filler loadings. Meanwhile, the n-Bi_2O_3/PLA thin films are good X-ray shielding candidates only for the mammography unit at tube voltages of 22–35 kV when compared to the m-Bi_2O_3/PLA thin films. The particle size effect on X-ray attenuation diminished as the X-ray tube voltage exceeded 35 kV.

11.1.4 Effect of Starch Addition into PVA Composites

Starch offered better particle size effect for X-ray shielding ability than its micro-sized counterpart when being added into the Bi_2O_3–PVA composites. In addition, starch has improving the dispersion of nano-sized Bi_2O_3 particles within PVA matrix

and also has helped to reduce the dependence of Bi_2O_3 particle size effect toward the density of PVA matrix.

11.2 Concluding Remarks

The use of viable processing methodologies for designing new materials with advanced nanotechnology to enhance radiation shielding purposes in order to meet the safety requirements for use in medical X-ray imaging facilities has been achieved. However, very limited or little information is still available in this emerging research field. This leaves a wide scope for future investigators to make further advances in new materials design and processing. Thus, some recommendations for further research are as follows:

1. Since the relationship between the mass attenuation coefficient and particle size of lead oxide remains unknown as mentioned in Chap. 3, further study should be done to reveal their relationship since lead oxide was the familiar compound used as radiation shielding in the past.
2. The dispersion of the nano-fillers by melt-mixing method was fairly homogeneous with some particle agglomerations with the use of only high-speed mixture. However, to get perfect dispersion for nano-fillers in polymer matrices are still challenging. Therefore, different ways of mixing as well as curing is required to be investigated deeply to improve the nano-filler dispersion by melt-mixing method.
3. Deeper testing of the physical and mechanical properties of the composites should be considered so that the composites are able to practically use as an X-ray shielding for long periods of time.
4. The practical concentrations of W, Au and Pb ions implanted into an epoxy, acrylic or glass composite should be increased higher than the concentrations used in order to provide good X-ray attenuation properties and could be considered as candidates for effective X-ray shielding in diagnostic radiology.
5. Since Bi has a greater atomic number, classified as non-hazardous and is also a relatively environmentally friendly compound compared to toxic Pb, the implantation of Bi ions into the epoxy, acrylic or glass should be considered to provide good X-ray attenuation properties and could be considered as candidates for effective X-ray shielding in diagnostic radiology.
6. Deeper investigations should be considered to characterize the implanted composites. However, the higher implanted ion concentrations are required so that the characterization analyses on the composites could be succeeded.
7. The fabrication of nanofiller-nanofiber polymer by electrospinning should be tested with different filler and polymer types that are also good candidates for attenuating X-rays.

8. Further investigations on the physical and mechanical properties of the electrospun nanofiller/nanofibre PLA should be considered for X-ray shielding practical purposes.
9. More studies on the effect of starch addition into polymer matrix should be done in order to support the preliminary results of starch helping in improvement of the dispersion of nano-sized particle within polymer matrix.